



Lehrstuhl für Elektrische Energiespeichertechnik
Fakultät für Elektrotechnik und Informationstechnik
Technische Universität München

Causes and effects of inhomogeneity in lithium-ion battery modules: A physicochemical modelling approach

Dipl.-Geophys. (Univ.) Katharina Rumpf

Vollständiger Abdruck der von der Fakultät für Elektrotechnik und Informationstechnik der
Technischen Universität München zur Erlangung des akademischen Grades eines

Doktor-Ingenieur (Dr.-Ing.)

genehmigten Dissertation.

Vorsitzender: Prof. Dr.-Ing. Ralph Kennel
Prüfer der Dissertation: 1. Prof. Dr.-Ing. Andreas Jossen
2. Prof. Dr.-Ing. Kai-Peter Birke

Die Dissertation wurde am 18.09.2018 bei der Technischen Universität München eingereicht und durch
die Fakultät für Elektrotechnik und Informationstechnik am 02.12.2018 angenommen.

Kurzfassung

Elektrische Energiespeichersysteme spielen im Rahmen der Energiewende eine zunehmend größere Rolle. Nicht nur die Anzahl verkaufter Elektrofahrzeuge steigt kontinuierlich an, sondern auch die der installierten Heim- und stationären Speicher nimmt zu. Um die für die jeweilige Anwendung benötigte Kapazität und Spannung zur Verfügung stellen zu können, bestehen Batteriesysteme aus vielen verschalteten Batteriezellen. Da die produzierten Systeme verlässlich und langlebig sein sollen, sollte Inhomogenität in einem Batteriemodul vermieden werden. Inhomogenität kann dadurch entstehen, dass Zellen, die Parametervariationen aufweisen, während der Modulassembly nicht gematcht werden. Darüberhinaus kann sie durch das Moduldesign beeinflusst werden, z.B. durch das Thermomanagement oder das Zellverbinderdesign. Die vorliegende Arbeit untersucht die Gründe für und die Auswirkungen von Inhomogenität in Lithium-Ionen Batteriemodulen.

Aufgrund von Zellstreuungen als möglichem Einflussfaktor für Inhomogenität, werden die Variationen verschiedener Zellparameter und die Korrelation zwischen ihnen analysiert. Die Untersuchung basiert auf 1100 kommerziellen produktionsfrischen LiFePO_4 -Graphit Zellen, die aus zwei Chargen stammen. Die Zellparameter werden experimentell bestimmt, indem für alle 1100 Zellen DC Check-up- und AC Elektrochemische Impedanz Spektroskopiemessungen unter überwachten Temperatur- und Relaxationsbedingungen durchgeführt werden. Die Daten werden für 15 Parameter statistisch ausgewertet: verschiedene Entladekapazitäten, verschiedene DC und AC Impedanzen, die Masse und mittlere Temperatur der Zellen. Die ermittelte relative Streuung von Kapazität und Impedanz ist klein und die Variation der Impedanz lässt keinen Rückschluss auf die Variation der Kapazität zu. Von den Ergebnissen werden vier Implikationen zu empfohlenen Charakterisierungsparametern für die Entwicklung und Modellierung von Batteriemodulen abgeleitet. Die ermittelten Parameterstreuungen dienen als Input für die simulative Untersuchung der Auswirkungen von Inhomogenität in Batteriemodulen.

Zu diesem Zweck wird eine multidimensionale multiphysikalische Modellumgebung entwickelt, in der je verschalteter Zelle ein physikochemisches Modell und ein thermisches Modell mit einem elektrischen Modell gekoppelt werden. Das Modell berücksichtigt temperaturabhängige Transport- und Kinetikparameter und beschreibt das elektrochemische Verhalten jeder Zelle. Darüberhinaus wird der Wärmeaustausch mit der Umgebung betrachtet. Elektrische Konsistenz in Abhängigkeit von Modultopologie und Zellverbindern wird gewährleistet, indem elektrische Ladungs- und Energieerhaltung zwischen den Zellen berücksichtigt wird. Mittels des Modells kann der Einfluss defekter oder asymmetrischer Zellverbinder auf die Inhomogenität des Modulbetriebs untersucht werden. Betrachtet wird ein Modul von zwei parallel verschalteten Zellen unter Konstantstrom-Entladung unter verschiedenen Modulanchlusszenarien und unter dem Einfluss von Parameterstreuung in Kapazität, Impedanz und Umgebungstemperatur. Aus der Diskussion der resultierenden inhomogenen Stromaufteilung wird eine Zellmatching Strategie abgeleitet und analysiert, die die Modulperformance z.B. bei Second-Life Anwendungen verbessern kann.

Abstract

Electrical energy storage systems play an increasing role in the course of the exit from nuclear and fossil-fuel energy. Not only the number of sold electric vehicles is increasing constantly but also the number of installed home and stationary storage systems is growing. To provide the required capacities and voltage levels of the respective application, battery systems consist of multiple connected battery cells. As the produced systems should be reliable and long-lasting, inhomogeneity within a battery module should be avoided. Inhomogeneity can arise if cells which show cell-to-cell variations are not matched during battery module assembly. Or it can arise from module design reasons such as thermal management design or cell connector design. This work investigates the causes and effects of inhomogeneity in lithium-ion battery modules.

Considering cell-to-cell variations as possible causes for inhomogeneity, the parametric cell-to-cell variation of multiple different cell parameters and the correlation between them is investigated based on 1100 commercial production fresh LiFePO_4 -graphite cells which originate from two batches. The cell parameters are experimentally determined by conducting DC check-up- and AC electrochemical impedance spectroscopy-measurements under controlled temperature and relaxation conditions for all 1100 cells. The data is statistically analysed for 15 different parameters: different discharge capacities, different DC and AC impedances, the mass and mean temperature of the cells. The determined relative variation of capacity and impedance is small and it is found, that the variation of the cell impedance allows no conclusion about the variation of the cell capacity. From the results, four implications concerning recommended characterisation parameters for the development and modelling of battery modules are derived. The determined parametric variations serve as input for the simulative investigation regarding the effects of inhomogeneity in lithium-ion battery modules.

For these simulations, a multidimensional multiphysics modelling framework for lithium-ion battery modules is developed which couples a physicochemical model and a thermal model per cell with an electrical model. The electrochemical behaviour of each connected cell is described while their transport and kinetics parameters are implemented temperature dependent. Furthermore, heat exchange with the environment is considered and the conservation of electric charge and energy between the cells is accounted for in order to reach electrical consistency according to the respective module topology and cell interconnections. The model is capable of investigating the influence of defective and asymmetric cell connectors on the inhomogeneity of module operation. To evaluate this electrical influence, the observed inhomogeneities are compared to the influence of thermal gradients between the cells. The resulting inhomogeneous current distribution is presented for a module of two parallel connected cells under constant-current discharge operation for variations in cell capacity, cell impedance and ambient temperature at different module contact scenarios. From the observed impact of both, electrical and thermal variations between parallel connected cells, a cell matching strategy is derived and discussed which can enhance a module's performance during e.g. second life applications.

Vorwort und Danksagung

Die vorliegende Dissertation entstand im Rahmen meiner Tätigkeit als wissenschaftliche Mitarbeiterin am Lehrstuhl für Elektrische Energiespeichertechnik unter der Betreuung von Professor Dr. Andreas Jossen an der Technischen Universität München. Finanziert wurde sie aus einem Förderprojekt des Bayerischen Staatsministeriums für Wirtschaft und Medien, Energie und Technologie sowie aus einem Förderprojekt der Europäischen Union.

An erster Stelle gilt mein herzlicher Dank Herrn Professor Dr. Andreas Jossen, der mir die Möglichkeit zur Promotion gegeben hat und meine Arbeit stets mit großem Interesse begleitet und betreut hat. Weiterhin danke ich Herrn Professor Dr. Kai-Peter Birke für die Übernahme des Koreferats und Herrn Professor Dr. Ralph Kennel für die Leitung der mündlichen Prüfung.

Darüber hinaus danke ich meinen Kollegen am Lehrstuhl für Elektrische Energiespeichertechnik und insbesondere dem Team Simulation für die gute Zusammenarbeit und jederzeitige Unterstützung. Ich freue mich, dass das während meiner Arbeit entwickelte Simulationsmodell auch zukünftig durch meinen Kollegen Markus Schindler genutzt und weiterentwickelt wird.

Besonderer Dank gebührt meinen Kollegen Maik Naumann, Jonas Keil und Andy Noel. Danke, dass ihr immer ein offenes Ohr und eine offene Tür hattet.

Danke an meine Freundin Ina, meine Familie und an meine Oma. Es ist schön zu wissen, dass ihr da seid.

Abschließend möchte ich meinem Mann Bastian danken. Dir widme ich diese Arbeit. Danke, dass du mich immer unterstützt hast, immer an mich geglaubt hast und immer an meiner Seite warst. Ohne dich ist alles nichts. Ich freue mich auf unsere nächsten Abenteuer.

Katharina Rumpf
München, 2018

List of Publications

Within the scope of this thesis, the following publications have been generated until the 18.09.2018:

Peer-Reviewed Journal Contributions (Lead Author) *

Katharina Rumpf, Alexander Rheinfeld, Markus Schindler, Jonas Keil, Tobias Schua, Andreas Jossen. "Influence of Cell-to-Cell Variations on the Inhomogeneity of Lithium-Ion Battery Modules". In: *Journal of The Electrochemical Society* 165.11 (2018), pp. A2587-A2607.

Katharina Rumpf, Maik Naumann, Andreas Jossen. "Experimental investigation of parametric cell-to-cell variation and correlation based on 1100 commercial lithium-ion cells". In: *Journal of Energy Storage* 14 (2017), pp. 224-243.

* Self-produced sections of peer-reviewed lead author journal contributions are partially contained in this thesis without further reference in the running text.

Peer-Reviewed Journal Contributions (Co-Author)

Bernhard Rieger, Simon V. Erhard, Katharina Rumpf, Andreas Jossen. "A New Method to Model the Thickness Change of a Commercial Pouch Cell during Discharge". In: *Journal of The Electrochemical Society* 163.8 (2016), pp. A1566-A1575.

Data Bases

Katharina Rumpf, Maik Naumann, Andreas Jossen. "Statistic analysis of experimentally determined cell parameters based on 1100 production fresh commercial lithium-ion cells". Data base. <https://mediatum.ub.tum.de/node?id=1419334>, 2017.

Conference Contributions

Katharina Rumpf, Jonas Keil, Andreas Jossen. "Modelling the influence of cell-to-cell variations within lithium-ion battery modules on inhomogeneous module ageing". Poster. International Meeting on Lithium-Ion Batteries 2018, Kyoto, Japan.

Katharina Rumpf, Alexander Rheinfeld, Markus Schindler, Jonas Keil, Tobias Schua, Andreas Jossen. "Influencing factors on the inhomogeneity and performance of lithium-ion battery modules". Presentation. Electric / Electronic in Hybrid and Electric Vehicles and Electrical Energy Management 2018, Würzburg, Germany.

Katharina Rumpf, Stephan Kosch, Willy Porcher, Yvan Reynier. "Cell evaluation and modeling interest to optimize cell design". Presentation. Workshop "Next generation of competitive Li-ion batteries to meet customer expectations – made in Europe". Transport Research Arena 2018, Vienna, Austria.

Katharina Rumpf, Markus Schindler, Jonas Keil, Tobias Schua, Alexander Rheinfeld, Andreas Jossen. "Inhomogeneities in lithium-ion battery modules: A physicochemical model based analysis of influencing factors on module performance and efficiency". Presentation. Advanced Battery Power 2018, Münster, Germany.

Katharina Rumpf, Alexander Rheinfeld, Andreas Geltinger, Tobias Schua, Andreas Jossen. "Modeling inhomogeneity in lithium-ion battery modules". Poster. MSE Colloquium 2017, Garching, Germany.

Katharina Rumpf, Maik Naumann, Andreas Jossen. "Experimental investigation of cell-to-cell variations of 1100 commercial LiFePO₄-graphite cells". Poster. Batterieforum Deutschland 2017, Berlin, Germany.

Katharina Rumpf, Simon V. Erhard, Maik Naumann, Alexander Rheinfeld, Andreas Jossen. "Modeling the impact of internal cell parameters on the cell-to-cell variation of capacity and impedance". Poster. Advanced Battery Power 2017, Aachen, Germany.

Katharina Rumpf, Alexander Rheinfeld, Andreas Geltinger, Tobias Schua, Andreas Jossen. "Modeling inhomogeneity in lithium-ion battery modules". Poster. 2nd ECS Student Chapter Symposium 2016, Munich, Germany.

Katharina Rumpf, Lemuel Moraleja, Jan Geder, Andreas Jossen. "Comparing the specific heat capacity of lithium-ion cells using adiabatic calorimetry". Poster. Batterieforum Deutschland 2016, Berlin, Germany.

Peter Keil, Katharina Rumpf, Andreas Jossen. "Thermal Characterization of Li-ion Batteries: Accelerating Thermal Impedance Spectroscopy". Lecture Notes on Impedance Spectroscopy 5 – Kanoun (Ed.). Taylor & Francis Group, London, 2015.

Simon V. Erhard, Franz Spingler, Alexander Rheinfeld, Stephan Kosch, Katharina Rumpf, Andreas Jossen. "Physico-chemical Modelling of Li-ion Batteries: Parameter Analysis in the Frequency Domain". Lecture Notes on Impedance Spectroscopy 5 – Kanoun (Ed.). Taylor & Francis Group, London, 2015.

Katharina Rumpf, Simon V. Erhard, Andreas Jossen. "Multidimensional physicochemical-thermal FEM model for commercial 26650 LiFePO₄ cells". Poster. Advanced Battery Power 2014, Münster, Germany.

Peter Keil, Katharina Rumpf, Andreas Jossen. "Thermal Impedance Spectroscopy for Li-Ion Batteries with an IR Temperature Sensor System". Poster. The 27th World Battery, Hybrid and Fuel Cell Electric Vehicle Symposium and Exhibition 2013, Barcelona, Spain.

List of Contents

Kurzfassung	I
Abstract	II
Vorwort und Danksagung	III
List of Publications	IV
List of Abbreviations	IX
List of Formula Symbols	XI
1 Introduction	1
1.1 Motivation and research questions	1
1.2 Objectives	3
1.3 Outline	4
2 State of the art	7
2.1 Experimental analysis of cell-to-cell variations	7
2.1.1 Number of investigated cells	9
2.1.2 Number of investigated parameters	10
2.1.3 Correlation between parameters	10
2.1.4 Conclusion	11
2.2 Causes and effects of inhomogeneity	11
2.2.1 Inhomogeneity due to cell-to-cell variations	12
2.2.2 Inhomogeneity due to thermal gradients	14
2.2.3 Inhomogeneity due to cell connector resistances	15
2.2.4 Conclusion	16
3 Methodology	17
3.1 Definition of topologies	17
3.2 Investigated cell	17
3.3 Statistics	18
3.3.1 Parametric variation	18
3.3.2 Parametric correlation	19
3.4 Physicochemical modelling	19
3.4.1 Structure of a cylindrical lithium-ion cell	19
3.4.2 Governing equations within the p2D Newman-model	20

3.4.3	Electrochemical reactions	20
3.4.4	Analytical equations enhancing the p2D Newman-model	22
3.5	Thermal behaviour of lithium-ion cells	26
3.5.1	Thermal modelling	27
3.5.2	Calculation of thermal cell parameters	28
3.5.3	Calculation of convective heat transfer coefficients	30
4	Parametric cell-to-cell variation and correlation	35
4.1	Experimental	35
4.1.1	Measurement equipment	36
4.1.2	Relaxation and thermal conditions	36
4.1.3	CU-measurement	36
4.1.4	EIS-measurement	38
4.1.5	Possible sources of errors	38
4.1.6	Definition of parameters	38
4.1.7	Measurement uncertainties	41
4.2	Results and discussion	41
4.2.1	Parametric variations of cell parameters	42
4.2.2	Parametric correlations between cell parameters	52
4.3	Implications for developing and modelling battery modules	58
4.4	Conclusion	60
5	Influence of cell-to-cell variations on the inhomogeneity of battery modules	63
5.1	Influencing cell internal parameters on cell capacity and impedance	63
5.1.1	Influences on cell capacity	65
5.1.2	Influences on cell impedance	66
5.1.3	Variation range for parameters	67
5.2	Model development	68
5.2.1	Physicochemical model	68
5.2.2	Thermal model	68
5.2.3	Electrical model	71
5.2.4	Model coupling	78
5.2.5	Validation and parametrisation	79
5.3	Inhomogeneous current distribution due to cell-to-cell variations	84
5.3.1	Influence of the system terminal position	84
5.3.2	Impact on the Ah-throughput	88
5.3.3	Influence of the C-Rate	91
5.4	Implications for assembling battery modules	94
5.5	Conclusion	95
6	Cell matching strategy for peak current reduction	97
6.1	Assembling cells under an expected thermal gradient	98
6.2	Influence of cell connector resistances on resulting peak currents	100
6.3	Implications for assembling battery modules under a cell matching perspective	104
6.4	Conclusion	104

7 Conclusion and outlook	107
7.1 Cell-to-cell variation and correlation	107
7.2 Inhomogeneity of battery modules and matching strategy	109
7.3 Outlook	110
List of References	113
List of Figures	123
List of Tables	125

List of Abbreviations

AC	alternating current
CC	constant-current
CCCV	constant-current-constant-voltage
CFD	computational fluid dynamics
CH	charge
COD	coefficient of determination
COV	coefficient of variation
CTS	cell test system
CU	check-up
CV	constant-voltage
DC	direct current
DCH	discharge
DOD	depth of discharge
ECM	equivalent circuit model
EIS	electrochemical impedance spectroscopy
ELM	electrical model
EOD	end of discharge
EV	electric vehicle
fpd	frequencies per decade
LCO	lithium cobalt oxide
LFP	lithium iron phosphate
LTO	lithium titanate oxide
mpf	measures per frequency
MU	measurement uncertainty
NCA	lithium nickel cobalt aluminium oxide
NMC	lithium nickel manganese cobalt oxide
OC	open circuit

List of Abbreviations

OCV	open circuit voltage
PCM	physicochemical model
PE	polyethylen
PP	polypropylen
SEI	solid electrolyte interphase
SOC	state of charge
SOH	state of health
ST	system terminal
THM	thermal model
TP	turning point

List of Formula Symbols

Roman

A_{cell}	Area of a cell exposed to the surrounding air (m^2)
A_{contact}	Area of the cell contacts (m^2)
$A_{\text{electrode}}$	Area of the electrode (m^2)
Bi	Biot number (no unit)
C	Capacity of the cell (Ah)
<i>C-Rate</i>	Applied C-Rate (no unit)
C_{neg}	Capacity of the negative electrode (Ah)
C_{pos}	Capacity of the positive electrode (Ah)
C_{rated}	Rated capacity of the cell (Ah)
D_l	Diffusion coefficient in the liquid phase ($\text{m}^2 \text{s}^{-1}$)
D_s	Diffusion coefficient in the solid phase ($\text{m}^2 \text{s}^{-1}$)
E_{a,D_s}	Activation energy for diffusion (J mol^{-1})
$E_{a,k}$	Activation energy for reaction (J mol^{-1})
E_{eq}	Open circuit (equilibrium) potential (V)
$E_{\text{eq,neg}}$	Open circuit potential of the negative electrode (V)
$E_{\text{eq,pos}}$	Open circuit potential of the positive electrode (V)
L	Characteristic length of a cell (m)
M	Molar mass of the active material (g mol^{-1})
N	Vertical number of cell rows in a topology (no unit)
Nu	Nusselt number (no unit)
Nu_{bunch}	Nusselt number for a bunch of cells (no unit)
Nu_{lam}	Nusselt number for laminar flow (no unit)
Nu_{mean}	Mean Nusselt number (no unit)
Nu_{turb}	Nusselt number for turbulent flow (no unit)
P	Parallel connected cells in a battery module (no unit)
Pr	Prandtl number (no unit)
Q	Heat power averaged over the whole cell volume (W)
R_{conn}	Electric resistance of a cell connector between serial connected cells (Ω)
R_{cell}	Internal resistance of the cell (Ω)
R_{coll}	Specific electric resistance of one current collector (Ωm^{-1})
Re	Reynolds number (no unit)

R_{foil}	Effective impedance of the current collectors in a full cell (Ω)
R_{n}	Resistance of the negative cell connector between parallel connected cells (Ω)
R_{p}	Resistance of the positive cell connector between parallel connected cells (Ω)
$R_{\text{th,ws}}$	Thermal resistance of a spot-welded joint ($\text{m}^2 \text{K W}^{-1}$)
R_{ws}	Electric resistance of a spot-welded joint (Ω)
R_{wsn}	Resistance of the welding spot at the negative cell pole (Ω)
R_{wsp}	Resistance of the welding spot at the positive cell pole (Ω)
S	Serial connected cells in a battery module (no unit)
T	Temperature (K)
$T_{\text{air,in}}$	Temperature of the air entering a system (K)
$T_{\text{air,mean}}$	Mean air temperature within a system (K)
$T_{\text{air,out}}$	Temperature of the air exiting a system (K)
T_{amb}	Ambient temperature (K)
T_{cell}	Temperature of a cell (K)
T_{centre}	Temperature at the centre of a cell (K)
T_{contact}	Temperature of a cell's contact area (K)
T_{surf}	Temperature at the surface of a cell (K)
a	Side spacing ratio of a bunch of cells (no unit)
a_{v}	Active specific surface area (m^{-1})
b	Back spacing ratio of a bunch of cells (no unit)
$c_{\text{g,th}}$	Theoretical gravimetric capacity (Ah kg^{-1})
c_{l}	Concentration of lithium in the electrolyte (mol m^{-3})
$c_{\text{l,0}}$	Initial concentration of lithium in the electrolyte (mol m^{-3})
c_{p}	Specific heat capacity ($\text{J kg}^{-1} \text{K}^{-1}$)
$c_{\text{p,air}}$	Specific heat capacity of air ($\text{J kg}^{-1} \text{K}^{-1}$)
$c_{\text{p,cell}}$	Specific heat capacity of a cell ($\text{J kg}^{-1} \text{K}^{-1}$)
$c_{\text{p,conn}}$	Specific heat capacity of the cell connectors ($\text{J kg}^{-1} \text{K}^{-1}$)
$c_{\text{s,0}}$	Initial concentration of lithium in the active material (mol m^{-3})
c_{s}	Concentration of lithium in the active material (mol m^{-3})
$c_{\text{s,max}}$	Theoretical maximum concentration of lithium in the active material (mol m^{-3})
$c_{\text{v,th}}$	Theoretical volumetric capacity (Ah m^{-3})
d_{cell}	Diameter of a cylindrical cell (m)
dx_{cell}	Distance between two adjacent connected cells (m)
f_{A}	Arrangement factor of a bunch of cells (no unit)
h_{cell}	Height of the cell (m)
h_{conv}	Convective heat transfer coefficient ($\text{W m}^{-2} \text{K}^{-1}$)
i_{app}	Current applied at the system terminal (A)
i_{cell}	Current flowing through a cell (A)
i_j	String current within string j with $j \in [1, y]$ (A)
i_{n}	Current at the negative end of a string of x serial connected cells (A)
$i_{\text{n,cell}}$	Current at the negative cell pole (A)

i_p	Current at the positive end of a string of x serial connected cells (A)
$i_{p,cell}$	Current at the positive cell pole (A)
i_v	Local current source ($A\ m^{-3}$)
j_0	Exchange current density ($A\ m^{-2}$)
j_{1C}	Current density at a $C-Rate=1$ ($A\ m^{-2}$)
j_{Li}	Pore wall flux at the electrode-electrolyte interface ($mol\ m^{-2}\ s$)
j_{loc}	Local current density ($A\ m^{-2}$)
j_{ns}	Normal electrode current density ($A\ m^{-2}$)
j_{rate}	Current density at a given $C-Rate$ ($A\ m^{-2}$)
k	Reaction rate (ms^{-1})
k_{air}	Thermal conductivity of air ($W\ m^{-1}\ K^{-1}$)
k_{conn}	Thermal conductivity of the cell connectors ($W\ m^{-1}\ K^{-1}$)
k_r	Radial thermal conductivity of a cell ($W\ m^{-1}\ K^{-1}$)
k_{ref}	Reaction rate reference value (ms^{-1})
k_z	Axial thermal conductivity of a cell ($W\ m^{-1}\ K^{-1}$)
l_{conn}	Length of the cell connectors (m)
m_{cell}	Mass of a cell (kg)
o	Number of parallel connected strings in between of string j and the ST (no unit)
q	Heat power (W)
q_{cond}	Conducted heat power (W)
q_{conv}	Convected heat power (W)
q_{diss}	Dissipated heat power (W)
q_{gen}	Generated heat power (W)
q_{rad}	Radiated heat power (W)
r_{cell}	Radius of a cylindrical cell (m)
r_p	Particle radius (m)
s_1	Distance between two horizontal cell rows in a topology (m)
s_2	Distance between two vertical cell rows in a topology (m)
t_{conn}	Thickness of the cell connectors (m)
$t_{electrode}$	Thickness of the electrode (m)
t_{coll}	Thickness of the current collector (m)
t_{neg}	Thickness of the negative electrode (m)
t_+	Transport number of Li^+ (no unit)
t_{pos}	Thickness of the positive electrode (m)
t_{sep}	Thickness of the separator (m)
v_{air}	Velocity of air (ms^{-1})
w_{conn}	Width of the cell connectors (m)
x	Number of serial connected cells in a topology (no unit)
x_0	Electrode stoichiometry at delithiated state of a full cell (no unit)
x_{100}	Electrode stoichiometry at lithiated state of a full cell (no unit)
$x_{electrode}$	Length of an electrode stack (m)

x_{\max}	Maximum x-coordinate of a PCM stack (m)
x_{stack}	x-coordinate of a PCM stack (m)
x_{coll}	Length of the current collector (m)
x_{contact}	Thickness of the cell contacts (m)
y	Number of parallel connected cells (or strings) in a topology (no unit)
$y_{\text{electrode}}$	Width of an electrode stack (m)
y_{coll}	Width of the current collector (m)
z	Number of e^- exchanged during (de-)lithiation (no unit)

Greek

α_a	Anodic charge-transfer coefficient (no unit)
α_c	Cathodic charge-transfer coefficient (no unit)
ε_l	Electrolyte volume fraction (no unit)
ε_{rad}	Surface emissivity (no unit)
ε_s	Active material volume fraction (no unit)
η_{CT}	Overpotential due to charge transfer (V)
η_i	Internal polarisation of a cell i (V)
κ_l	Ionic conductivity in the electrolyte (S m^{-1})
μ	Mean of a normal distribution (no unit)
ν_{air}	Viscosity of air ($\text{m}^2 \text{s}^{-1}$)
ϕ	Electric potential of a cell (V)
ϕ_l	Potential of the liquid phase within a PCM (V)
ϕ_s	Potential of the solid phase within a PCM (V)
ϕ_{system}	Electric potential of the system (V)
ψ	Voidage percentage of a bunch of cells (no unit)
ρ_{air}	Density of air (kg m^{-3})
ρ_{AM}	Density of the active material (kg m^{-3})
ρ_{coll}	Resistivity of the current collector material (Ωm)
ρ_{conn}	Density of the cell connectors (kg m^{-3})
σ	Standard deviation of a normal distribution (no unit)
σ_{conn}	Electric conductivity of the cell connectors (S m^{-1})
σ_s	Electric conductivity of the active material (S m^{-1})
τ	Tortuosity (no unit)

Subscripts

AM	Active material
air	Air
amb	Ambient environment
cell	Cell
coll	Current collector
conn	Cell connector
contact	Cell contacts
electrode	Electrode

hold	Module holder
l	Liquid phase
lam	Laminar flow
mean	Mean value
n	Negative cell pole or negative end of a string
neg	Negative electrode
p	Positive cell pole or positive end of a string
pos	Positive electrode
s	Solid phase
sep	Separator
stack	Stack of anode, separator and cathode
string	String of multiple serial connected cells
system	System of multiple connected cells
turb	Turbulent flow
ws	Welding spot
aligned	Aligned arrangement of cells within a topology
bunch	Bunch of cells within a topology
row	Horizontal row of cells within a topology
staggered	Staggered arrangement of cells within a topology
Natural constants	
F_{const}	Faraday constant (96,485 As mol ⁻¹)
R_{const}	Universal gas constant (8.314 kg m ² s ⁻² mol ⁻¹ K ⁻¹)
σ_{B}	Stefan-Boltzmann constant (5.67×10^{-8} W m ⁻² K ⁻⁴)

1

Introduction

1.1 Motivation and research questions

Electrical energy storage systems play an increasing role in the course of the exit from nuclear and fossil-fuel energy. Not only the number of sold electric vehicles (EVs) is increasing constantly but also the number of installed home and stationary storage systems is growing. In order to provide the required capacities and voltage levels of the respective application, battery systems consist of multiple connected battery cells. Connecting cells in series increases the voltage level, whereas connecting cells in parallel increases the capacity of the system. Within a series connection of battery cells, the capacity of the weakest cell specifies the capacity of the battery system [1; 2] and moreover its lifetime [3]. When connecting cells in parallel, a variation in the cell impedances results in different currents through the cells [4–6], resulting in different states of charge (SOCs), temperatures and degradation rates during operation although their terminal voltage is at the same level [7].

In order to be able to produce reliable and long-lasting battery systems, inhomogeneity within a module should be avoided [8]. Inhomogeneity in a battery module in this context denotes a gradient of a certain parameter across connected battery cells. There are different reasons which can lead to inhomogeneity within battery modules (compare Figure 1.1). On the one hand, it can result from cell internal reasons, i.e. by integrating unmatched cells into battery modules, which show cell-to-cell variations in capacity and impedance [7–12]. On the other hand, it can also result from cell external reasons, which relate to the module design, such as thermal management design or cell connector design. Inhomogeneity can evolve as asymmetrical cell connectors result in uneven cell connector resistances [13], due to uneven [13] or defective cell contacts [4; 14], from a disadvantageous cell arrangement, an ineffective cooling strategy [15] or an external heat source next to the battery module [16; 17].

Battery cells can, in spite of high quality standards for commercial lithium-ion cells, result from manufacturing tolerances [7; 9; 18–21] and varying shipping or storage conditions. When integrating unmatched cells into battery modules, these variations will lead to an inhomogeneous current distri-

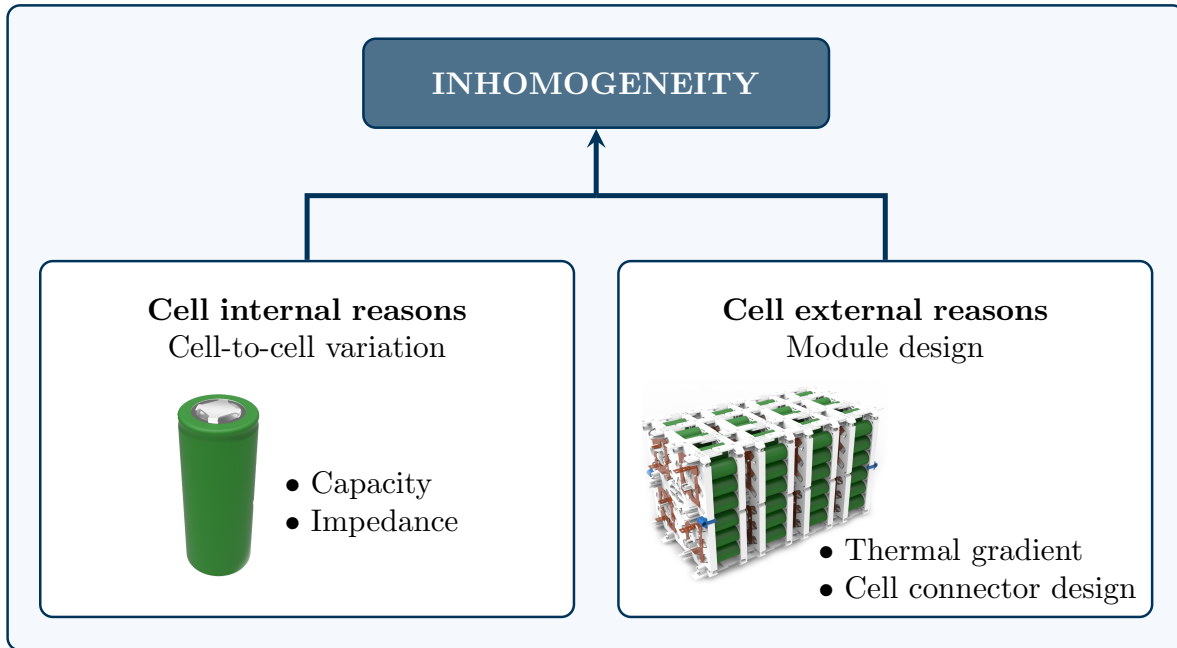


Figure 1.1: Influencing factors on inhomogeneity in lithium-ion battery modules.

bution across the module depending on the module topology [1; 6; 7; 10; 11; 22]. As a consequence, the individual cells are subjected to different currents and temperatures during module operation [23], which may result in inhomogeneous [7] and accelerated ageing [9; 10]. Therefore, parametric cell-to-cell variations are crucial to consider when designing and assembling battery modules.

An ineffective cooling strategy [15] or an external heat source next to the battery module leads to a thermal gradient across the battery module [15; 16]. On the short time scale, this gradient results in a current deviation between parallel connected cells or strings [17] and thus affects the module performance [17; 24]. On the long scale, temperature variations might moreover lead to differently aged cells [7; 25].

When regarding single cell ageing, high storage temperatures lead to a stronger electrolyte decomposition and solid electrolyte interphase (SEI) growth which results in accelerated cell degradation [26–28] due to cell capacity decrease and cell resistance increase [29]. High cell temperatures during cell cycling with a highway driving cycle (e.g. US06) have however been found to decrease the capacity fade, as stress and degradation caused by (de-)intercalation processes are reduced at higher temperatures [28; 30].

Especially for high applied *C-Rates*, unintended peak currents, which exceed the intended applied *C-Rate*, might approach the cell current specification limit for the assembled cells. They can become a severe safety risk, especially when occurring over a longer period of time or more often during cycle life. During charging routines of EVs, high current peaks are even more severe – especially at cold ambient temperatures [31]. High charging currents can then result in lithium plating, which can lead to dendrite growth and possibly to an internal short circuit in the worst case [31]. Peak currents will moreover lead to a higher generated heat within the respective cell, which will increase the cell temperature and can thus lead to a thermal hotspot within the battery module. Therefore, aiming for a cell matching approach in order to reduce occurring peak currents can help to not exceed the current

specification limit, reduce the generated heat and emergence of thermal hotspots and thus increase the module safety and module lifetime.

An alternative to cell matching during module assembly is to implement a balancing system within the battery management system [32]. Although balancing systems mostly estimate the SOC of the cells [33; 34], also other balancing approaches have been reported, such as balancing the cell temperature [23; 35–37] or compensating cell terminal voltage variations due to cell-to-cell impedance differences [23; 36; 37].

Effective matching during battery module assembly requires the knowledge of the varying parameters for each single cell. Related measurements are time consuming and are rarely to be realised in practice. Therefore, quantifying and comparing the impact of manufacturing related parametric cell-to-cell variations on the evolving inhomogeneity within a battery module by simulation is a potential option.

When aiming to determine the parametric variation of lithium-ion cells due to manufacturing tolerances for scientific reasons, it must be ensured that possible cell-to-cell variations do not result from external reasons. Such reasons could be that the cells originate from different production batches, that the cells have been shipped under different conditions, thus experiencing a different calendaric ageing, or that the cells have already experienced an operational history, i.e. have been cycled prior to the cell characterisation measurements, maybe even under different measurement conditions. Concluding, in order to being able to rely on experimentally determined parametric variations due to manufacturing tolerances, the cells to be used for investigation should be production fresh.

In this context, the following research questions emerge:

1. How strong is the cell-to-cell variation of different cell parameters and how do these parameters correlate with each other?
2. Which parameters should be measured, in order to adequately depict cell-to-cell variations?
3. What happens if cells under cell-to-cell variations are connected and how does a temperature gradient across a battery module influence the module characteristics?
4. Is there a possibility to reduce this influence by adequate cell matching?

1.2 Objectives

On the basis of the above mentioned research questions, this thesis has the main aim to investigate the causes and effects of inhomogeneity in lithium-ion battery modules. Therefore, the following objectives and tasks have been set for this thesis:

1. Quantify the cell-to-cell parametric variations of production fresh commercial lithium-ion cells due to manufacturing tolerances.
2. Analyse possible correlations between cell parameters which can be measured during cell characterisation.
3. Develop a physicochemically based modelling framework, which is able to account for cell-to-cell variations in capacity and impedance, different cell connector designs and external thermal gradients.

4. Compare the influences of cell internal and cell external reasons on the inhomogeneity of lithium-ion battery modules.
5. Apply the model to derive a cell matching strategy for peak current reduction during battery module operation.

In order to further define the scope of this thesis, some limitations are to be highlighted. Within this thesis, the focus is on examining the variation of cell parameters at one point in time, namely when the cells are production fresh. Ageing of cells or modules is not investigated – neither experimentally nor by simulation. The developed model is not coupled to any ageing model and therefore no conclusions are met about the battery module behaviour over lifetime.

1.3 Outline

The thesis is structured as depicted in Figure 1.2.

Following the introduction, the state of the art regarding the experimental analysis of cell-to-cell variations and regarding the causes and effects of inhomogeneity is presented in Chapter 2.

Chapter 3 sets the methodical context regarding the definition of topologies, the investigated cell, the statistic theory for parametric variation and correlation, physicochemical modelling and the thermal behaviour of lithium-ion cells.

Following this, the cell-to-cell variation and correlation of different cell parameters is experimentally investigated in Chapter 4: The experimental settings are described including the measurement equipment with its corresponding measurement precision, the relaxation and thermal conditions, the settings of the direct current (DC) and alternating current (AC) measurements, possible sources of error, the definition of the investigated parameters and their measurement uncertainties. The results are illustrated, described and discussed in three parts: First, the parametric variations of the cell parameters is presented. Second, the parametric correlations between the cell parameters are analysed. Third, implications for developing and modelling lithium-ion battery modules are derived from the results.

In Chapter 5, the multidimensional multiphysics model is presented and the influence of cell-to-cell variations on the inhomogeneity of battery modules is investigated by simulation: First, the influencing cell internal parameters on cell capacity and impedance are discussed theoretically and based on literature. Furthermore, typical ranges for occurring cell-to-cell variation ranges are given for capacity, impedance and ambient temperature. This is followed by the description of the multidimensional multiphysics model for general *xSyP* battery modules. The simulation results depict the inhomogeneous current distribution within a 2P battery module due to attributed cell-to-cell variations, different module contact designs and different *C-Rates* while discussing the findings from a physicochemical point of view. The results lead to first implications regarding the assembly of lithium-ion battery modules.

To demonstrate an application scenario of the developed model, a matching approach for reducing peak currents during battery module operation is presented in Chapter 6. Here, the cell assembly under expected thermal gradients and the influence of different cell connector resistances on peak currents is discussed. The results lead to further implications regarding the assembly of lithium-ion battery modules.

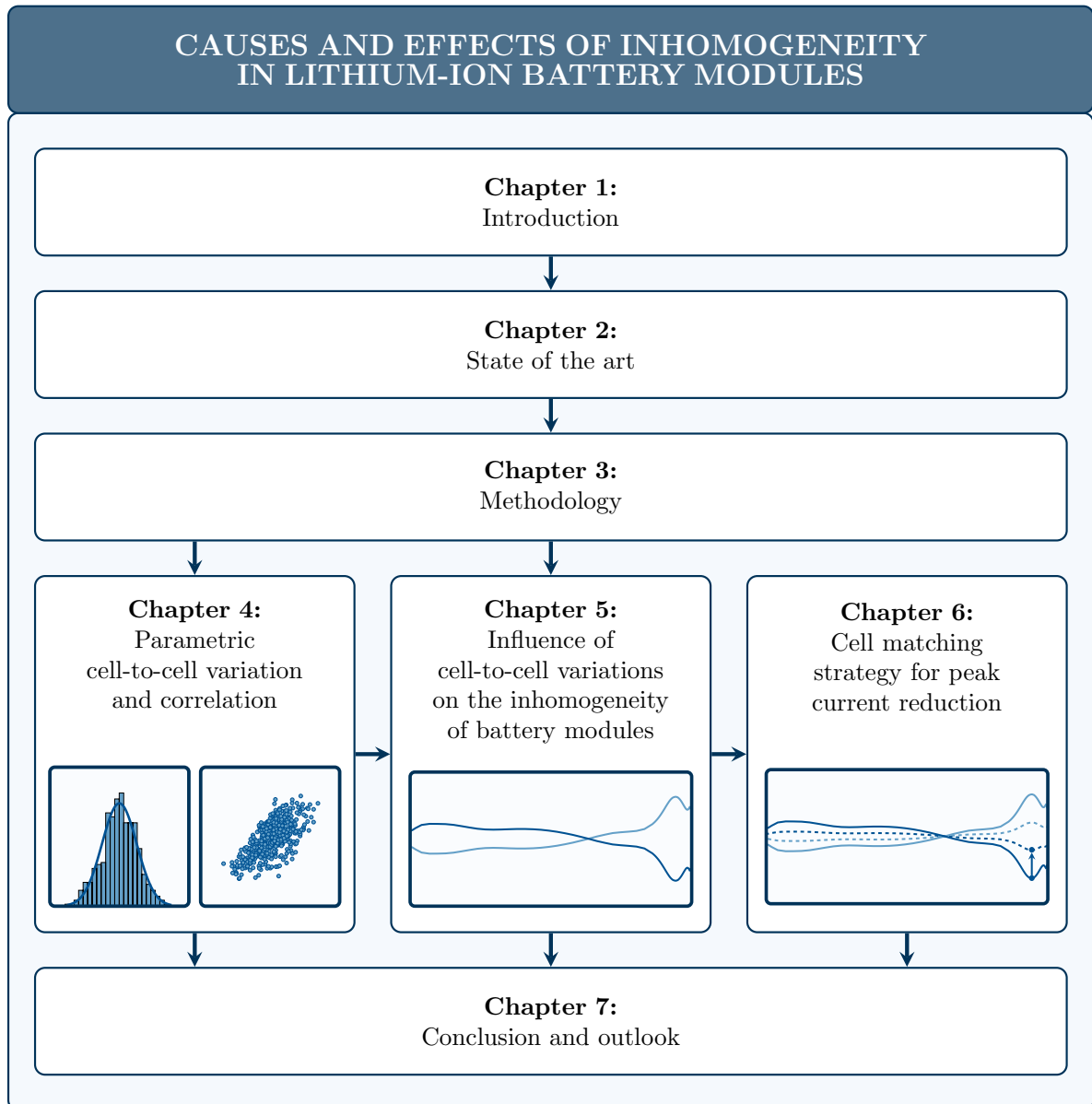


Figure 1.2: Structure of the thesis.

The conclusion of the thesis is outlined in Chapter 7 by first focusing on concluding the findings from the experimental investigation of cell-to-cell variations and correlations. Afterwards, the findings from the simulative investigation of inhomogeneity in battery modules and from the cell matching approach are summarized. An outlook regarding possible application scenarios of the presented results and towards further research objectives closes the thesis.

2

State of the art

This chapter gives an overview about the state of the art regarding the objectives of this thesis. First, a literature review focussing on the experimental analysis of cell-to-cell variations is given, which is mainly based on the publication “Experimental investigation of parametric cell-to-cell variation and correlation based on 1100 commercial lithium-ion cells” by Rumpf et al. [38]. Afterwards, a literature review is given which deals with modelling approaches towards causes and effects of inhomogeneity. This second review is mainly based on the publication “Influence of cell-to-cell variations on the inhomogeneity of lithium-ion battery modules” by Rumpf et al. [39]. Each of the literature reviews are concluded and the knowledge gap within current literature is highlighted.

2.1 Experimental analysis of cell-to-cell variations

The experimental determination of commercial cell-to-cell parametric variations has been addressed by a handful of research groups. However, measurements to determine cell-to-cell variations are time consuming: in order to allow for a thorough statistic analysis a large amount of cells has to be investigated. In terms of cell characterisation, this requires excessive measurement capacities.

Most publications, which base their work on a statistic analysis of battery cells, aim to investigate ageing behaviour [9; 10; 19–21; 40] or the assembly and performance of battery modules [1; 9–11; 19; 20; 41; 42]. In these cases the statistic analysis is mostly addressed marginally alongside the main focus of the respective work.

Table 2.1 gives an overview of the conducted literature review regarding the statistic analysis of battery cells.

Table 2.1: Overview over the literature review regarding the statistic analysis of battery cells including information about the number of investigated cells, the investigated parameters and the correlation between parameters. Abbreviations: alternating current (AC), direct current (DC), constant-current (CC), constant-current-constant-voltage (CCCV), discharge (DCH).

Author	Ref.	Number of cells	Parameters	Correlation
An	[43]	5473	mass capacity	capacity / <i>C-Rate</i> DC impedance / <i>C-Rate</i>
Baumhöfer	[11]	198	DC impedance	Im(<i>Z</i>) AC impedance / lifetime Re(<i>Z</i>) AC impedance / lifetime AC frequency / lifetime initial DC impedance / lifetime
	[21]	7739 48	capacity CCCV-DCH capacity temperature	
Campestrini	[20]	250	capacity impedance	–
Dubarry	[8]	100	mass initial SOC discharge (DCH) capacity DC impedance	specific capacity / capacity
	[18]	10	mass initial SOC DCH capacity DC impedance	–
Gogoana Kenney	[10]	72	DC impedance	–
	[44]	simulation	electrode thickness electrode density active material weight fraction	–
Miyatake Paul	[1]	12	DCH capacity	–
	[9]	20000	initial capacity DC impedance	–
Santhanagopalan	[45]	simulation		electrode thickness / AC impedance porosity / AC impedance tortuosity / AC impedance particle size / AC impedance
Schuster	[19]	484 new 1908 aged	CCCV capacity AC impedances	–
	[46]	83 partly aged		CCCV capacity / AC impedances
Zheng	[41]	96	AC impedance DC impedance	–
	[42]	16	capacity	–

2.1.1 Number of investigated cells

Many publications base their statistic analysis on no more than 250 cells [1; 8; 10; 18; 20; 21; 40–42].

Dubarry et al. [8] have investigated 100 cells and measured their respective distribution of weight, initial SOC (as delivered), and discharge capacity. By simulation they identified cell internal attributes which resulted in the experimentally determined cell-to-cell variations. The amount of active material, polarisation resistance, and localised kinetic factors. Following this, they further investigated 10 cells towards their cell-to-cell variations [18] and chose a "nominal sample cell" in order to examine ageing phenomena in the cells [40].

Zheng et al. [41] have examined 96 cells regarding the variation of impedances in order to distinguish between the internal and contact resistance increase faults when the cells are connected in series. After having measured the variation of capacity of 16 cells, they connected 8 of them in series to a small battery module and parametrized a model which describes both, the battery module's state and the single cells' inconsistencies [42].

Miyatake et al. [1] have experimentally examined the influence of cell-to-cell variations in capacity on the discharge capacity of differently connected battery module topologies assembled from up to 12 cells. When cells are connected in series, the module capacity is affected by the cell with the smallest capacity. When cells are connected in parallel, the capacities of the single cells add up to the module capacity. When cells are connected in series and parallel, the module capacity depends on the module configuration.

Gogoana et al. [10] have measured the impedance variation of 72 cells in order to show that when two cells, which have a 20% different impedance, are connected in parallel, they experience an up to 40% higher ageing than two parallel-connected cells which have a similar internal resistance.

Campestrini et al. [20] compared battery module ageing to that of single cell ageing. For this they examined two battery modules consisting of 112 cells each which had been matched from a lot of 250 cells. Disassembling the battery modules allowed for an ageing analysis of capacity fade and impedance rise regarding local temperature distribution and cell-to-cell variation within the modules.

Baumhöfer et al. [21] have analysed the variation of capacity (constant-current-constant-voltage (CCCV)) of 48 commercial cells at two states of ageing. Moreover, they determined different pulse and AC impedances in order to identify parameters to be measured at the begin-of-life in order to predict ageing behaviour. They found that the deviations between the capacities of the aged cells increase compared to the capacity distribution of the new cells. They point out that using more cells for the statistic investigation, would be beneficial [21].

Some research groups do examine larger lots of cells [9; 11; 19; 43; 46].

Paul et al. [9] have investigated 20000 lithium-ion cells. They measured the initial cell capacity and the direct current resistance. Using 96 of these cells they furthermore examined ageing inhomogeneity in battery systems due to both, cell-to-cell variations and temperature gradients and validated a battery module simulation approach based on the Monte Carlo method.

An et al. [43] have measured the rate dependency of cell-to-cell variations of lithium-ion cells. Therefore they analysed the distribution of cell capacity and mass based on 5473 cells. From these they used 198 cells to additionally examine the DC impedance and correlate both, the capacity and the DC impedance, to the current rate. From the capacity distribution of 7739 cells they moreover matched

cells to build parallel-connected battery modules. Using these, they validated their equivalent circuit model (ECM) and studied the effect of cell sorting methods on the battery module's performance. [11] Schuster et al. [19] have analysed 484 new and 1908 aged lithium-ion cells from two identical battery electric vehicles towards their capacity and impedance distribution. The distribution shapes change during ageing from normal towards Weibull distribution. Following this, having complemented the data set by additional 83 partly aged cells, they furthermore examined the correlation between capacity and impedance of lithium-ion cells during calendar and cycle life in order to conclude upon whether testing the cell impedance can be used to deduce the cell capacity [46]. The correlation behaviour is strongly dependent on operational and storage conditions.

2.1.2 Number of investigated parameters

What becomes clear: Most papers do only examine the variation of one DC or AC impedance and one discharge capacity - sometimes even without clearly specifying whether the discharge capacity has been determined during the constant-current (CC) phase or the CCCV phase. Only a small number of publications determine the cell-to-cell variations of different impedances [19; 21]; none of them reports on a comparison of different capacities. However, such a comparison for both, capacities and impedances, seems crucial in order to make sure that the determined parameter during cell characterisation is the most promising to be used in order to reveal the desired information. What is more, discussing the dependency between different external cell parameters, i.e. a certain cell capacity and impedance, can help to reveal dependent parameters of which one could in consequence be omitted during cell characterisation and which would thus save measurement time.

2.1.3 Correlation between parameters

The dependency between different external cell parameters can be depicted by investigating the correlation between these parameters. Schuster et al. [46] have shown the correlation between two different AC impedances and the discharge capacity respectively. They compared the correlation plots determined from new cells to those of differently aged additional cells. They have neither correlated the two AC impedances to each other nor have they regarded DC impedances, different discharge capacities or other external cell parameters. Schweiger et al. [47] have determined the internal resistance of a cell by using different DC and AC methods and discussed the results qualitatively. However, as only one single cell was tested, they have not been able to show correlation graphs of the different impedances which would have been beneficial in order to quantify the dependency between the investigated parameters. Baumhöfer et al. [21] have examined the respective real and imaginary part as well as the frequency of an AC impedance and an additionally determined pulse resistance at the begin of life. Subsequently they correlated these parameters to the calculated lifetime of their investigated number of cells. However, they have not correlated the parameters themselves. An extensive study of the correlation between multiple different external cell parameters of new cells has not yet been reported.

By simulation, correlations between cell parameters have already been addressed. By developing an impedance model, Santhanagopalan et al. [45] have investigated the dependency of the variability of certain internal cell parameters (such as electrode thickness, porosity, tortuosity and particle size) on the parametric variation of the AC impedance and thus on the performance at cell level. Kenney et al. [44] have simulated capacity variations in electrode manufacturing by varying the electrode thickness,

electrode density and active material weight fraction and discussed their impact on the resulting capacity of serial-connected lithium-ion cells. However, they have not correlated the parameters.

Manufacturing tolerances of lithium-ion batteries lead to a certain variance of internal cell parameters which can cause different external behaviour from cell to cell. However, cell characterisation regarding these internal cell parameters on a big scale is difficult, as this requires the disassembly of manufactured cells and time intensive experimental investigation. Instead, determining the cell external parameters for the purpose of cell sorting and matching during battery module assembly is beneficial.

2.1.4 Conclusion

During the literature study on the experimental analysis of cell-to-cell variations it became clear that a comparison of the presented results is difficult, if these are based on different cells, parameters and measurement conditions. In order to investigate parametric cell-to-cell variation and correlation between external cell parameters, using and comparing cell-to-cell variation data from different literature sources is not sensible. Rather should the measurements, parameter determinations and data analysis be from one literature source.

Therefore, Chapter 4 presents results regarding cell-to-cell variations of multiple external cell parameters such as cell capacities, impedances, mass and temperature and examines the dependency between these parameters by discussing their correlation. The requirements of a thorough statistic analysis are met by basing the investigation on a sufficient number of cells. Furthermore, the measurement conditions including the temperature as well as the relaxation times between the different characterisation measurements are strictly monitored for each single cell. From the analysis implications for the development and modelling of battery modules and for the quality control during cell production are extracted.

2.2 Causes and effects of inhomogeneity

Literature studies, which have focussed on modelling the effects of influencing factors on the inhomogeneity of battery modules, have mostly implemented either cell-to-cell variations (in cell capacity (dC) [1; 6; 7; 11; 22; 48], impedance (dR) [1; 6; 7; 10; 11; 22; 36; 37; 48–50] or SOC ($dSOC$) [35–37; 51–53]) or thermal gradients [17; 35–37; 49; 51; 54–57] or varying interconnection resistances [4; 13; 14; 50]. Although a comparison of the cell internal influence of both, a dC and dR variation is not uncommonly reported together [1; 6; 7; 11; 22; 48], cell internal and cell external influences on inhomogeneity have seldom been compared [49–51]. Investigations which model the inhomogeneity in battery modules have mostly used ECMs for the single connected cells [1; 4; 6; 7; 10; 11; 13; 35–37; 48; 50; 53–55; 57]. Only a handful of groups have used physicochemical models (PCMs) for the cells [14; 17; 52; 56] which require vast parameterisation effort and complex numerical computation schemes to solve for the differential algebraic equation system compared to the ECM. However, using PCMs allows for an implementation of temperature dependent transport and kinetics parameters and moreover for a discussion from an electrochemical point of view due to a deeper insight into the electrochemical reactions during module operation. Wu et al. [14] focus on the influence of cell connectors and their interconnection resistances on the performance of battery modules. Yang et al. [17] and Huang et al. [56] investigate the impact

of thermal gradients on the current distribution between parallel connected cells. Capron et al. [52] examine the impact of SOC-variation ($dSOC$) between cells which are cooled by forced convection.

Table 2.2 gives an overview of the conducted literature review regarding causes and effects of inhomogeneity.

In the following, literature investigating different influences on the inhomogeneity of battery modules is analysed in detail.

2.2.1 Inhomogeneity due to cell-to-cell variations

Inhomogeneity in lithium-ion battery modules due to a variation in cell capacity (dC) and impedance (dR) has been simulated by a couple of groups [1; 6; 7; 11], while others have focused on a variation in SOC between connected cells [52; 53].

Miyatake et al. [1] have examined the characteristics of serial, parallel and combined connected cells under dC and dR variation during discharge by using ECMs for the cells. They found that the cell with the smallest capacity dominates the capacity of the serial string. Within a parallel connection, the cell capacities add up. These relationships have also been used by Kim et al. [48], when they used ECM-based models of serial, parallel and combined connected cells to estimate the SOC of a battery module while taking dC and dR variations into account.

Both, Brand et al. [6] and Bruen et al. [7], presented a validated ECM-electrical model (ELM) study of parallel connected cells under dC and dR cell-to-cell variations. Whereas Brand et al. connected production fresh cells under certain variations, Bruen et al. induced the cell-to-cell variations by connecting cells at different stages of ageing, which has also been done by An et al. [11]. Brand et al. found that under a dR variation, the cell currents divide between the two parallel connected cells based on the ratio of their internal resistances and gradually equalise during the progressing CC phase. Under a dC variation, the ratio of the cell capacities result in a long lasting current difference between the cells [6]. The highly dynamic driving cycle used by Bruen et al. did not result in a strong SOC variation between the four connected cells. However, when the driving cycle comprises small currents and large depth of discharges (DODs), then the probability of obtaining a higher degree of inhomogeneity within the module increases. According to Bruen et al. [7], the magnitude of the applied current furthermore determines whether the cell currents diverge or converge after a step-wise change in current. For a small applied current, the system response is dominated by the self-balancing processes between the parallel connected cells [7]. Due to the nature of the ECM approach, no electrochemical phenomena have been discussed.

The experimental study conducted by Bruen et al. [7] was extended further by Pastor-Fernandez et al. [22], who found that the current imbalance between parallel connected cells does not only depend on the initial state of cell ageing (and thus on their initial capacity and impedance), but also on the dependence of open circuit voltage (OCV) and cell impedance on the SOC. Moreover, they conclude that when regarding ageing of parallel connected cells, the charge-throughput and thermal energy of the connected cells converge over time.

By analysing a 2P module under CC-cycling, Gogoana et al. [10] found that an internal resistance matching of parallel cells is crucial to reduce the capacity fade of a battery module. In order to reduce accelerated ageing of a module, they recommend to not charge the cells to full capacity as this is

Table 2.2: Overview over the literature review regarding causes and effects of inhomogeneity including information about the simulated module topology, the class of the cell model, the implemented physics coupling between the different submodels, the investigated cell-to-cell variations, the operation scenarios and whether cell interconnections R_{conn} are considered. Abbreviations: equivalent circuit model (ECM), electrical model (ELM), physicochemical model (PCM), thermal model (THM), constant-current (CC), constant-current (CCC), constant-current-constant-voltage (CCCV), open circuit (OC), discharge (DCH), charge (CH).

Author	Ref.	Module	Cell model	Coupling	VAR	Operation	R_{conn}
An	[11]	1S2P	ECM	ECM-ELM	dC, dR	CC-DCH	No
Brand	[6]	1S2P	ECM	ECM-ELM	dC, dR	CC-DCH, OC	Yes
Bruen	[7]	1S4P	ECM	ECM-ELM	dC, dR	CC-DCH	Yes
Capron	[52]	10 cells	PCM	ECM-ELM	$dSOC$	driving cycle	No
Dubarry	[53]	1S2P 1S3P	ECM	ECM-ELM	$dSOC$	CC-DCH, OC	No
Fleckenstein	[51]	2S2P	ECM	ECM-THM	$dT, dSOC$	CC-DCH-CC-CH, OC	Yes
Gogoana	[10]	1S2P	ECM	ECM-ELM	dR	CC-cycling	No
Grün	[50]	1S4P	ECM	ECM-ELM	dR, dR_{conn}	CC-DCH-CCCV-CH-cycling	Yes
Huang	[56]	4S6P	PCM	ECM-THM	dT	CC-DCH	No
Kamalisiahroudi	[49]	1S2P	only exp	PCM-THM	dT, dR	CC-cycling	No
Kim	[48]	2S1P 3S1P 4S1P	ECM	only exp	dC, dR	CC-DCH	No
Klein	[57]	1S5P	only exp	only exp	dT	CC-DCH CC-cycling pulse-DCH	No No No
Miyatake	[1]	2S 2P	ECM	ECM-ELM	dC, dR	CC-DCH	No
Offer	[4]	2S2P 7S12P	ECM	ECM-ELM	dR_{conn}	CC-cycling	Yes
Pastor-Fernandez	[22]	1S4P	only exp	only exp	dC, dR	CC-DCH-CCCV-CH-cycling	No
Shi	[55]	1S2P	ECM	ECM-ELM	dT	CC-DCH	No
Troxler	[54]	1S3P	ECM	ECM-ELM	dT	CC-DCH-CCCV-CH-cycling	No
Wang	[13]	1S8P	ECM	ECM-ELM	dR_{conn}	CC-DCH	Yes
Wu	[14]	1S8P	PCM	PCM-ELM	dR_{conn}	pulse-DCH	Yes
Yang	[17]	7S12P 1S2P	PCM	PCM-THM PCM-ELM	dT	CC-DCH, OC CC-cycling CC-DCH	Yes No

expected to avoid the high current peak through the more resistive connected cell. However, they have not discussed the influence of different cell connectors.

Dubarry et al. [53] presented an ECM based model of different topologies (1S2P, 1S3P and 2S2P) to examine the electrochemical behaviour of parallel cells or strings. The model is able to illustrate the transient behaviour of cell voltages and currents under a $dSOC$ cell-to-cell variation and can thus derive the balancing current between parallel connected cells or strings.

Capron et al. [52] have examined the effect of cell-to-cell variations within the initial SOC of cells on the temperature development within a battery module during CC discharge. For every cell, they used a PCM. Realising the thermal model of the module as a 2D computational fluid dynamics (CFD) model, allowed for depicting the forced air convection cooling and the temperature distribution within the module. However, the cells in the model have not been coupled electrically, wherefore the current distributions and balancing currents within the module could not be discussed.

2.2.2 Inhomogeneity due to thermal gradients

The effect of thermal gradients on the performance of individual lithium-ion cells has been investigated experimentally and by ECM simulation by Troxler et al. [54]. The temperature gradient within a single cell can be approximated by multiple parallel connected cells at different temperatures [51; 54], wherefore the results can also be considered relevant for multiple connected cells under thermal gradients. The cell performs as if under a higher uniform temperature than the theoretical average uniform temperature [54]. Within the cell, the local SOC diverges due to an asymmetric current distribution and due to the temperature dependence of the local OCV [51].

Both, Yang et al. [17] and Huang et al. [56], have exclusively examined the influence of a thermal gradient on the performance of a battery module by using a PCM-modelling approach. They have not considered dC or dR variations. While Yang et al. have realised an electric coupling between two parallel connected cells, Huang et al. have not. Although Yang et al. found that the dT variation did not strongly affect the output voltage or discharge capacity of the module, it did show a significant impact on the inhomogeneous current distribution between the cells. The capacity loss rate is found to increase with both, a higher operating temperature and a higher temperature gradient across the module. The influence of the system terminal (ST) position on the resulting currents is not examined. Huang et al. [56] have coupled a three dimensional thermal model (THM) to a p2D PCM and examined the performance of a 4S6P module during a CC-DCH under natural convection. Although they used PCMs for their simulated cells, they do not discuss the electrochemical influencing factors on the impedance of a cell but use the overall cell impedance for variation. They found, that under a dT imbalance within the module, cells at a lower temperature experience a smaller current due to their higher internal resistance. Cells with a higher temperature see a higher current which further increases the cell temperature and which intensifies the thermal imbalance within the module. These larger thermal gradients moreover lead to an increase in the variation of discharge capacities among the parallel connected cells. Huang et al. conclude, that a thermal gradient which is evolving across the battery module during operation may rather be due to operating conditions, cell connector design, cell arrangement and cooling conditions than due to the initial ambient temperature.

Klein et al. [57] have experimentally examined the influence of a linear thermal gradient across five parallel connected cells on the mean temperature as well as SOC- and current distribution within the module. Although their conceptual model to explain their experimental observations was ECM-based,

Klein et al. discussed the cell internal influencing factors on the cell impedance from an electrochemical point of view for different time scales. By examining both, lithium iron phosphate (LFP) and lithium nickel manganese cobalt oxide (NMC) based parallel connected cells, they were able to conclude that a higher temperature sensitivity in the impedance of a cell will cause larger current inhomogeneities when the module is subjected to a dynamic profile and that moreover a steeper OCV works against the effect of the inhomogeneous cell impedances. For both cell chemistries, the sensitivity to a thermal gradient was higher if the cells had been at a lower SOC and lower average temperature.

Shi et al. [55] have found, that a thermal gradient across a module leads to imbalanced currents between parallel connected cells and results in an increased capacity fade during ageing compared to a thermally homogeneous module [55].

Kamalisiahroudi et al. [49] have experimentally studied the influence of temperature differences on the current distribution within two parallel connected cells at low temperatures. By comparing the performance of 2P modules consisting of cells of the same type to that of a connection of different types of cells, they discussed the influence of a variation in cell resistance on the temperature distribution within the modules. Although they concluded that the connections of cells with uniform cell impedances will not necessarily result in a uniform temperature distribution, they did not discuss the influence of cell connectors on the current or temperature distribution within their experimental system.

2.2.3 Inhomogeneity due to cell connector resistances

The influence of cell connectors and their interconnection resistances on the performance of battery modules have been investigated by Offer et al. [4], Wu et al. [14], Wang et al. [13] and Grün et al. [50]. Offer et al. [4] have experimentally examined a 7S12P module under a cyclic load. They simulated this scenario based on a coupled ECM-ELM and concluded that within a parallel connected module, a current imbalance does not result from variations of cell impedance variations but from the interconnection resistances between the cells. Wu et al. [14] have enhanced this study while considering a PCM instead of a ECM as cell model and have found that the current inhomogeneity increases linearly with the number of parallel connected cells and increases logarithmically with an increasing ratio of cell connector resistance to cell impedance $\frac{R_{\text{conn}}}{R_{\text{cell}}}$. For this analysis they considered the ST at the side of the module. Under cyclic loading, there is no time for the SOCs of the cells to balance. Therefore, the cell close to the ST experiences high currents throughout the load, which leads to more generated heat in this region and an increased thermal gradient across the module. Wang et al. [13] based their studies on a 1S8P module which was modelled by a ECM per cell while being coupled to a ELM. They not only examined the influence of unequal cell connectors on the performance but also on the ageing behaviour of a battery module. Due to different positions of the ST, unequal cell connectors arose, which lead to a variation within the cell connector resistances. The cell located near the ST experienced a lower discharge state and a higher charge state, which resulted in a stronger ageing of that cell and which increased the current through the adjacent cells. Grün et al. [50] compared the impact of a dR variation between four parallel connected cells to that of different assembled cell connectors. They pointed out that the variation in cell impedance show a higher influence on current distribution and ageing than a variation in the electrical contact resistances R_{ws} . Moreover, the choice of the ST position as well as cell connector geometry and material (and thus R_{conn}) can help to symmetrise the load distribution.

2.2.4 Conclusion

What becomes clear from the literature review is that current literature lacks an investigation which compares the impact of cell-to-cell variations in capacity and impedance on the inhomogeneity in battery modules with that of thermal gradients and asymmetric cell connector design or defective cell contacts in one study using the same module topology and operation scenario for all influencing factors. Electric and thermal gradients across a battery module can occur simultaneously. In order to analyse their individual effects as well as their superposition, a holistic simulative investigation is sensible. Within a model environment, these effects can be readily separated which is rather challenging during experiments. Simulations using a multiphysics coupled model enables to investigate the different influences on inhomogeneity in battery modules during operation.

Therefore, Chapter 5 presents a model based framework including a PCM after Doyle, Fuller and Newman [58–61] with temperature dependent transport and kinetics parameters for each cell, while accounting for conservation of electric charge and energy between the cells to reach electrical consistency according to the respective module topology and cell interconnections. It is thus capable of investigating the influence of defective welding spot joints (though not shown in this thesis) and asymmetric cell connectors on the module inhomogeneity, while comparing the results to those occurring due to induced thermal gradients. Discussing the inhomogeneity within battery module operation from an electrochemical engineering point of view poses a valuable extension of previous work in the field, which is mainly focusing on aspects in electrical and mechanical engineering.

For reasons of reproducibility, model coupling equations for general $xSyP$ battery modules in different module contact scenarios are provided, which can be chosen from depicted flow charts. The focus of the study is to make general statements about the evolving current distribution between connected cells under operation. Therefore, the most simple module topology is used for this purpose, namely two parallel connected cells ($x=1, y=2$), as this topology seems most suitable to discuss the crucial effects of different influences on inhomogeneous current distribution in battery modules. Regarding the operation scenario, the focus is on CC-DCH at 1C. Of course, if insights into the performance of a specific battery module or system under a certain operation scenario are aimed at, then a battery module with more connected cells and more realistic load profiles are advantageous. However, as battery module topologies on the market are manifold (i.e. serial connected cells in a BMW i3 [62] or highly parallelised battery systems in Tesla cars [6; 7]), the aim of this study is to rather provide general statements using this generalised battery module. Focusing on only two connected cells has the advantage that the resulting current distribution between the cells is not smeared by additional connected cells within the topology. Thereby the results can be stated very clearly and the effects by the different influencing factors can be differentiated more easily.

3

Methodology

The following chapter sets the methodical context regarding the definition of topologies, the investigated cell, the statistic theory for parametric variation and correlation, physicochemical modelling and the thermal behaviour of lithium-ion cells.

3.1 Definition of topologies

In the following, the terminology regarding cell, battery module and battery system is defined for this thesis.

Lithium-ion cells exist in different formats, e.g. coin cells, cylindrical cells, prismatic cells or Pouch cells. They can be made of different cell chemistries, e.g. lithium cobalt oxide (LCO), lithium iron phosphate (LFP), lithium nickel cobalt aluminium oxide (NCA) or lithium nickel manganese cobalt oxide (NMC) versus lithium metal, graphite or lithium titanate oxide (LTO).

If multiple cells are connected in series or parallel, a battery module is generated. The voltage of a module determines from the sum of voltages of the serial connected cells. The capacity of the module determines from the sum of capacities of the cells connected in parallel. During the course of this thesis, the number of cells connected in series is denoted by x_S , the number of cells connected in parallel is denoted by y_P .

If multiple modules are connected in series or parallel, a battery system is generated.

3.2 Investigated cell

The cell under investigation is a commercial 3 Ah 26650 LiFePO₄-graphite cell (SonyUS26650FTC1). 1100 fresh cells of two batches (batch B1: cell 1-600, batch B2: cell 601-1100) have been examined

Table 3.1: Nominal data of the investigated cell Sony US26650FTC1.

Parameter	Symbol	Value
Nominal capacity	C_N	3 Ah
Nominal voltage	V_N	3.2 V
Max. charge voltage	$V_{ch,max}$	3.60 ± 0.05 V
Min. discharge voltage	$V_{disch,min}$	2 V
Ohmic impedance (1 kHz, AC)	$R_{i,AC}$	18 m Ω
Max. continuous charge current	$I_{ch,max}$	2.85 A
Max. continuous discharge current	$I_{disch,max}$	20 A
Temperature range charge	$T_{amb,ch}$	0 to 45 °C
Temperature range discharge	$T_{amb,disch}$	-20 to 60 °C
Mass	m_{cell}	84.5 g

experimentally (compare Chapter 4). The batches are defined by a code printed on each individual cell and which corresponds to the production date. At the time of the experimental investigation the cells of batch B1 had an age of 9 months, the cells of batch B2 of 10 months. Table 3.1 shows the nominal data of the investigated cell. This cell is also used for parametrising the developed multiscale multiphysics model which is presented in Chapter 5.

3.3 Statistics

For the statistic analysis of the measured cell parameters presented in Chapter 4, statistic theory for parametric variation and correlation is used based on [63].

3.3.1 Parametric variation

It is assumed that all cell parameters are normally distributed around their respective mean value μ [9; 19; 20].

The mean value of a parameter x calculates

$$\mu_x = \frac{1}{n} \sum_{i=1}^n x_i \quad (3.1)$$

where n is the number of data points, i.e. the number of investigated cells [63, p. 50]. In a normal distribution the parameter's standard deviation σ around the mean is defined as

$$\sigma_x = \sqrt{\frac{1}{n-1} \sum_{i=1}^n (x_i - \mu_x)^2} \quad (3.2)$$

68.1 % of the values lie within the interval $\pm\sigma_x$ around μ_x [63, p. 65].

The coefficient of variation (COV) σ_x/μ_x is a relative measure of a parameter's variation independent of scale (relative variation). It is thus used to compare the variation of different parameters in order to set them in context to each other [63, p. 68].

3.3.2 Parametric correlation

Investigating the correlation between two parameters using a set of n cells offers a method to describe the dependency between the two parameters. The correlation coefficient ρ_{xy} of two variables x and y calculates

$$\rho_{xy} = \frac{\sum_{i=1}^n (x_i - \mu_x)(y_i - \mu_y)}{\sqrt{\sum_{i=1}^n (x_i - \mu_x)^2 \cdot \sum_{i=1}^n (y_i - \mu_y)^2}} \quad (3.3)$$

with μ_x and μ_y being the mean values of the two parameters. It measures the strength of the linear dependency of two parameters. The correlation coefficient ranges from -1 to 1 [63, p. 126]. $\rho_{xy} = 0$ means that there is no correlation between parameter x and y , $\rho_{xy} = 1$ implies a total positive and $\rho_{xy} = -1$ a total negative linear dependency respectively. In addition, correlation coefficients are classified as follows in this thesis:

$$\begin{aligned} |\rho_{xy}| \leq 0.3 & \quad \text{weak correlation} \\ 0.3 < |\rho_{xy}| \leq 0.7 & \quad \text{moderate correlation} \\ 0.7 < |\rho_{xy}| & \quad \text{strong correlation} \end{aligned} \quad (3.4)$$

These classes have been chosen due to the coefficient of determination (COD) of the class limits. The COD ρ_{xy}^2 denotes the ratio of dependency of the variation of parameter x on the variation of parameter y [63, p. 151]. For a correlation coefficient $\rho_{xy} = 0.3$ between two parameters, the COD equals $\rho_{xy}^2 = 0.09 = 9\%$. Thus a weak correlation between two parameters x and y means that up to 9% of the variation of parameter x depends on the variation of parameter y . For $\rho_{xy} = 0.7$ the COD equals $\rho_{xy}^2 = 0.49 = 49\%$. Thus a strong correlation means that more than 49% of the variation of parameter x depends on the variation of parameter y . All correlation values in between $0.3 < |\rho_{xy}| \leq 0.7$ are classified as a moderate correlation.

3.4 Physicochemical modelling

The physicochemical behaviour of a lithium-ion cell can be described by a p2D PCM after Doyle, Fuller and Newman [58–61]. The model is based on the theory of porous electrodes and concentrated solutions and accounts for the conservation of charge and mass.

It can be used to model the behaviour of lithium-ion cells of different formats and of different cell chemistries (compare Chapter 3.1). The cell used for investigation within this thesis is a commercial 3 Ah 26650 LiFePO₄-graphite cell (SonyUS26650FTC1) (compare Chapter 3.2). Therefore, where appropriate, the focus of the following sections is set on describing cylindrical cells with LiFePO₄-LiC₆ active material.

3.4.1 Structure of a cylindrical lithium-ion cell

A cylindrical lithium-ion cell is comprised of a wound jelly roll (compare Figure 3.1) within a casing. The jelly roll consists of different layers: The double coated negative porous electrode material (dark grey) on a copper current collector foil (orange), followed by a separator (dashed), the double coated positive porous electrode material (green) on an aluminium current collector foil (light grey) and a

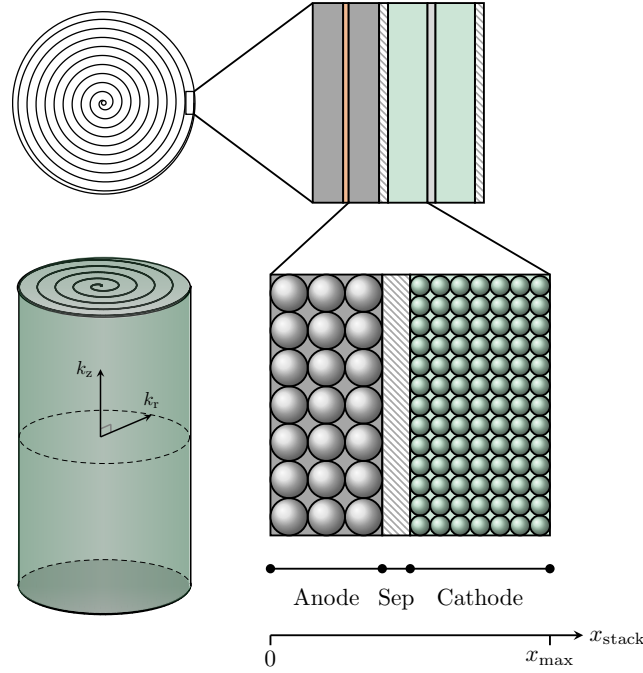


Figure 3.1: Schematic of a jelly roll and the different layers.

second separator (dashed). The porous electrodes consist of active material particles and electrolyte filled pore volume. The inner cell stack (one anode, separator and cathode each) can be reduced to a 1D interval, which represents the whole cylindrical cell in the PCM.

3.4.2 Governing equations within the p2D Newman-model

The governing equations of the p2D Newman-model are shown in Table 3.2. Within the porous electrodes i ($i \in \{\text{neg, pos}\}$), spherical particles with a mean particle radius $r_{p,i}$ (m) are assumed. This leads to an active specific surface area $a_v = \frac{3\varepsilon_{s,i}}{r_{p,i}}$ (m^{-1}), where $\varepsilon_{s,i}$ (no unit) is the active material volume fraction within the respective electrode.

These equations are solved for four variables within three domains in 1D (anode, separator and cathode) and within the pseudo r -dimension representing the active material particles. At each coordinate within both of the porous electrodes, both, the solid and liquid phase are assumed to exist. For the solid phase (subscript s) spherical particles with particle radius r_p are modelled for both of the porous electrodes. For the liquid phase (subscript l) the electrolyte properties are provided. The four variables, for which the equations are solved, are the electric potential of the solid phase (ϕ_s) and liquid phase (ϕ_l) respectively, as well as their corresponding lithium-ion concentrations (c_s in the particle domain and c_l in the porous electrode domain).

3.4.3 Electrochemical reactions

The electrochemical reactions occurring at the electrode-electrolyte interface of a lithium-ion cell are given by the negative electrode reaction (compare Equation 3.5) and the positive electrode reaction (compare Equation 3.6) - a combination of both gives the net reaction (compare Equation 3.7). In the following the equations are given for a $\text{LiFePO}_4\text{-LiC}_6$ cell as functions of stoichiometry x and y (no

Table 3.2: Governing equations within the p2D Newman-model (PCM). s=solid phase, l=liquid phase.

Governing Equations	Section	Mathematical Expression	Boundary conditions
Kinetics			
Butler-Volmer equation	s-l	$j_{Li} = j_0 \left(\exp \left(\frac{\alpha_a \eta_{CT} F_{const}}{R_{const} T} \right) - \exp \left(- \frac{\alpha_c \eta_{CT} F_{const}}{R_{const} T} \right) \right)$	
Exchange current density	s-l	$j_0 = k_c^{\alpha_a} k_a^{\alpha_c} (c_{s,max} - c_{s,surf})^{\alpha_a} (c_{s,surf})^{\alpha_c} \left(\frac{c_l}{c_{l,ref}} \right)^{\alpha_a}$	$c_{s,surf} = c_s _{r=r_p}$
Electrode overpotential	s-l	$\eta_{CT} = \phi_s - \phi_l - E_{eq}$	
Charge balance			
Electric flux	s(r)	$i_s = -\sigma_{s,eff} \nabla \phi_s$	
Ionic flux	l(x)	$i_l = -\kappa_{l,eff} \nabla \phi_l + \frac{2\kappa_{l,eff} R_{const} T}{F_{const}} \left(1 + \frac{\partial \ln f_{\pm}}{\partial \ln c_l} \right) (1 - t_+) \nabla \ln c_l$	$i_l(x, t) _{x=0} = 0$ $i_l(x, t) _{x=x_{stack}} = 0$
Charge conservation	s-l	$\frac{\partial i_s(x, t)}{\partial x} + \frac{\partial i_l(x, t)}{\partial x} = 0$	
Mass balance			
Species conservation s	s(r)	$\frac{\partial c_s}{\partial t} = D_s \left(\frac{\partial^2 c_s}{\partial r^2} + \frac{2}{r} \frac{\partial c_s}{\partial r} \right)$	$-D_s \frac{\partial c_s}{\partial r} _{r=0} = 0$ $-D_s \frac{\partial c_s}{\partial r} _{r=r_p} = j_{Li}$
Species conservation l	l(x)	$\varepsilon_l \frac{\partial c_l}{\partial t} = \nabla (D_{l,eff} \frac{\partial c_l(x, t)}{\partial x}) + a_v j_{Li} (1 - t_+)$	$D_{l,eff} \frac{\partial c_l(x, t)}{\partial x} _{x=0} = 0$ $D_{l,eff} \frac{\partial c_l(x, t)}{\partial x} _{x=x_{stack}} = 0$

unit) under the assumption of $x = y$.



3.4.4 Analytical equations enhancing the p2D Newman-model

The equilibrium potentials for a Li_xC_6 negative electrode $E_{\text{eq,neg}}$ (compare Equation 3.8) and a Li_yFePO_4 positive electrode $E_{\text{eq,pos}}$ (compare Equation 3.9) have been approximated by Safari et al. [64] depending on the stoichiometry x of the negative and y of the positive electrode (no unit) respectively:

$$\begin{aligned} E_{\text{eq,neg}}(x) = & 0.6379 + 0.5416 \exp(-305.5309x) + 0.044 \tanh\left(-\frac{x - 0.1958}{0.1088}\right) \\ & - 0.1978 \tanh\left(\frac{x - 1.0571}{0.0854}\right) - 0.6875 \tanh\left(\frac{x + 0.0117}{0.0529}\right) \\ & - 0.0175 \tanh\left(\frac{x - 0.5692}{0.0875}\right) \end{aligned} \quad (3.8)$$

$$\begin{aligned} E_{\text{eq,pos}}(y) = & 3.4323 - 0.8428 \exp(-80.2493(1 - y)^{1.3198}) \\ & - 3.2474 \cdot 10^{-6} \exp(20.2645(1 - y)^{3.8003}) \\ & + 3.2482 \cdot 10^{-6} \exp(20.2646(1 - y)^{3.7995}) \end{aligned} \quad (3.9)$$

The changes of the electrodes' equilibrium potentials with temperature, the so called entropic coefficients $\frac{dE_{\text{eq}}}{dT}$, influence the reversible heat generated in the cell during the electrochemical reaction. Guo et al. [65] give an equation for the entropic coefficient of a LiC_6 -electrode (compare Equation 3.10). Li et al. [66] have approximated entropy measurement data from Dodd [67] for a LiFePO_4 -electrode (compare Equation 3.11). Both entropic coefficients are given in mV K^{-1} . The stoichiometries x and y have no unit.

$$\begin{aligned} \frac{dE_{\text{eq,neg}}(x)}{dT} = & (0.00527 + 3.29927 \cdot x - 91.79326 \cdot x^2 + 1004.91101 \cdot x^3 \\ & - 5812.27813 \cdot x^4 + 19329.75490 \cdot x^5 - 37147.89470 \cdot x^6 + 38379.18127 \cdot x^7 \\ & - 16515.05308 \cdot x^8) \cdot (1 - 48.09287 \cdot x + 1017.23480 \cdot x^2 - 10481.80419 \cdot x^3 \\ & + 59431.30001 \cdot x^4 - 195881.64880 \cdot x^5 + 374577.31520 \cdot x^6 - 385821.16070 \cdot x^7 \\ & + 165705.85970 \cdot x^8)^{-1} \end{aligned} \quad (3.10)$$

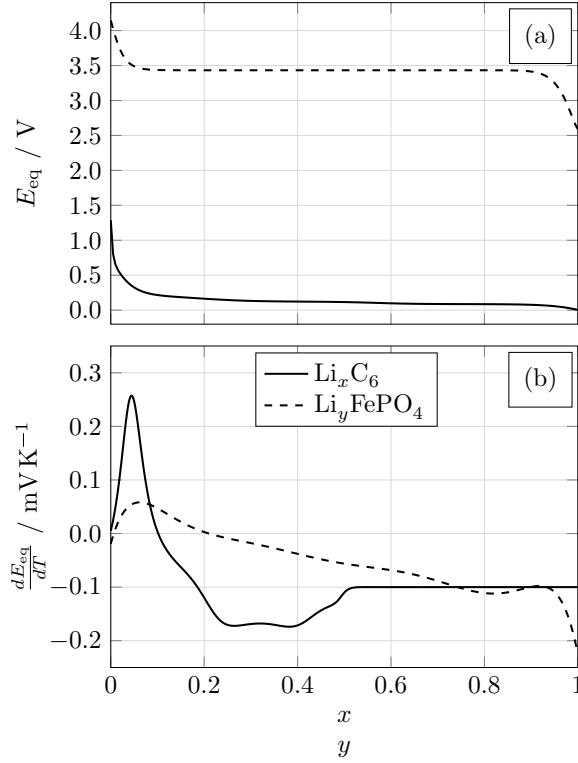


Figure 3.2: Equilibrium potentials (a) and entropic coefficients (b) of the Li_xC_6 and Li_yFePO_4 electrodes as a function of stoichiometry x and y respectively.

$$\begin{aligned} \frac{dE_{\text{eq,pos}}(y)}{dT} = & 1000 \cdot (-0.35376y^8 + 1.3902y^7 - 2.2585y^6 + 1.9635y^5 - 0.98716y^4 \\ & + 0.28857y^3 - 0.046272y^2 + 0.0032158y - 1.9186 \cdot 10^{-5}) \end{aligned} \quad (3.11)$$

The implemented equations for equilibrium potentials and entropic coefficients of the Li_xC_6 and Li_yFePO_4 electrodes as a function of stoichiometry x and y respectively are depicted in Figure 3.2.

The tortuosity quantifies the change of a transport path through a porous electrode or separator. The Bruggeman relation [68] (Equation 3.12) states the dependency of porosity ε_1 and tortuosity τ within a porous electrode consisting of spherical particles:

$$\tau = \varepsilon_1^{1-\alpha_{\text{Brug}}} \quad (3.12)$$

$\alpha_{\text{Brug}} = 1.5$ is the Bruggeman coefficient which has been determined empirically [68].

For more complex structures consisting of other than spherical particles, different values for α have to be determined. In this case the general equation for tortuosity is to be used [69]:

$$\tau = f\varepsilon_1^{1-\alpha} \quad (3.13)$$

The relationship between tortuosity and porosity can be expressed by the MacMullin number N_M :

$$N_M = \frac{\tau}{\varepsilon_1} \quad (3.14)$$

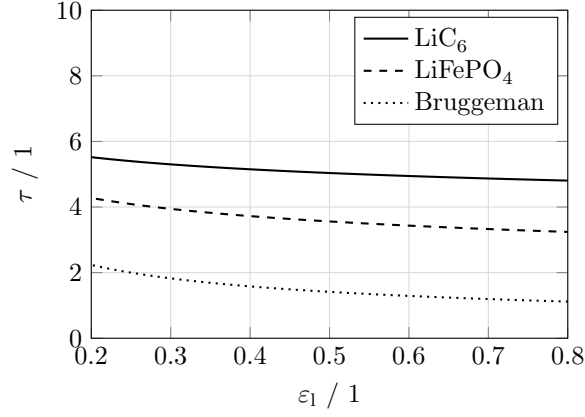


Figure 3.3: Tortuosity of the LiC₆ and LiFePO₄ electrodes as a function of porosity ϵ_1 compared to the Bruggeman relation.

Landesfeind et al. [69] have examined $\tau\epsilon$ -relationships by fitting experimental data of porosity and tortuosity for different porous electrodes and separators. The following relations are attributed to the LiC₆- and LiFePO₄-electrode and the separator respectively:

$$N_{M,\text{LiC}_6} = 4.7\epsilon_{1,\text{LiC}_6}^{-1.1} \quad (3.15)$$

$$N_{M,\text{LiFePO}_4,\text{lowC}} = 3.1\epsilon_{1,\text{LiFePO}_4}^{-1.6} \quad (3.16)$$

$$N_{M,\text{Sep1}} = \epsilon_{1,\text{Sep}}^{-3.5} \quad (3.17)$$

These MacMullin numbers are used to account for the tortuosity within the respective domains by calculating the effective electrolyte transport properties: Electrolyte conductivity κ_1 and electrolyte diffusivity D_1 .

$$\kappa_{1,\text{eff}} = \frac{1}{N_M} \kappa_1 = \frac{\epsilon_1}{\tau} \kappa_1 \quad (3.18)$$

$$D_{1,\text{eff}} = \frac{1}{N_M} D_1 = \frac{\epsilon_1}{\tau} D_1 \quad (3.19)$$

The implemented equations for the tortuosity of the LiC₆ and LiFePO₄ electrodes as a function of porosity ϵ_1 are depicted in Figure 3.3.

The transport properties of the electrolyte D_1 (m² s⁻¹), κ_1 (S m⁻¹) and $\frac{\partial \ln f_{\pm}}{\partial \ln c_1}$ (no unit) are described in dependency of lithium concentration c_1 (mol l⁻¹) and cell temperature T_{cell} (K) according to Valøen et al. [70]. The electrolyte diffusivity $D_1(c_1, T_{\text{cell}})$ is implemented as

$$D_1(c_1, T_{\text{cell}}) = (10^{-4.43 - \frac{54}{T_{\text{cell}} - 229 - 5 \cdot c_1} - 0.22 \cdot c_1}) \cdot 10^{-4} \quad (3.20)$$

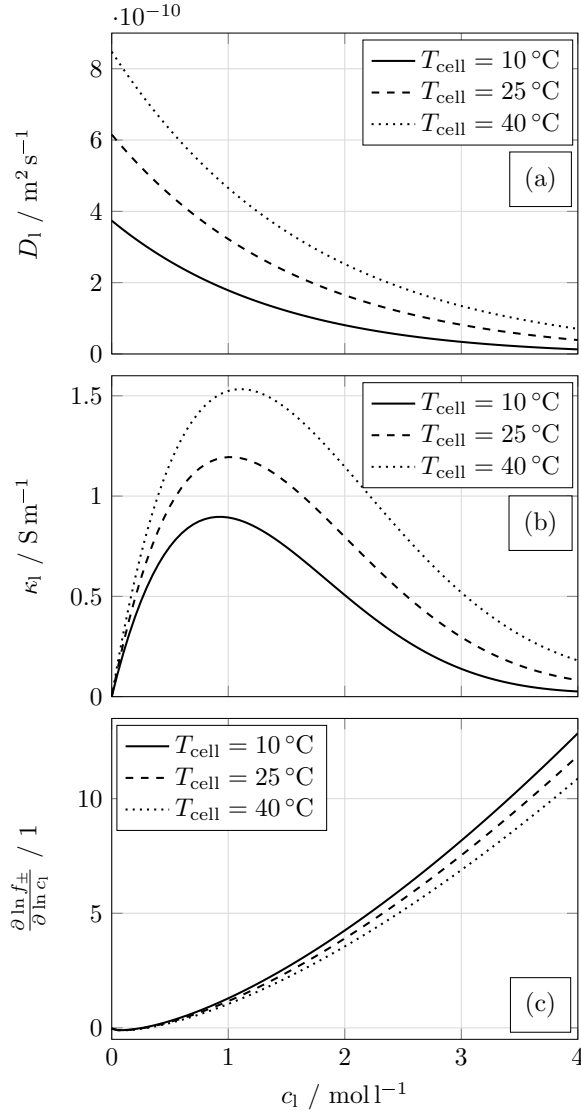


Figure 3.4: Transport parameters of the electrolyte as a function of lithium concentration c_1 and cell temperature T_{cell} : (a) Diffusion coefficient D_1 , (b) Ionic conductivity κ_1 and (c) Activity dependency $\frac{\partial \ln f_{\pm}}{\partial \ln c_1}$.

The electrolyte conductivity $\kappa_1(c_1, T_{\text{cell}})$ is described by

$$\begin{aligned} \kappa_1(c_1, T_{\text{cell}}) = \frac{c_1}{10} &(-10.5 + 0.074T_{\text{cell}} - 6.96 \cdot 10^{-5}T_{\text{cell}}^2 + 0.668c_1 - 0.0178c_1T_{\text{cell}} \\ &+ 2.8 \cdot 10^{-5}c_1T_{\text{cell}}^2 + 0.494c_1^2 - 8.86 \cdot 10^{-4}c_1^2T_{\text{cell}})^2 \end{aligned} \quad (3.21)$$

The activity dependency $\frac{\partial \ln f_{\pm}}{\partial \ln c_1}(c_1, T_{\text{cell}})$ is given as

$$\frac{\partial \ln f_{\pm}}{\partial \ln c_1}(c_1, T) = \frac{1}{1 - t_+} (0.601 - 0.24c_1^{0.5} + 0.982(1 - 0.0052(T_{\text{cell}} - 298 \text{ K}))c_1^{1.5}) - 1 \quad (3.22)$$

The implemented equations for the transport parameters of the electrolyte as a function of lithium concentration c_1 and cell temperature T_{cell} are depicted in Figure 3.4.

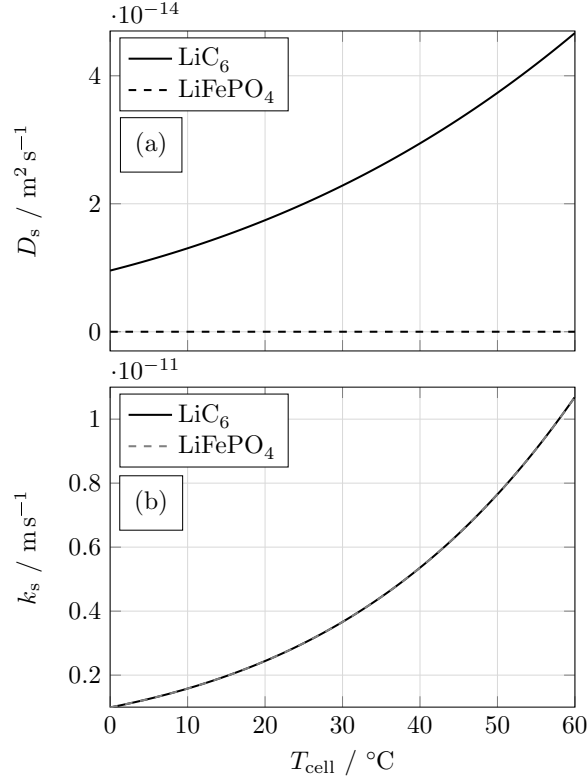


Figure 3.5: Diffusivity (a) and reaction rate (b) of the LiC_6 and LiFePO_4 electrodes as a function of cell temperature T_{cell} . Note, that the diffusivity of the LiFePO_4 electrode in (a) does also show an exponential behaviour but has reference diffusion coefficient $D_{\text{s,ref}}$ which is four magnitudes smaller than for the LiC_6 electrode. Note, that in (b) the reaction rates curves of both electrodes are the same as they are implemented using the same reference reaction rates and activation energies.

The diffusivity and reaction rate in the electrodes are assumed to follow a temperature dependent Arrhenius behaviour according to Guo et al. [65; 71].

The solid phase diffusivity $D_s(T_{\text{cell}})$ ($\text{m}^2 \text{s}^{-1}$) is implemented as

$$D_s(T_{\text{cell}}) = D_{\text{s,ref}} \cdot \exp\left(-\frac{E_{\text{a},D_s}}{R_{\text{const}}}\left(\frac{1}{T_{\text{cell}}} - \frac{1}{T_{\text{ref}}}\right)\right) \quad (3.23)$$

The reaction rate $k_s(T_{\text{cell}})$ (m s^{-1}) is described by

$$k_s(T_{\text{cell}}) = k_{\text{ref}} \cdot \exp\left(-\frac{E_{\text{a},k}}{R_{\text{const}}}\left(\frac{1}{T_{\text{cell}}} - \frac{1}{T_{\text{ref}}}\right)\right) \quad (3.24)$$

The implemented equations for the diffusivity and reaction rate of the LiC_6 and LiFePO_4 electrodes as a function of cell temperature T_{cell} are depicted in Figure 3.5.

3.5 Thermal behaviour of lithium-ion cells

The behaviour of a lithium-ion cell does not only depend on the applied *C-Rate* but also on its ambient temperature [72]. More precisely, the temperature of a cell affects both, the cell performance [73; 74]

and cell ageing [26–31; 75]. A cell’s charge and discharge characteristics depend on its electrodes’ chemistries. Each electrode chemistry has a unique OCV, which is temperature dependent [76]. The OCV of a full cell determines from the balancing of the two electrodes and their OCVs. It is thus temperature dependent as well [76; 77]. The main operating temperature of lithium-ion cells generally lies between 0 °C and 40 °C for charging [78] and between –20 °C and 50 °C for discharging [78]. Even if a cell is operated or stored within this temperature range, differences can still be observed in the cell behaviour.

As pointed out in the introduction, a cell degrades faster at high cell storage temperatures [26–28] due to stronger electrolyte decomposition and SEI growth [75] which leads to cell capacity decrease and cell resistance increase [29; 75]. Considering the same cell as investigated in this thesis, the rate of the cell capacity decrease has been found to slow down in a square root dependence over time [75] and the loss of active material has been found to only make up a minor contribution [75]. A cell which has been operated at a highway driving cycle at high temperatures has experienced smaller capacity fade, which has been attributed to reduced stress and degradation by (de-)intercalation processes at high temperatures [28; 30]. During an experimental cycle ageing study considering the same cell as investigated in this thesis, both, the cell capacity loss and the resistance increase have been found to strongly depend on the depth of cycle and average SOC of the cell [75]. The influence of temperature on cell degradation during cell cycling on the other hand showed no additional influence after the cyclic ageing results had been corrected for the calendar ageing results [75].

At high ambient temperatures electrolyte evaporation can occur [79], whereas it does not play a role at normal ambient temperatures [80]. Although the aim is to use an electrolyte which shows a high conductivity over a wide temperature range (i.e. ideally from –40 °C and 80 °C), the perfect electrolyte is not available yet and a certain trade-off needs to be accepted [81]. Furthermore, at high temperatures the passivation layer will start to solubilise and break, the polyethylen (PE) and polypropylen (PP) separator components will start to melt and the positive active material will start to decompose which can – dependent on the chemistry – result in O₂ emission which will react with the solvents [82].

At sub-ambient temperatures high charging currents can result in lithium plating [83–86], which might lead to dendrite growth [66; 87; 88] which can finally result in an internal short circuit within the cell [31; 86]. Moreover, at temperatures $T_{\text{amb}} < -20$ °C, electrolyte freezing can occur [73] which results in a reduced discharge capacity and in an increased cell impedance [73; 89].

3.5.1 Thermal modelling

This chapter sets the context for modelling the thermal behaviour of cylindrical cells. A detailed description of the thermal model used in this thesis is given in Chapter 5.2.2.

During the operation of a cell, heat is generated [90] which is partly stored in the cell due to the cell’s heat capacity and partly dissipated to the environment by conduction (e.g. via the cell terminals), convection (via surrounding air or liquid) and by radiation. As heat dissipation does only occur at the surface of the cell, the temperature at the cell’s centre is higher than the one at the cell’s surface. The temperature within a cell is thus not homogeneous.

This discrepancy has for example been investigated by Osswald et al. [91] and Erhard et al. [92], who have modified a commercial 26650 cell in order to measure and simulate its local potentials. During the modification process they have also inserted a thermocouple within the inner mandrel of the jelly roll

[91]. By furthermore attaching a thermocouple to the surface of the cell, this allowed for monitoring both, the surface and the centre temperature of the cell during subsequent measurements. During the conducted CC-DCH tests at different C -Rates $\in \{0.5, 1, 2\}C$, the temperature difference within the cell increased up to 5 K ($2C$), 1.5 K ($1C$) and 0.5 K ($0.5C$) [92]. Similar values have also been measured by Zhang et al. [74].

When aiming to model the behaviour of a cell, the choice of the thermal model dimension determines how well the temperature within a cell can be resolved. A 1D thermal model allows to depict the temperature decrease between centre and surface by a line plot in radial direction of the cylindrical cell. A 2D thermal model allows to show surface or contour temperature plot of the circular cell area. A 3D thermal model furthermore allows to resolve the temperature distribution over the height of the cylindrical cell in a volumetric plot. Thus, choosing a higher model dimension allows for higher resolution but it does also imply higher computational effort. Therefore, the thermal model dimension should be chosen carefully depending on the aim of the investigation.

The modelling part of this thesis aims at examining the inhomogeneity in small battery modules. The module is operated at $T_{\text{amb}} = 25^\circ\text{C}$, $v_{\text{air}} = 1\text{ ms}^{-1}$ and at moderate C -Rates. As seen in the investigation by Erhard et al. [92], a CC-DCH at C -Rate $\leq 1C$ results in temperature gradients within the cell less than 1.5 K. As the aim of the present investigation is to examine the inhomogeneity of battery modules and not cells, the temperature gradient across the module is of interest and not the one within the cells. The latter is therefore decided to be neglected. In this case, each of the connected cells can be represented by a 0D lumped thermal model, which solves the heat balance equation in every time step (compare Chapter 5.2.2). The output is one temperature per cell.

When being coupled to the PCM of the respective cell, this cell temperature can be used to adjust several cell internal model parameters. As pointed out in Chapter 3.4.4, this includes the temperature dependence of the electrodes' OCVs [65–67] as well as the transport properties of the electrolyte [70] and the kinetics parameters of the electrodes [65; 71].

In order to parametrise a thermal cell model, different thermal cell parameters such as the heat capacity and thermal conductivity need to be implemented. Although for a 0D thermal model the thermal conductivity is not needed, Chapter 3.5.2 presents equations, how all of these parameters can be calculated.

If the cell or battery module is exposed to surrounding air, natural or forced convection will occur depending on the applied thermal management. In order to sufficiently account for the dissipated heat by convection in a thermal model, either a CFD model can be integrated or the convective heat transfer coefficients must be calculated according to the topology and ambient conditions. CFD simulations require careful meshing of the topology's geometry especially at higher thermal model dimensions. This results in multiple mesh elements, for which the laminar and turbulent fluid dynamics equations need to be solved. As this leads to a high computational effort, calculating the convective heat transfer coefficients and using them in heat balance equations can offer an alternative. The approach how to calculate the convective heat transfer coefficient for different topologies is described in Chapter 3.5.3.

3.5.2 Calculation of thermal cell parameters

During thermal modelling of a cell's behaviour, the thermal parameters of the cell such as its heat capacity and thermal conductivities must be parametrised. The heat capacity of a cell defines how

Table 3.3: Thermal properties of the cell components and the calculated cell properties after Chen et al. [94] and Bandhauer et al. [90]. Exponent glossary: m=measured, a=assumed.

Component	t μm	m wt%	ρ kg m^{-3}	k $\text{W m}^{-1} \text{K}^{-1}$	c_p $\text{J kg}^{-1} \text{K}^{-1}$
Cu current collector	11 ^m	11.5 ^m	8933 ^[97]	398 ^[97]	385 ^[97]
LiC ₆ electrode	61 ^m	19.2 ^m	1347.3 ^[94]	1.0 ^[94]	1437.4 ^[94]
Separator	18 ^m	2.7 ^m	1009.0 ^[94]	0.3 ^[94]	1978.2 ^[94]
LiFePO ₄ electrode	79 ^m	27.9 ^m	1500.0 ^[98]	1.5 ^[98]	1260.2 ^[98]
Al current collector	16 ^m	4.2 ^m	2702 ^[97]	238 ^[97]	903 ^[97]
Can (S.S. AISI-304)		22.2 ^a	7900 ^[97]	14.6 ^[97]	477 ^[97]
Electrolyte		12.5 ^a	1130.0 ^[94]	0.6 ^[94]	2055.1 ^[94]

well a cell can store heat. It can be calculated from the respective mass ratios [93]:

$$c_p = \frac{\sum_i \rho_i V_i c_{p,i}}{\sum_i \rho_i V_i} \quad (3.25)$$

Due to a cell's layered or wound nature, its thermal conductivity is anisotropic (compare Figure 3.1): The thermal conductivity through the layers of a cell k_r (i.e. in radial direction of a cylindrical cell), is one to two magnitudes smaller than along the layers of a cell k_z (i.e. in axial direction of a cylindrical cell) [94–96]. This is due to the fact that the current collectors support the thermal conductivity along the layers whereas the electrode material and separator constrain it through the layers. Similar to the heat capacity of a cell, also the thermal conductivities can be calculated from the component material layers' thicknesses t_i and thermal conductivities k_i [90; 94]:

$$k_r = \frac{\sum_i t_i}{\sum_i \frac{t_i}{k_i}} \quad (3.26)$$

$$k_z = \frac{\sum_i t_i k_i}{\sum_i t_i} \quad (3.27)$$

In order to calculate the thermal parameters for the investigated cell, the values for the cell components are listed in Table 3.3. Furthermore, the measured component thicknesses and mass ratios are given.

The heat capacity of the cell stack calculates to $c_{p,\text{cell}} = 1300 \text{ J kg}^{-1} \text{ K}^{-1}$ and the thermal conductivities have been determined to be $k_r = 1 \text{ W m}^{-1} \text{ K}^{-1}$ and $k_z = 45 \text{ W m}^{-1} \text{ K}^{-1}$. These values are in a similar range as values which have been measured by Drake et al. [96] for a 26650 cell ($c_{p,\text{cell,lit}} = 1605 \pm 80 \text{ J kg}^{-1} \text{ K}^{-1}$, $k_{r,\text{lit}} = 0.15 \pm 0.01 \text{ W m}^{-1} \text{ K}^{-1}$, $k_{z,\text{lit}} = 32 \pm 1.6 \text{ W m}^{-1} \text{ K}^{-1}$). The measured $k_{r,\text{lit}}$ value is lower than the component conductivities. This is explained to be due to the fact that within the fitting model, multiple thermal contact resistances had been taken into account, which lower the radial thermal conductivity [96].

3.5.3 Calculation of convective heat transfer coefficients

The convective heat transfer coefficient h_{conv} depends on dimensionless parameters such as Nusselt Nu, Reynolds Re and Prandtl Pr number as well as on the geometry of the overflow cell or bunch of cells respectively.

3.5.3.1 Convective heat transfer coefficient for a single cylindrical cell

The Nusselt number Nu relates the convective heat transfer coefficient h_{conv} to the characteristic overflow length L of the object and the thermal conductivity of the fluid k_{air} [99]. It thus defines the dimensionless heat transfer to an overflowing fluid [99].

$$\text{Nu} = \frac{h_{\text{conv}}L}{k_{\text{air}}} \quad (3.28)$$

The characteristic length L of a cylindrical cell equals half the circumference of the cell, with r_{cell} being the radius of the cell:

$$L = \pi r_{\text{cell}} \quad (3.29)$$

Gnielinski [100] has defined the mean Nusselt number Nu_{mean} for perpendicular flow against cylinders:

$$\text{Nu}_{\text{mean}} = 0.3 + \sqrt{\text{Nu}_{\text{lam}}^2 + \text{Nu}_{\text{turb}}^2} \quad (3.30)$$

Nu_{lam} and Nu_{turb} are the Nusselt numbers for laminar and turbulent flow, respectively [100].

$$\text{Nu}_{\text{lam}} = 0.664\sqrt{\text{Re}}\sqrt[3]{\text{Pr}} \quad (3.31)$$

$$\text{Nu}_{\text{turb}} = \frac{0.037\text{Re}^{0.8}\text{Pr}}{1 + 2.443\text{Re}^{-0.1}(\text{Pr}^{2/3} - 1)} \quad (3.32)$$

Re is the Reynolds number, Pr is the Prandtl number. Pr defines the ratio of the viscosity of the fluid ν to its temperature conductivity $\frac{k}{\rho c_p}$. It is a material value and relates the diffusive impulse transport to diffusive heat transport in friction afflicted fluids. [99]

$$\text{Pr} = \frac{\nu_{\text{air}}\rho_{\text{air}}c_{p,\text{air}}}{k_{\text{air}}} \quad (3.33)$$

Re relates the inertia force to the friction force. It defines whether a flow stays laminar stable or becomes turbulent [101].

$$\text{Re} = \frac{v_{\text{air}}L}{\nu_{\text{air}}} \quad (3.34)$$

The equations for the Nusselt number are valid for the following ranges of Re and Pr [101]:

$$10 < \text{Re} < 10^7 \quad (3.35)$$

$$0.6 < \text{Pr} < 1000 \quad (3.36)$$

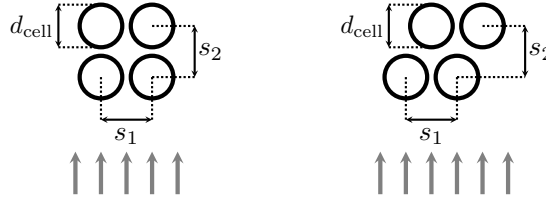


Figure 3.6: Definition of the values s_1 and s_2 for a bunch of four cells in aligned arrangement (left) and staggered arrangement (right). These values are used to define the side spacing ratio $a = s_1/d_{\text{cell}}$ and the back spacing ratio $b = s_2/d_{\text{cell}}$ of the arrangement. Adapted after [101].

For a single cylindrical 26650 cell, $\text{Re} = 2553$, $\text{Nu}_{\text{lam}} = 30$ and $\text{Nu}_{\text{turb}} = 18$ which results in $\text{Nu}_{\text{mean}} = 35$ and consequently $h_{\text{conv}} = 22.5 \text{ W m}^{-2} \text{ K}^{-1}$ for $v_{\text{air}} = 1 \text{ m s}^{-1}$, $k_{\text{air}} = 0.0259 \text{ W m}^{-1} \text{ K}$, $\nu_{\text{air}} = 1.6 \times 10^{-5} \text{ m}^2 \text{ s}^{-1}$, $\text{Pr} = 0.72$ and $T = 25 \text{ }^\circ\text{C}$.

Regarding the material values for the surrounding air, the mean air temperature $T_{\text{air,mean}}$ should be used [101]:

$$T_{\text{air,mean}} = \frac{T_{\text{air,in}} + T_{\text{air,out}}}{2} \quad (3.37)$$

$T_{\text{air,in}}$ is the air temperature entering the investigated system, $T_{\text{air,out}}$ is the air temperature exiting the investigated system. For small systems of connected cells, this differentiation between entering and exiting air temperature can be neglected.

3.5.3.2 Convective heat transfer coefficient for multiple cylindrical cells

As an approximation for the convective heat transfer coefficient within a row or bunch of cells, an effective convective heat transfer coefficient $h_{\text{conv,eff}}$ can be calculated, which can be assumed to be valid for each of the cells. $h_{\text{conv,eff}}$ depends on the respective Nusselt number Nu_{row} or Nu_{bunch} which are defined using two arrangement related variables: The voidage percentage ψ and the arrangement factor f_A of the bunch of cells. These two variables both depend on the respective side spacing ratio $a = s_1/d_{\text{cell}}$ and back spacing ratio $b = s_2/d_{\text{cell}}$ of the arrangement. The definition of the values s_1 and s_2 is shown in Figure 3.6 for a bunch of four cells in an aligned and staggered arrangement.

During the calculation of Nu , it is distinguished whether a horizontal row of cells or a bunch of cells is investigated.

Regarding a horizontal row of cells, the Reynolds number Re adapts to $\text{Re}_{\psi_{\text{row}}}$ according to the changed air velocity within the voidage percentage ψ_{row} [101]:

$$\psi_{\text{row}} = \frac{\pi}{4a} \quad (3.38)$$

$$\text{Re}_{\psi_{\text{row}}} = \frac{v_{\text{air}} L}{\psi_{\text{row}} \nu_{\text{air}}} \quad (3.39)$$

The equations for the Nusselt number are valid for the same ranges of Re and Pr as for the single cell (compare Equations 3.35 and 3.36) [101]. The Nusselt number for a horizontal row of cells Nu_{row} is

calculated using the same equation as for a single cell (compare Equations 3.30-3.32), except for the use of $\text{Re}_{\psi_{\text{row}}}$ instead of Re .

When investigating a bunch of cells (as an extension to a horizontal row of cells), the equations adapt further. The voidage percentage ψ_{bunch} and respective Reynolds number $\text{Re}_{\psi_{\text{bunch}}}$ calculate [101]:

$$\psi_{\text{bunch}} = \begin{cases} \frac{\pi}{4a} & \text{for } b \geq 1 \\ \frac{\pi}{4ab} & \text{for } b < 1 \end{cases} \quad (3.40)$$

$$\text{Re}_{\psi_{\text{bunch}}} = \frac{v_{\text{air}}L}{\psi_{\text{bunch}}\nu_{\text{air}}} \quad (3.41)$$

Here, v_{air} is the air velocity in front of the bunch of cells.

The Nusselt number of a horizontal row of cells Nu_{row} is adapted further to Nu_{bunch} using the arrangement factor f_A .

$$\text{Nu}_{\text{bunch}} = f_A \text{Nu}_{\text{row}} \quad (3.42)$$

The arrangement factor f_A changes according to whether an aligned or staggered arrangement is investigated [101]:


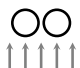

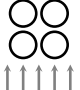
$$f_{A,\text{aligned}} = 1 + \frac{0.7}{\psi^{1.5}} \frac{(b/a - 0.3)}{(b/a + 0.7)^2} \quad (3.43)$$

$$f_{A,\text{staggered}} = 1 + \frac{2}{3b} \quad (3.44)$$

The vertical number of rows of cells N influences the Nusselt number Nu_{bunch} if $N < 10$ [101]:

$$\text{Nu}_{\text{bunch},N<10} = \frac{1 + (N - 1)}{N} f_A \text{Nu}_{\text{row}} \quad (3.45)$$

Table 3.4: Dimensionless thermal parameters for a single cylindrical cell and different battery module topologies, calculated for $v_{\text{air}} = 1 \text{ m s}^{-1}$ and $T = 25 \text{ }^\circ\text{C}$. N is the number of vertical cell rows. s_1 and s_2 are the spacings between horizontal and vertical cells respectively. a and b are the side and back spacing ratios of the arrangement. ψ is the voidage percentage and f_A is the arrangement factor of the bunch of cells. Re_ψ is the Reynolds number. Nu_{lam} , Nu_{turb} and Nu are the laminar, turbulent and mean Nusselt number respectively. For a bunch of cells, Nu is adjusted to Nu_{bunch} . From this value, the effective convective heat transfer coefficient h_{conv} is calculated.

Topology				
Parameter				
N	1	1	2	2
s_1 / cm		3.1	∞	3.1
s_2 / cm			3.1	3.1
a		1.2	∞	1.2
b			1.2	1.2
ψ	1	0.7	1	0.3
Re_ψ	2552.5	3875.0	2552.5	7479.3
Nu_{lam}	30.1	37.0	30.1	51.5
Nu_{turb}	18.1	25.0	18.1	41.7
Nu	35.4	45.0	35.4	66.5
f_A	1	1	0.6	1.9
Nu_{bunch}	35.4	45.0	27.8	94.8
$h_{\text{conv}} / \text{W m}^{-2} \text{K}^{-1}$	22.5	28.5	17.6	60.1

4

Parametric cell-to-cell variation and correlation

The aim of this chapter is to experimentally investigate the cell-to-cell variation of different parameters and the correlation between them. In order to allow for a valid statistic analysis, 1100 commercial 26650 LiFePO₄-graphite cells are examined, which originate from two batches. Like this, the influence of different batches on the parametric variation and correlation can additionally be investigated. Both, DC and AC measurements are conducted and the measurement conditions including the temperature as well as the relaxation times between the different characterisation measurements for each single cell are strictly monitored. Multiple cell parameters are determined: Different discharge capacities, different DC and AC impedances, the mass and the temperature of the cells. The determination of these different parameters allows for a comparison of their variations and to find correlations between the parameters. Thus, for example, the variation of discharge capacity can be compared to the variation of impedance of a cell, moreover these parameters can be correlated and the result can be discussed in context of the cell temperature. Furthermore, the measurement uncertainties for the parameters are determined and their influence on the variation results are discussed. In the end, distinct quantitative statements about the parametric variation of and the correlation between the investigated parameters are provided and are furthermore used to extract implications for the development and modelling of battery modules and for the quality control during cell production.

This chapter is based on the publication “Experimental investigation of parametric cell-to-cell variation and correlation based on 1100 commercial lithium-ion cells” by Rumpf et al. [38].

4.1 Experimental

In order to investigate the distribution of several cell parameters and the correlation between them, check-up (CU)- [28; 102] and electrochemical impedance spectroscopy (EIS)-measurements [28; 102; 103] have been performed under monitored temperature and relaxation conditions.

Table 4.1: Precision of the measurement equipment. During the CU-measurement the sampling rate was 0.1 Hz.

Instrument	Variable	Precision	Range
BasyTec CTS	Time	$\Delta t = \pm 1 \mu\text{s}$	
	Voltage	$\Delta V = \pm 0.3 \text{ mV}$	$V \in [0 \text{ V}, 6 \text{ V}]$
	Current	$\Delta I = \pm 200 \mu\text{A}$	$I \in]300 \text{ mA}, 5 \text{ A}]$
		$\Delta I = \pm 10 \mu\text{A}$	$I \in]15 \text{ mA}, 300 \text{ mA}]$
		$\Delta I = \pm 0.5 \mu\text{A}$	$I \in]1 \text{ mA}, 15 \text{ mA}]$
BioLogic VMP3	Phase angle	$\Delta \phi_Z = \pm 1^\circ$	$f \in [10 \times 10^{-6} \text{ Hz}, 1 \times 10^6 \text{ Hz}]$
	Impedance	$\Delta Z / Z = \pm 1 \%$	$f \in [10 \times 10^{-6} \text{ Hz}, 1 \times 10^6 \text{ Hz}]$
PT100	Temperature	$\Delta T(@25^\circ\text{C}) = \pm 0.2 \text{ K}$	$T \in [-70^\circ\text{C}, 250^\circ\text{C}]$
Sartorius Talent	Mass	$\Delta m = \pm 0.001 \text{ g}$	$m \in [0 \text{ g}, 310 \text{ g}]$

4.1.1 Measurement equipment

The check-up (CU)-measurements have been performed using a BaSyTec cell test system (CTS) and an Espec LU-123 climate chamber at $T = 25^\circ\text{C}$. The surface temperature of each cell has been monitored using PT100 thermocouples. For the electrochemical impedance spectroscopy (EIS)-measurements a BioLogic VMP3 potentiostat and a climate chamber at $T = 25^\circ\text{C}$ have been used. The weight measurements have been executed using a precision balance Sartorius Talent TE313S at room temperature. The precision of the measurement equipment is stated in Table 4.1.

During both, the CU- and the EIS-measurement, the cells have been contacted by custom-made terminal boards using gold plated spring contacts and enabling a four-wire-measurement.

4.1.2 Relaxation and thermal conditions

During the measurements special care has been taken of each individual cell concerning relaxation times between CU- and EIS-measurements and their storage temperature: From the time of arrival at the institute the cells had been stored at $T \approx 8^\circ\text{C}$. At least 3 h before the start of the CU-measurement, the respective cells have been stored at room temperature ($T \approx 25^\circ\text{C}$). 64 cells have been tested at a time. After the CU-measurement had been finished, the cells were stored at room temperature again for a minimum of $t = 40$ to 48 h. After this waiting-time between CU- and EIS-measurements, cell internal relaxation processes should have declined sufficiently [104]. Directly before the EIS-measurement was started, the cells have been stored at $T = 25^\circ\text{C}$ in a climate chamber for at least 3 h. An overview of the measurement and storage sequence illustrating the temperature condition and time duration for each step is presented in Figure 4.1.

4.1.3 CU-measurement

The cells have been shipped to the institute at a $SOC \approx 30\%$. First, each cell has been weighed as delivered (including its shrink sleeving). The CU-measurement first charged the respective cell using a CCCV protocol to 3.6 V using a CC $I_{\text{ch,CC}} = 1 \text{ C} = 3 \text{ A}$ followed by a constant-voltage (CV) (until $|I_{\text{ch,CV}}| < C/30 = 100 \text{ mA}$). This was followed by a 1 min 1 C discharge pulse and a 6 min open circuit (OC) period. Afterwards the cell has again been CCCV-charged. This charge period

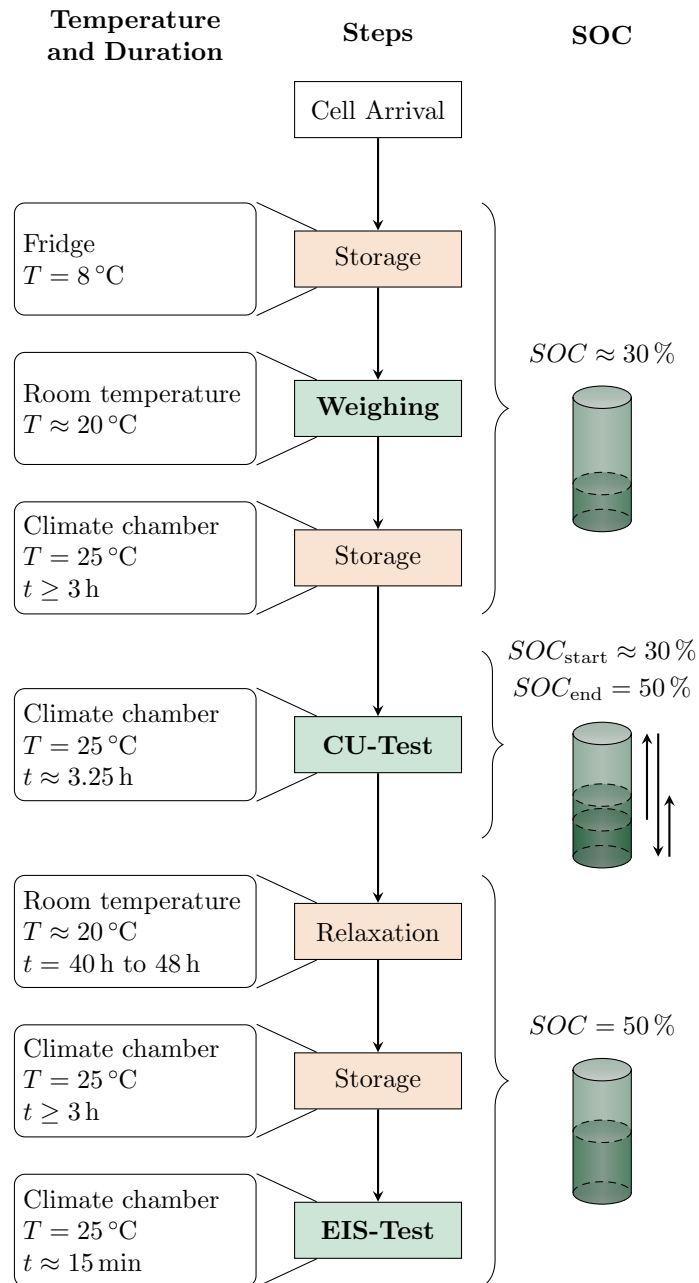


Figure 4.1: Flow chart of the measurement and storage sequence illustrating the temperature condition and time duration of each step.

has again been followed by a 6 min OC. Then, the cell has been CCCV-discharged to 2 V using a CC $I_{\text{disch,CC}} = 1 \text{ C} = 3 \text{ A}$ (CV until $|I_{\text{disch,CV}}| < C/20 = 150 \text{ mA}$). During these DCH periods (CC and CV) the discharge capacities of the cell $C_{\text{DCH_CC}}$, $C_{\text{DCH_CV}}$ and $C_{\text{DCH_CCCV}}$ are determined by Ah-counting. Having allowed for a short relaxation period of 6 min OC, the cell is finally CC charged to $SOC = 50\%$ using $I_{\text{ch,CC}} = 1 \text{ C} = 3 \text{ A}$, which corresponds to $0.5 C_{\text{DCH_CCCV}}$. The CU-plan is concluded by another 6 min relaxation period at OC. The relevant part of the test protocol, from which the parameters are defined, is displayed in Figure 4.2 top.

4.1.4 EIS-measurement

The EIS-measurement investigates the cell impedance within a logarithmic spaced frequency range $f \in [10000, 0.01] \text{ Hz}$ using an excitation current amplitude of $\hat{I} = 50 \text{ mA}$. The number of frequencies per decade (fpd) and number of measures per frequency (mpf) changes according to the chosen sub-intervals: $f \in [10000, 1] \text{ Hz}$ (13 fpd, 10 mpf), $f \in]1, 0.1] \text{ Hz}$ (10 fpd, 5 mpf), $f \in]0.1, 0.01] \text{ Hz}$ (3 fpd, 2 mpf). The test is performed at $SOC = 50\%$ and $T = 25 \text{ }^\circ\text{C}$. The data points at high frequencies representing an inductive behaviour are neglected during the analysis (compare Figure 4.2 bottom).

4.1.5 Possible sources of errors

There are different sources of error which could externally influence the variation of parameters and should therefore be kept in mind during the interpretation of results. Possible observations within the parametric variation over the cell number could be group building, drifts or trends.

The cells have been shipped in boxes of 25 cells. The boxes have been numbered according to their position in the delivered package and the cells have been numbered according to their position in the respective box. Thus, if the variation plot of a certain parameter shows groups of 25 cells within a certain parameter range, this could be due to the packaging order of the boxes.

The cells have been measured in sequential order. For the CU-measurement 64 cells have been measured at a time. For the EIS-measurement 8 cells have been measured at a time. The position of the cell regarding the terminal board, measurement channel, and position in the climate chamber could all result in a specific temperature influence which differs from the other cells. An increased cell temperature would for example result in an increased discharge capacity. Therefore, the parametric variation of the temperature over cell number should be analysed carefully regarding drifts or trends. The correlation coefficient of other parameters with the temperature can reveal possible dependencies.

Measurement uncertainties (MU) influencing the determined parameters will be discussed in Chapter 4.1.7.

4.1.6 Definition of parameters

In total, 68 parameters have been evaluated using both, CU- and EIS-measurements. In this thesis, the focus is on 15 of those parameters: Mass and mean temperature during measurement of the cell, three different discharge capacities, seven different impedances obtained from both, CU- and EIS-measurement and the interpolated frequencies of the EIS impedances. Figure 4.2 shows representative CU- and EIS-measurement data of one cell (top: last part of the CU-measurement, bottom: Nyquist

diagram of the EIS-measurement) and defines the obtained capacity and impedance parameters, which are discussed in this thesis.

Three values of discharge capacity are investigated. They are obtained from the last part of the CU-measurement starting at the begin of discharge: C_DCH_CC / Ah is the capacity obtained during the discharge CC-phase, C_DCH_CV / Ah is the capacity obtained during the discharge CV-phase and C_DCH_CCCV / Ah is the capacity obtained during both, the discharge CC- and CV-phase. A comparison of the three values will allow to analyse the influence of the variation of cell impedance on the variation of cell capacity.

Different values of impedance have been obtained from the two measurements: The DC impedances R_DC_10s , R_DC_30s and R_DC_60s are defined as the ratio between the difference in voltage and the difference in relaxation current at the end of the CU-measurement. The values are obtained after the final constant current charge phase. The time interval is 10 s, 30 s and 60 s respectively. After $t = 10s$ influences of the ohmic drop, charge transfer and diffusion processes contribute to the DC impedance, after $t = 30s$ and $t = 60s$ the influence of diffusion has become more dominant. Due to this fact, the SOC and temperature sensitivity of the DC impedance increases for R_DC_30s and R_DC_60s compared to R_DC_10s . Comparing the variation results of these three parameters, the change of DC impedance variation over time can be investigated. Comparing their correlation results, the changing temperature sensitivity can be depicted. Due to the definition of the DC impedances in the time domain, the term DC resistance can be considered more appropriate. However, the term DC impedance is still maintained in the following as like this the AC and DC impedances can be mentioned together in the text where appropriate.

The AC impedances are defined within the Nyquist diagram and are determined by interpolating the measured EIS-data to find the characteristic points R_AC_Im0 , R_AC_1000Hz , R_AC_max and R_AC_min . R_AC_Im0 is defined as the zero crossing of the data with the real axis: $R_AC_Im0 = Re(Z)|_{Im(Z)=0}$ at an interpolated frequency f_AC_Im0 . R_AC_1000Hz is defined as the real part of the impedance at an interpolated frequency $f = 1000 Hz$: $R_AC_1000Hz = Re(Z)|_{f=1000 Hz}$. R_AC_max is defined as the real part of the impedance between R_AC_Im0 and the local maximum at an interpolated frequency f_AC_max . R_AC_min is defined as the real part of the impedance between R_AC_Im0 and the local minimum at an interpolated frequency f_AC_min . The R_AC_max and R_AC_min impedances are chosen for investigation as they are frequently used for fitting purposes of ECMs. The R_AC_1000Hz impedance is analysed, as manufacturers often measure this impedance in order to determine the ohmic impedance of a cell. This is due to the fact that measurement devices can more easily detect the impedance at a constant frequency (i.e. $f = 1000 Hz$) than to find the true ohmic impedance R_AC_Im0 . The latter is more often considered in scientific publications. This work will allow for a comparison of both ohmic AC impedance values.

In addition to the capacity and impedance values, the mass and temperature of the cells are considered in the data analysis. T_Mean is the mean surface temperature of the cell during the CU-measurement. The variation of T_Mean is used to discuss the possible error sources of cell positioning within the climate chamber, the choice of measurement channel or terminal board during the CU-measurement. Correlation between T_Mean and another parameter is only to some extent sensible when the second parameter has not been determined from the CU-measurement.

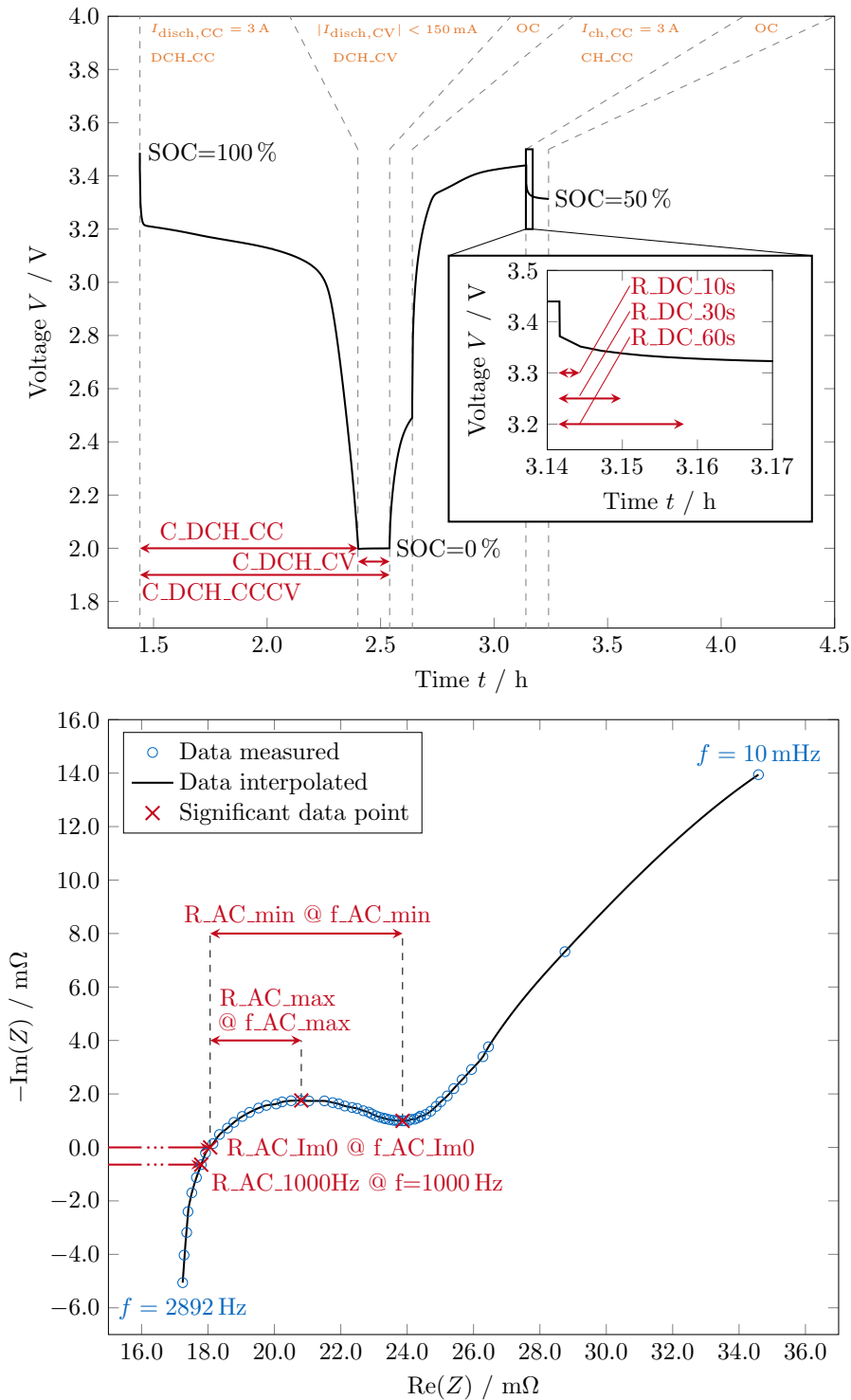


Figure 4.2: Definition of parameters from the last part of the CU-measurement (top) and Nyquist diagram of the EIS-measurement (bottom). Note, that the imaginary axis of the Nyquist diagram is displayed reversed. Thus, the so called local maximum impedance is in fact a minimum and vice versa. Additionally the mass and temperature of each cell is analysed.

4.1.7 Measurement uncertainties

In order to being able to discuss the statistic values of a parameter, these values must be related to the measurement uncertainty (MU) of the parameter. Only the mass and the temperature are determined directly. All other investigated parameters are calculated from measured basic quantities (i.e. time, current, voltage). In this case, the measurement uncertainty (MU) of a parameter x depends on the MU of the measured basic quantities. If a parameter x calculates from a product or quotient of these basic quantities $x = a \cdot b$, then the corresponding MU $u(x)$ calculates [105]:

$$u(x) = \sqrt{\left(\frac{\partial x}{\partial a}\right)^2 u^2(a) + \left(\frac{\partial x}{\partial b}\right)^2 u^2(b)} \quad (4.1)$$

where $\frac{\partial x}{\partial a}$ and $\frac{\partial x}{\partial b}$ are the partial derivatives of x with respect to a and b respectively and $u(a)$ and $u(b)$ are the MU of the basic quantities.

If a parameter x calculates from a sum or difference of these basic quantities $x = a + b$, then $u(x)$ calculates from the sum of the absolute errors in the quantities a and b :

$$u(x) = u(a) + u(b) \quad (4.2)$$

The MU of a basic quantity is determined based on the given MU range stated in the data sheet. If only the lower and upper limits of the MU of a directly measured quantity $u(a) \in [m, n]$ are given and if moreover no information is given about the distribution of the MU, then a uniform distribution is to be assumed between the limits [105]. In this case the variance of the corresponding MU $u^2(a)$ is given by [105; 106]:

$$u^2(a) = \frac{(n - m)^2}{12} \quad (4.3)$$

It is assumed, that the MU of a parameter x is the same for each single determination of the respective parameter for all cells. The MU is also the same when relating it to the mean or standard deviation of the parameter. The relations $u(x)/\mu_x$ and $u(x)/\sigma_x$ allow for a discussion of the influence of the MU on the parametric variation result. Both values are given in % and are stated in the results table (compare Table 4.2) for those parameters, for which the required MUs have been given in the data sheets. Note, that in order to not influence the determined parametric variation results, they are not corrected for the MU of the parameter. Instead, the respective MU values will be used to discuss the results.

4.2 Results and discussion

The obtained CU- and EIS data is evaluated and analysed in two steps: First, the distribution of the parameters is displayed and their variation is statistically analysed in Section 4.2.1. Second, the correlation between the investigated parameters is depicted and discussed in Section 4.2.2. The results of the parametric variations are summarized in Table 4.2, those of the parametric correlations are shown in Table 4.4.

4.2.1 Parametric variations of cell parameters

Regarding the parametric variation, each parameter is investigated based on its mean μ , standard deviation σ around the mean and its COV σ/μ . For each parameter a normal distribution is assumed. [9] The results of the parametric variations are displayed in different comparative figures (compare Figure 4.3 to 4.8) and are additionally summarized in Table 4.2.

All result figures showing the variation of a certain parameter based on one batch are structured as follows: The data is presented in two different graphs. The left graph shows the statistic variation of the parameter in a histogram plot, relating the number of cells to a certain parameter value. The right graph displays the respective parameter value over the sequential cell number (B1: 1-600, B2: 601-1100) in a scatter plot. In both graphs, the purple lines give the respective mean value μ , the green lines mark intervals, each with a width of the standard deviation σ of the displayed parameter. The values of mean μ , standard deviation σ around the mean and coefficient of variation σ/μ are given in the respective upper left corner of each graph. The black curve in the histogram plot depicts the normal distribution curve.

The respective histogram plot can be used to depict group building within the batches. Due to the sequentially cell numbering, the scatter plot can be used to reveal a possible drift within the measurement, dependency on cell positioning or dependency on the packaging boxes (groups of 25 cells per box).

In order to compare batches B1 and B2, the respective result plots of a certain parameter are displayed in the same row: At the left hand side of the figure the parametric variation of batch B1 is displayed in blue; the right hand side shows the corresponding parametric variation of batch B2 in orange.

4.2.1.1 Variation of discharge capacities

Figure 4.3 shows the parametric variations of the discharge capacities C_DCH_CC , C_DCH_CV and C_DCH_CCCV .

The discharge capacity obtained from the CC-phase C_DCH_CC shows similar absolute mean and standard deviation values for both batches B1 and B2. The respective relative variation is small: $\sigma/\mu|_{C_DCH_CC,B1} = 0.41\%$, $\sigma/\mu|_{C_DCH_CC,B2} = 0.48\%$. Neither group building nor any drift can be observed for C_DCH_CC .

The discharge capacity obtained from the CV-phase C_DCH_CV is slightly left skewed for both batches B1 and B2. The absolute mean and standard deviation values are similar for both batches. The respective relative variation is large: $\sigma/\mu|_{C_DCH_CV,B1} = 7.94\%$, $\sigma/\mu|_{C_DCH_CV,B2} = 8.65\%$. Neither group building nor any drift can be observed for C_DCH_CV .

The discharge capacity obtained from both discharge phases C_DCH_CCCV shows two peaks for both batches B1 and B2. The group building is also observed in the respective scatter plots. However, it cannot be attributed to the measure of 25 cells per box. The absolute mean and standard deviation values are again similar for both batches and the relative variation is small: $\sigma/\mu|_{C_DCH_CCCV,B1} = 0.23\%$, $\sigma/\mu|_{C_DCH_CCCV,B2} = 0.33\%$.

As the relative MU is very small for all capacities ($u(x)/\sigma_x < 2\%$, compare Table 4.2), the determined variation results are not affected by the MU of the capacity values.

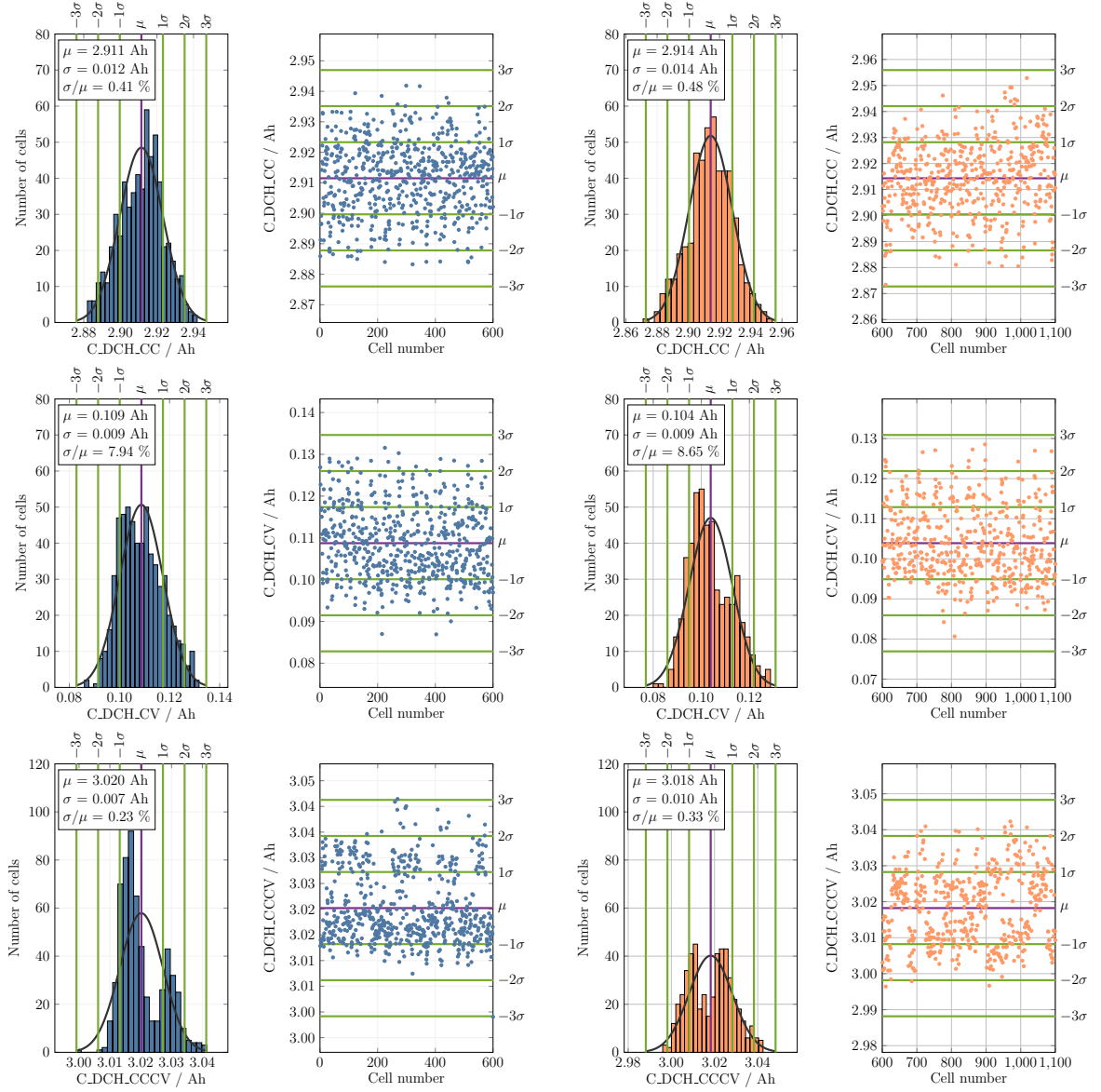


Figure 4.3: Variations of the discharge capacity during only CC-phase (first row), only CV-phase (second row) and combined CCCV-phase (third row). On the left side batch B1 is displayed in blue, on the right side batch B2 is displayed in orange.

The relative variation σ_x/μ_x of both, C_DCH_CC and C_DCH_CCCV, is smaller than 0.5%. However, the variation of C_DCH_CV is much higher around 8%. The reason for the relative variation of C_DCH_CV being so much bigger compared to C_DCH_CC, is assumed to be due to the fact that the CV-phase has both, a smaller duration and a smaller Ah-throughput than the CC-phase. In consequence, a small change in the duration of the CV-phase has a much higher influence on the result than the same change in duration on the result of the CC-phase. The same holds true for a change in the Ah-throughput. The reason for the relative variation of C_DCH_CCCV being the smallest value of all capacities, is the decreased influence of the variation of the cell impedance. This is due to C_DCH_CC and C_DCH_CV not being independent from each other: If the cell has a higher cell impedance, the arising overpotentials are higher, the voltage stop criterion is reached earlier; in consequence the CC-phase is shorter. Moreover, reducing higher overpotentials takes more time; therefore the CV-phase is longer compared to a cell with a smaller cell impedance. The CC-phase dominates the C_DCH_CCCV value due to its longer duration and higher Ah-throughput. Therefore, when summing up both capacities to C_DCH_CCCV, the influence of the variation of the cell impedance is decreased and furthermore, the relative variation of C_DCH_CCCV is even smaller than that of C_DCH_CC.

4.2.1.2 Variation of impedances

Figure 4.4 compares the three DC impedances R_DC_10s, R_DC_30s and R_DC_60s. The data of all DC impedances is normally distributed for both batches B1 and B2. The respective scatter plots neither show group building nor drift along the sequential cell number. The absolute mean impedance values and standard deviations of the two batches are similar, the relative variation of B1 is slightly higher compared to B2 for all three DC impedances. For R_DC_10s: $\sigma/\mu|_{R_DC_10s,B1} = 1.43\%$, $\sigma/\mu|_{R_DC_10s,B2} = 1.23\%$ (compare Figure 4.4 first row). For R_DC_30s: $\sigma/\mu|_{R_DC_30s,B1} = 1.34\%$, $\sigma/\mu|_{R_DC_30s,B2} = 1.22\%$ (compare Figure 4.4 second row). For R_DC_60s: $\sigma/\mu|_{R_DC_60s,B1} = 1.31\%$, $\sigma/\mu|_{R_DC_60s,B2} = 1.23\%$ (compare Figure 4.4 third row).

Thus, when determining the DC impedance after a longer period of time ($t = 30\text{ s}$, $t = 60\text{ s}$), the relative variation decreases insignificantly for batch B1, and it stays fairly constant for batch B2. The relative variation of a DC impedance is therefore not influenced significantly by the time period of its determination and it is moreover similar for the two examined batches.

The MUs of the DC impedances are in the range of 24 to 33% of the determined standard deviation (compare Table 4.2). Thus, about one quarter to one third of the determined variations could be due to the MUs.

Figure 4.5 compares the two ohmic AC impedances R_AC_Im0 and R_AC_1000Hz. When analysing the ohmic AC impedances R_AC_Im0 and R_AC_1000Hz, the first thing to notice is that batch B1 shows two peaks within its respective histogram distributions instead of only one. The data is normally distributed within the single separate peaks. However, regarding the complete data set of batch B1, the data is not normally distributed. For comparative reasons with the other parameters, a normal distribution is nevertheless used for statistic analysis. The group building within batch B1 can also be observed within the scatter plots. Batch B2 shows a normal distribution for both ohmic AC impedances.

The absolute values of the two parameters are again similar for both batches, however the standard deviation for batch B1 is much higher than for B2 due to the distribution shape. Therefore, the respec-

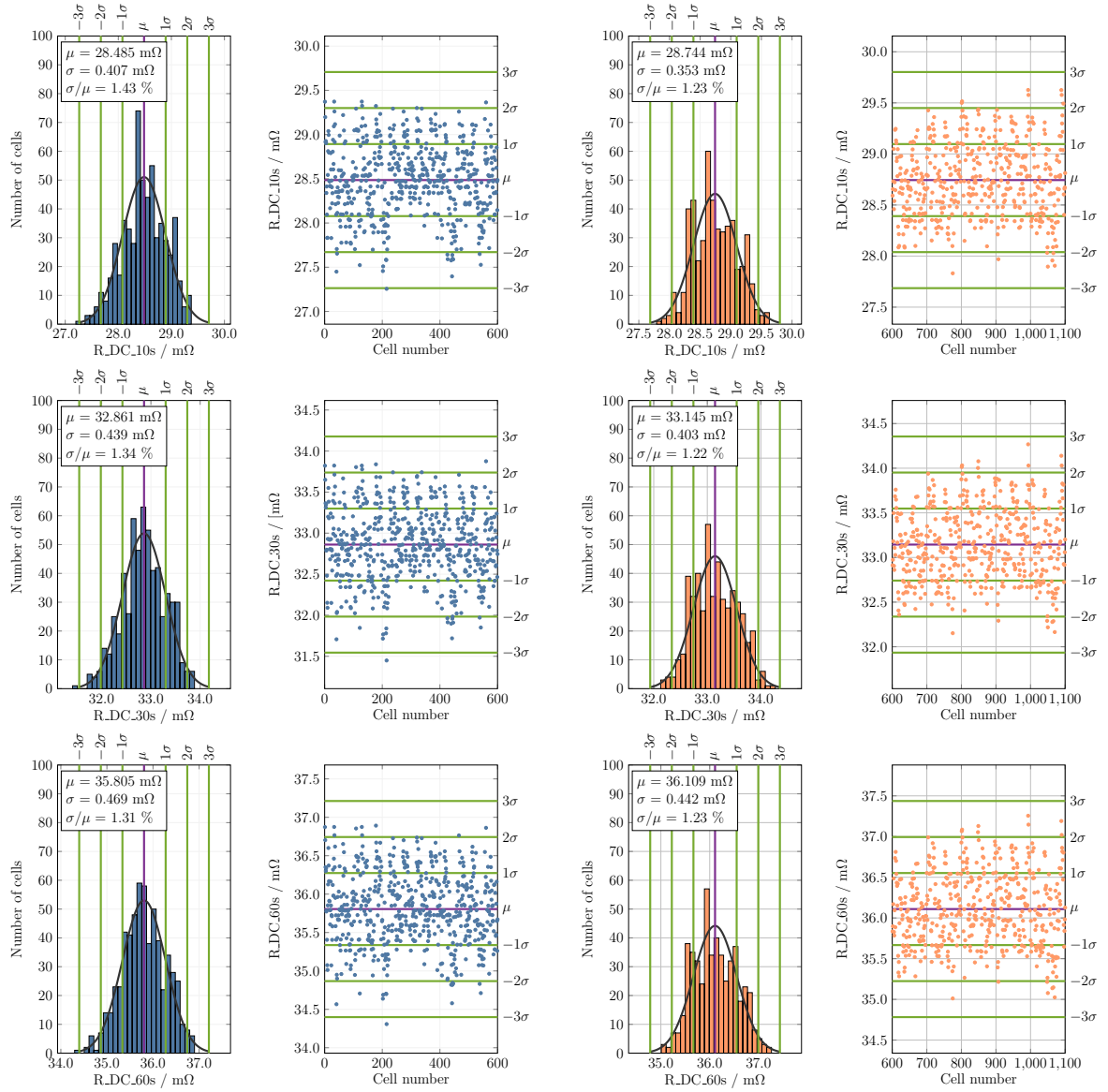


Figure 4.4: Variations of the DC impedances after 10s R_DC_10s (first row), 30s R_DC_30s (second row) and 60s R_DC_60s (third row). On the left side batch B1 is displayed in blue, on the right side batch B2 is displayed in orange.

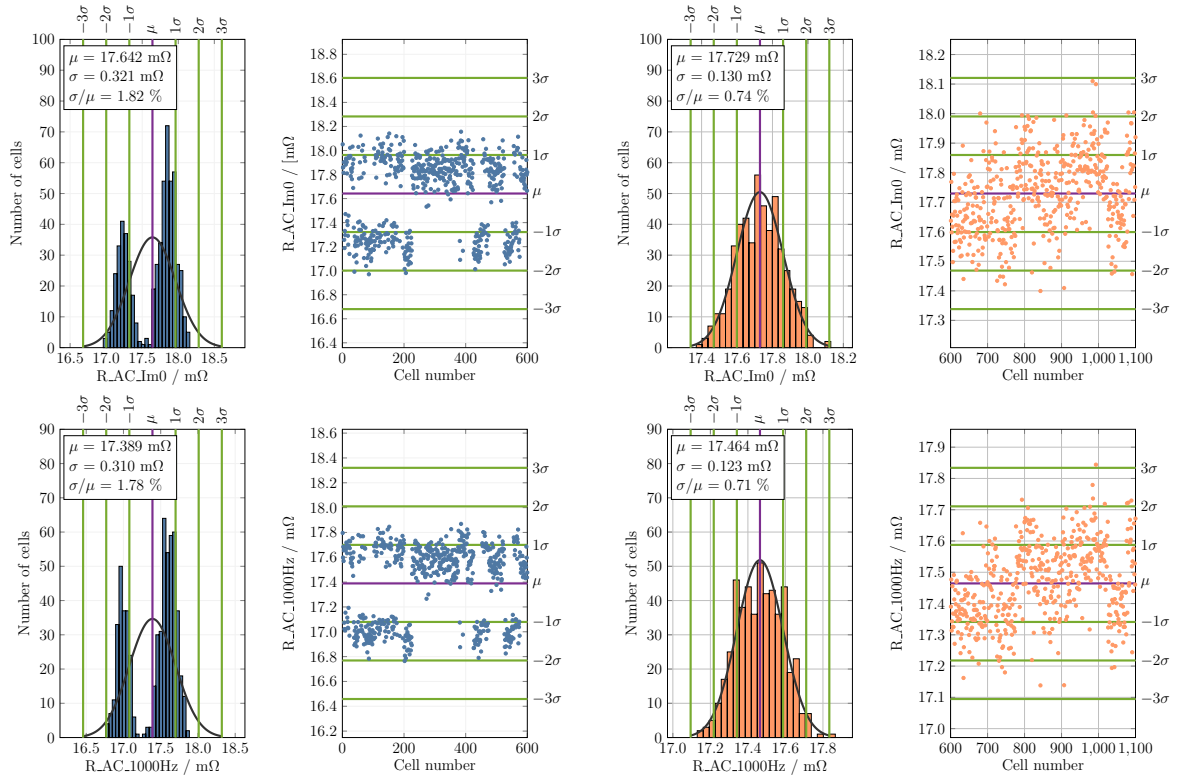


Figure 4.5: Variations of the ohmic AC impedances R_{AC_Im0} (first row) and R_{AC_1000Hz} (second row). On the left side batch B1 is displayed in blue, on the right side batch B2 is displayed in orange.

tive relative variations of B1 are higher than those of B2. For R_AC_Im0: $\sigma/\mu|_{R_AC_Im0,B1} = 1.82\%$, $\sigma/\mu|_{R_AC_Im0,B2} = 0.74\%$. For R_AC_1000Hz: $\sigma/\mu|_{R_AC_1000Hz,B1} = 1.78\%$, $\sigma/\mu|_{R_AC_1000Hz,B2} = 0.71\%$ (compare Figure 4.5 first and second row).

For batch B1, the relative MUs of the ohmic AC impedances are about one third of the respective standard deviation ($u(x)/\sigma_x \approx 33\%$). For batch B2, it is much higher at about $u(x)/\sigma_x \approx 80\%$ (compare Table 4.2). This is due to the fact, that the variation of B1 is much wider spread due to the observed group building such that the same MU has a larger influence on the less varying batch B2 than on B1.

An explanation for the observed two peaks within the histogram plots of the ohmic AC impedances of batch B1 could be a manufacturing adjustment during the production process. Such adjustments could be due to a change of material or due to a change in the process parameters. An example for a change of material could be a change of an electrode roll, a different current collector or a different electrolyte with a slightly different concentration. An example for a change in the process parameters could be a change in the welding parameters or tolerances concerning the tabs which connect jelly roll and cell can (i.e. length of the tabs, folding of the tabs during the insertion of the jelly roll into the can). As this clear group building within batch B1 cannot be observed for any other determined cell parameter but for the ohmic AC impedances, the latter reasons appear more realistic than a change in material. However, this is only an assumption as long as no additional information about the production process is provided by the manufacturer.

When comparing the two AC impedances within each single batch, the two AC impedances statistically show similar absolute and relative values. As there is no significant deviation between the two AC ohmic impedances, it is justifiable to use the R_AC_1000Hz impedance for experimental determination of the ohmic impedance of a cell. Within this work however, the ohmic impedance R_AC_Im0 will be used for further analysis.

Figure 4.6 compares the local extrema AC impedances R_AC_max and R_AC_min. They are both normally distributed for both batches. Neither group building nor drift can be observed within the scatter plots. The absolute mean values are slightly higher for batch B1, the absolute standard deviation values are similar for both batches regarding R_AC_max but higher for B2 regarding R_AC_min. Therefore, the relative variation values are higher for B2 for both parameters. For R_AC_max: $\sigma/\mu|_{R_AC_max,B1} = 7.94\%$, $\sigma/\mu|_{R_AC_max,B2} = 8.37\%$ (compare Figure 4.6 first row). For R_AC_min: $\sigma/\mu|_{R_AC_min,B1} = 2.60\%$, $\sigma/\mu|_{R_AC_min,B2} = 3.08\%$ (compare Figure 4.6 second row).

Comparing the mean relative MU of both batches: It is about $u(x)/\sigma_x \approx 54\%$ for R_AC_max and higher at about $u(x)/\sigma_x \approx 88\%$ for R_AC_min (compare Table 4.2). For the local maximum in the Nyquist plot, the variation could by 54% be due to the MU of the parameter, for the local minimum even by 88%.

The relative variation of R_AC_min is high around 2.8%, and even higher for R_AC_max around 8.2%. The reason for these high relative variation values could be the way of determining these AC parameters: The local maximum and minimum AC impedance values are determined by interpolating the real part values of the complex impedance from the Nyquist plot. As the complex impedance has been determined at logarithmic spaced frequencies, only a limited number of values serve as input for the interpolation, especially within the lower frequency ranges. An oscillation of the originally measured values might not completely be smoothed by the interpolation and could thus result in a large variation

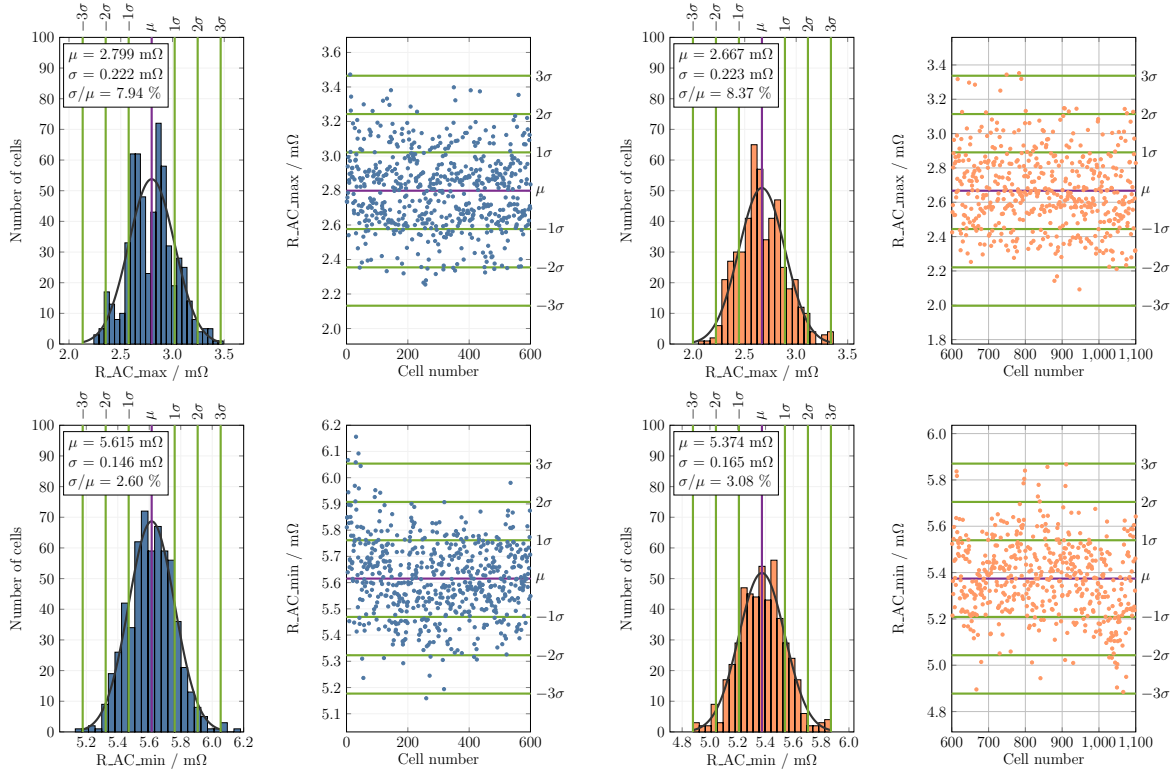


Figure 4.6: Variations of the local maximum AC impedance R_{AC_max} (first row), and the local minimum AC impedance R_{AC_min} (second row). On the left side batch B1 is displayed in blue, on the right side batch B2 is displayed in orange.

of the determined values. Moreover, the plateau, where the local maximum is determined is quite flat and the local minimum is quite smooth within the Nyquist plot (compare Figure 4.2 bottom). This could also explain the high relative variations for the parameters. In order to discuss the influence of the frequency values on the variation of the AC impedances, the variation of the AC frequencies will be analysed in Section 4.2.1.3.

Comparing the absolute values of R_{DC_10s} and R_{AC_Im0} it can be noted that the mean value of R_{DC_10s} is much higher than that of R_{AC_Im0} . This is due to the fact that within a time-dependent determination of DC impedances the ohmic drop occurs within the first instant after a current pulse has been cut off. At a time $t = 10s$ after the pulse not only the ohmic overpotential but also charge-transfer and diffusion overpotentials contribute to the measured impedance value. The ohmic DC impedance must therefore be considered part of the R_{DC_10s} value, which is why this value deviates significantly from the ohmic AC impedance absolute values. Calculating the ohmic DC time constant by using the measured f_{AC_Im0} mean value considering both batches ($\mu|_{f_{AC_Im0,B1,B2}} \approx 761$ Hz), this would imply to determine an ohmic DC impedance after $t \approx 1.3$ ms. In fact, the R_{DC_1ms} value had been determined from the CU-measurements. However, this value showed an unrealistic huge relative variations (not depicted in this thesis). This variation is attributed to the fact that 64 cells have been measured simultaneously by the CTS: a precise logging after such a small period of time seems to not have been possible for this number of cells. In other words, the large variation of R_{DC_1ms} is interpreted to be due to measurement uncertainties and has therefore not been depicted in this work. Determining the DC impedance value after $t = 1$ s (R_{DC_1s}) could possibly have resulted in a recordable value which might have been considered an approximate ohmic

DC impedance. However, based on the investigated data, in order to analyse the cell-to-cell variation of the cell impedance it is necessary to determine an ohmic AC impedance as the DC impedances do not provide information about obvious group building within a batch of cells.

The following discussed values refer to the combined mean values of both batches. The R_{DC_10s} absolute mean value is about $\mu|_{R_{DC_10s}} \approx 28.5 \text{ m}\Omega$, its corresponding frequency is $f|_{R_{DC_10s}} = 0.1 \text{ Hz}$. This mean DC impedance value is already bigger than the sum of $R_{AC_Im0} + R_{AC_min} \approx 17.7 \text{ m}\Omega + 5.5 \text{ m}\Omega = 23.2 \text{ m}\Omega$. Thus, the R_{DC_10s} impedance can be considered not only to include charge transfer processes but to additionally already include diffusion processes. The further DC impedances R_{DC_30s} and R_{DC_60s} even include more diffusion processes. The mean corresponding frequency to R_{AC_min} is $f_{AC_min} \approx 3.6 \text{ Hz}$. A DC impedance, which was comparable to $R_{AC_Im0} + R_{AC_min}$ would thus have to be measured after $t \approx 0.3 \text{ s}$.

4.2.1.3 Variation of AC frequencies

Figure 4.7 compares the interpolated AC frequencies f_{AC_Im0} , f_{AC_max} and f_{AC_min} . As defined in Section 4.1.6, the AC impedances are determined by interpolating the measured frequency values. This gives fixed frequency values for which the respective impedance is found. Figure 4.7 shows, how these frequencies vary for the two batches. f_{AC_Im0} does not show any drift or group building within the scatter plot. The relative variation of the parameter is in a similar range for the two batches, however, it is higher for batch B1: $\sigma/\mu|_{f_{AC_Im0,B1}} = 4.57\%$, $\sigma/\mu|_{f_{AC_Im0,B2}} = 3.79\%$ (compare Figure 4.7 first row). The local maximum and minimum values are found at fixed interpolated frequency values. Therefore, the variation of these frequencies is not scattered but lined at the respective fixed frequency values. As the interpolation point density was not very high around these local extrema, the frequency range is big, which leads to a high relative variation. For f_{AC_max} : $\sigma/\mu|_{f_{AC_max,B1}} = 15.42\%$, $\sigma/\mu|_{f_{AC_max,B2}} = 16.33\%$ (compare Figure 4.7 second row). For f_{AC_min} : $\sigma/\mu|_{f_{AC_min,B1}} = 20.75\%$, $\sigma/\mu|_{f_{AC_min,B2}} = 22.59\%$ (compare Figure 4.7 second row).

This large variation in frequencies of the local extrema explains the determined big variation in impedance values of the local extrema (compare Section 4.2.1.2). This implies, that the EIS-data is very sensitive to the chosen frequency density during an EIS-measurement. This especially applies to the low frequency range, within which the local maximum and minimum is determined. Choosing an increased number of low frequency points during an EIS-measurement means accepting a prolonged measurement time. However, it should be kept in mind that when aiming to fit an ECM by using these local maximum and minimum values, a preferably high accuracy of these characteristic data points is crucial for the quality of later modelling results. Another option would be to find the most suitable fixed frequencies for the characteristic data points - either by pre-measurements or by successive approximation. In any case, a good compromise should be found between measurement time and fitting accuracy.

4.2.1.4 Variation of mass and temperature

Figure 4.8 shows the parametric variations of the mass and mean temperature during the CU-measurement T_{Mean} .

The mass of the cells is normally distributed for both batches. The absolute mean and standard deviation values are similar for both batches and the relative variation is small: $\sigma/\mu|_{Mass,B1} = 0.07\%$,

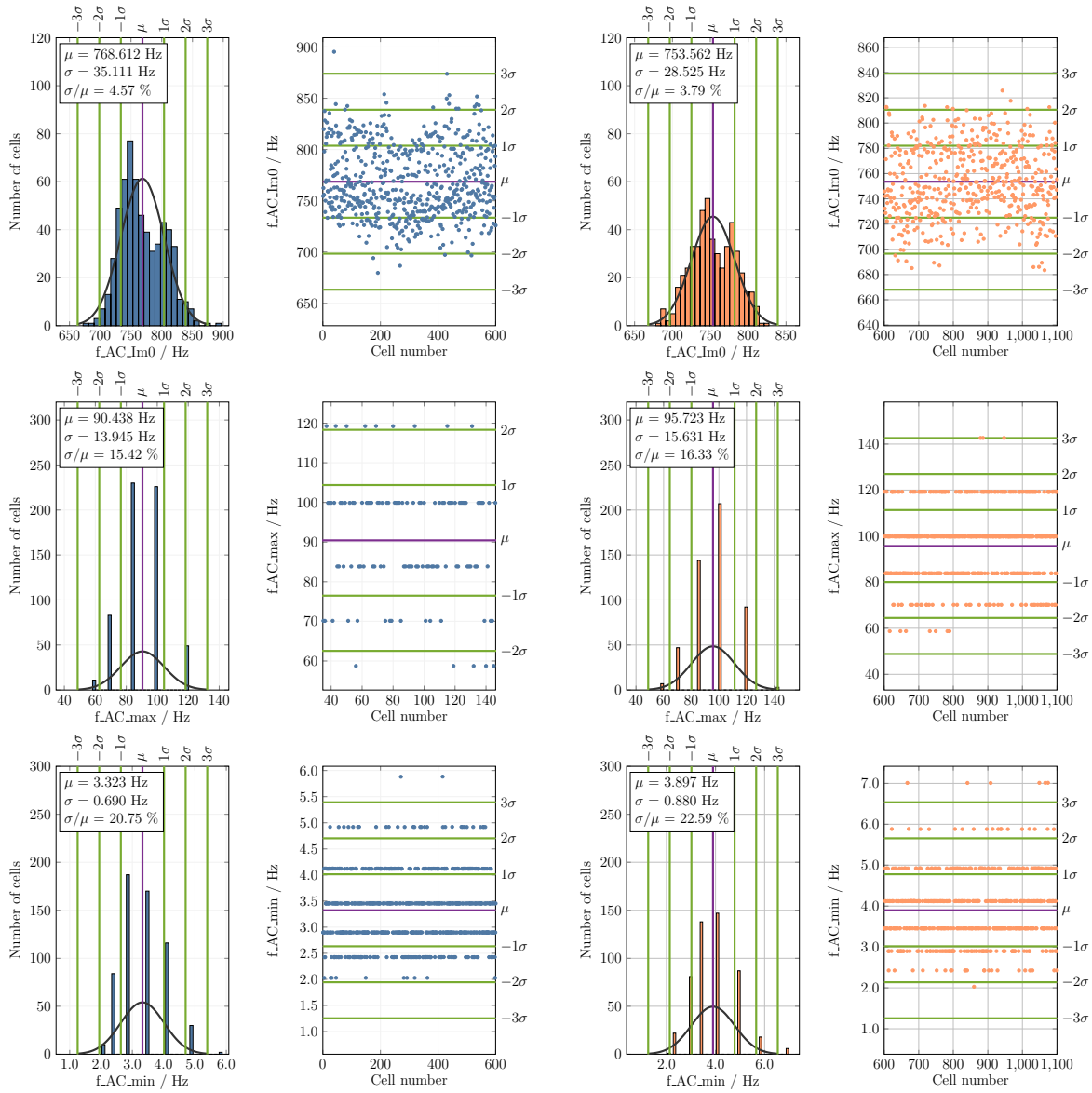


Figure 4.7: Variations of the interpolated AC frequencies f_{AC_Im0} (first row), f_{AC_max} (second row) and f_{AC_min} (third row). On the left side batch B1 is displayed in blue, on the right side batch B2 is displayed in orange.

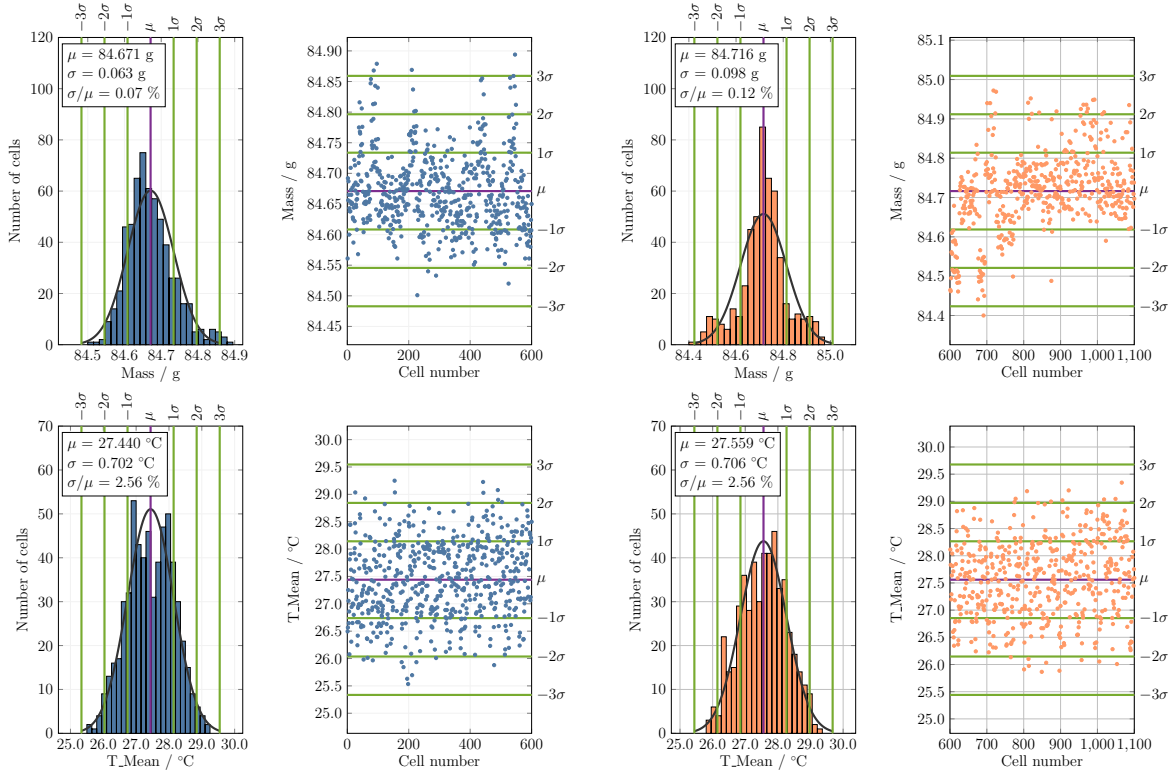


Figure 4.8: Variations of the mass (first row) and mean temperature during the CU-measurement T_Mean (second row). On the left side batch B1 is displayed in blue, on the right side batch B2 is displayed in orange.

$\sigma/\mu|_{Mass,B2} = 0.12\%$ (compare Figure 4.8 first row). Batch B2 shows a slight increase in mass with increasing cell number.

The corresponding relative MU is about $u(x)/\sigma_x < 1\%$ (compare Table 4.2). The MU has thus no impact on the variation result.

The mean temperature during the CU-measurement T_Mean is normally distributed for both batches. The absolute mean and standard deviation values are similar for both batches and the relative variation is equal: $\sigma/\mu|_{T_Mean,B1} = 2.56\%$, $\sigma/\mu|_{T_Mean,B2} = 2.56\%$ (compare Figure 4.8 second row).

For T_Mean the relative MU is about $u(x)/\sigma_x \approx 16\%$ (compare Table 4.2). This is not expected to significantly affect the variation results.

Moreover, no drift or group building can be observed within the scatter plots. This is a crucial finding as it implies three facts: First, the surrounding temperature within the climate chamber did not show a gradient, i.e. from bottom to top of the chamber, as no temperature drift within groups of 64 cells (maximum number of cells within the climate chamber) can be noticed. Second, the temperature was constant over the whole time of the CU-measurement, as no drift over the sequential cell number is apparent. Third, none of the terminal boards (4 cells per board) has been defective which could have led to an increased temperature of single cells in a regular cell number interval. Thus, the prior met assumptions regarding the temperature of the cells have been justified and errors within parametric variations due to the temperature can be excluded. It must be kept in mind though, that T_Mean is the mean temperature during the CU-measurement, which is why the significance of a correlation

between this temperature parameter and the parameters determined from the EIS-measurement is limited.

4.2.1.5 Comparison of parametric variations

Table 4.2 summarizes the parametric variations of the investigated parameters and states their relative MUs.

For the following comparisons of parametric variations, the mean of the respective values of batch B1 and B2 are considered, unless otherwise stated.

C_DCH_CC and C_DCH_CV both contribute to the overall discharge capacity C_DCH_CCCV. For C_DCH_CCCV the influence of the variation of the cell impedance is decreased. Therefore, its relative variation is the smallest $\sigma/\mu \approx 0.28\%$ compared to the other capacities. C_DCH_CC shows only a slightly higher value $\sigma/\mu \approx 0.45\%$. C_DCH_CV seems to be prone to technical measurement related variations. The relation to cell internal parametric variation remains to be investigated, e.g. by simulation.

Regarding the investigated cell impedances, determining the ohmic cell impedance proves to be necessary in order to determine a group building within a batch of cells, which has only been observed for the ohmic AC impedances. The DC impedances have not allowed for this classification. As the two ohmic AC impedances R_AC_Im0 and R_AC_1000Hz show the same statistical behaviour, it is justifiable to use R_AC_1000Hz to determine the ohmic cell impedance during cell characterisation. R_AC_1000Hz can also be determined at $f = 1000$ Hz by using an impedance meter or battery tester.

Without considering batch B1 (which shows group building), the DC impedances show a constant relative variation $\sigma/\mu \approx 1.22\%$ independent of the chosen time interval, whereas the ohmic AC impedances show a relative variation $\sigma/\mu \approx 0.72\%$, which is smaller by 40%. The local maximum and minimum impedances show a higher relative variation (about 7 times and 2.5 times higher respectively). These strong variations are interpreted to be due to the strong variation of their corresponding frequencies. When aiming to use the local maximum and minimum AC impedances for ECM fitting purposes and reliable modelling results, the density of frequency points during the EIS-measurement should be chosen carefully, especially when a flat local maximum plateau and smooth local minimum within the Nyquist diagram are observed.

Cell-to-cell variations of capacity and impedance reported in literature are within the same range as the results presented in this thesis (compare Table 4.3). Based on the determined results for batch B2, the ratio between the respective relative variations of C_DCH_CCCV and the ohmic impedance R_AC_Im0 equals $\sigma/\mu|_{C_DCH_CCCV} : \sigma/\mu|_{R_AC_Im0} \approx 1 : 2.2$. When considering C_DCH_CC, the ratio equals $\sigma/\mu|_{C_DCH_CC} : \sigma/\mu|_{R_AC_Im0} \approx 1 : 1.5$. These ratios are a little smaller than those reported in literature (compare Table 4.3). However, it becomes obvious that when aiming to relate and compare cell-to-cell variations, it is crucial to clearly identify the type and way of determination of the respective parameters. Otherwise the values are difficult to compare and interpret.

4.2.2 Parametric correlations between cell parameters

In order to investigate the dependency between two determined cell parameters, their respective correlation graph is analysed. The x- and y-coordinates of each correlation graph are defined by the range

Table 4.2: Experimentally determined parametric variations of the two batches. The variation is given in terms of mean value μ , standard deviation σ around the mean and coefficient of variation (COV) σ/μ . The measurement uncertainty (MU) of the parameter u is related to both, μ and σ of the parameter. The definition of the examined parameters is shown in Figure 4.2. Batch B1 is displayed in blue, B2 is displayed in orange. If no value is given, information to calculate the value have been missing.

Parameter x	Batch	μ_x	σ_x	σ_x/μ_x	$u(x)/\mu_x$	$u(x)/\sigma_x$
Mass and Temperature						
Mass / g	B1	84.671	0.063	0.07 %	<0.01 %	0.92 %
	B2	84.716	0.098	0.12 %	<0.01 %	0.59 %
T_Mean / °C	B1	27.440	0.702	2.56 %	0.42 %	16.45 %
	B2	27.559	0.706	2.56 %	0.42 %	16.36 %
Discharge capacity						
C_DCH_CC / Ah	B1	2.911	0.012	0.41 %	<0.01 %	0.93 %
	B2	2.914	0.014	0.48 %	<0.01 %	0.80 %
C_DCH_CV / Ah	B1	0.109	0.009	7.94 %	0.01 %	0.14 %
	B2	0.104	0.009	8.65 %	<0.01 %	0.10 %
C_DCH_CCCV / Ah	B1	3.020	0.007	0.23 %	<0.01 %	1.78 %
	B2	3.018	0.010	0.33 %	<0.01 %	1.12 %
DC Impedances (CU)						
R_DC_10s / mΩ	B1	28.485	0.407	1.43 %	0.40 %	28.34 %
	B2	28.744	0.352	1.23 %	0.40 %	32.77 %
R_DC_30s / mΩ	B1	32.861	0.438	1.33 %	0.35 %	26.33 %
	B2	33.145	0.403	1.22 %	0.35 %	28.62 %
R_DC_60s / mΩ	B1	35.805	0.469	1.31 %	0.32 %	24.59 %
	B2	36.109	0.442	1.22 %	0.32 %	26.10 %
AC Impedances (EIS)						
R_AC_Im0 / mΩ	B1	17.642	0.320	1.82 %	0.58 %	32.55 %
	B2	17.729	0.130	0.73 %	0.57 %	78.26 %
R_AC_1000Hz / mΩ	B1	17.389	0.310	1.78 %	0.59 %	33.21 %
	B2	17.464	0.123	0.70 %	0.58 %	81.86 %
R_AC_max / mΩ	B1	2.799	0.222	7.93 %	4.39 %	55.36 %
	B2	2.667	0.223	8.36 %	4.39 %	52.51 %
R_AC_min / mΩ	B1	5.615	0.146	2.60 %	2.46 %	94.61 %
	B2	5.374	0.165	3.08 %	2.50 %	81.26 %
Frequencies						
f_AC_Im0 / Hz	B1	768.612	35.082	4.56 %	-	-
	B2	753.562	28.496	3.78 %	-	-
f_AC_max / Hz	B1	90.438	13.934	15.41 %	-	-
	B2	95.723	15.616	16.31 %	-	-
f_AC_min / Hz	B1	3.323	0.689	20.73 %	-	-
	B2	3.897	0.879	22.56 %	-	-

Table 4.3: Overview of experimental investigations on cell-to-cell variations of capacity and impedance of production fresh cells reported in literature compared to this work: Besides basic cell parameters, the resulting relative variations of capacity and impedance as well as the ratio between the two values are listed.

Reference	Dubarry [18]	Campestrini [20]	Schuster [19]	Paul [9]	This work
No. of new cells	10	250	484	20000	1100 (B2: 500)
Chemistry	-	NCA	NMC	LFP	LFP
Nom. capacity	1.9 Ah	2.8 Ah	1.95 Ah	4.4 Ah	3 Ah
Cell ID	<i>commercial</i> 18650	Panasonic NCR18650PD	Molicel IHR18650A	-	Sony US26650FTC1
$\sigma/\mu _{\text{capacity}}$	C_DCH_CCCV: 0.16 %	C_DCH_CCCV: 0.16 %	C_DCH_CCCV: 0.8 %	C_DCH: 1.3 %	C_DCH_CCCV (B2): 0.33 %
$\sigma/\mu _{\text{impedance}}$	R_DC: 5.66 %	R_AC_1000Hz: 0.72 %	R_AC_Im0: 1.94 %	R_DC: 5.8 %	R_AC_Im0 (B2): 0.73 %
$\frac{\sigma/\mu _{\text{capacity}}}{\sigma/\mu _{\text{impedance}}}$	1:35.4	1:4.5	1:2.4	1:4.5	1:2.2

of parametric variation of the two respective parameters. Illustrating the values for all cells of a batch within the correlation graph will form a scatter plot. A totally positive ($\rho_{xy} = 1$) (negative ($\rho_{xy} = -1$)) correlation of the two parameters will be shown by a straight line with a positive (negative) gradient. A totally missing correlation ($\rho_{xy} = 0$) is depicted by a non-biased scatter plot. In the lower right corner of each correlation graph, the correlation coefficient ρ (compare Section 3.3.2) is given.

For being able to compare the correlation between different parameters, the single correlation graphs are arranged in a graphical correlation matrix: As the correlation coefficient between one parameter and itself always equals $\rho_{xx} = 1$ and the plot is therefore not of interest (straight line), the diagonal cells of the graphical correlation matrix are used to state the name and unit of the respective parameter. The matrix graph is divided into two triangular matrices by this diagonal line. The lower triangular matrix represents the parametric correlation data of batch B1 (blue), the upper triangular matrix that of batch B2 (orange). Each graphical matrix cell displays the single correlation graph of those two parameters which are given in the respective row and column. The given parametric ranges relate to all correlation graphs within the respective row or column.

Figure 4.9 shows the correlation between different impedances. Figure 4.10 shows the correlation between selected impedances, discharge capacities, mass and temperature.

Table 4.4 summarizes the obtained correlation coefficients for all 15 parameters. The structure of the table is based on the structure of the graphical correlation matrices within the correlation figures.

4.2.2.1 Correlation between impedances

The three determined DC impedances R_DC_10s, R_DC_30s and R_DC_60s show a strong correlation between each other: $\rho_{xy} \in [0.984, 0.996]$ for both batches (compare Table 4.4). Therefore, only R_DC_10s will be used for the following graphical analysis of the parametric correlations.

Figure 4.9 shows the correlation between the following impedance values: R_DC_10s, R_AC_Im0, R_AC_1000Hz, R_AC_min and R_AC_max.

R_AC_Im0 and R_AC_1000Hz show a strong correlation for both batches ($\rho_{xy,B1} = 0.988$, $\rho_{xy,B2} = 0.942$). This is a crucial finding as it justifies the assumption that measuring the R_AC_1000Hz impedance during cell characterization does adequately represent the ohmic impedance of the cell.

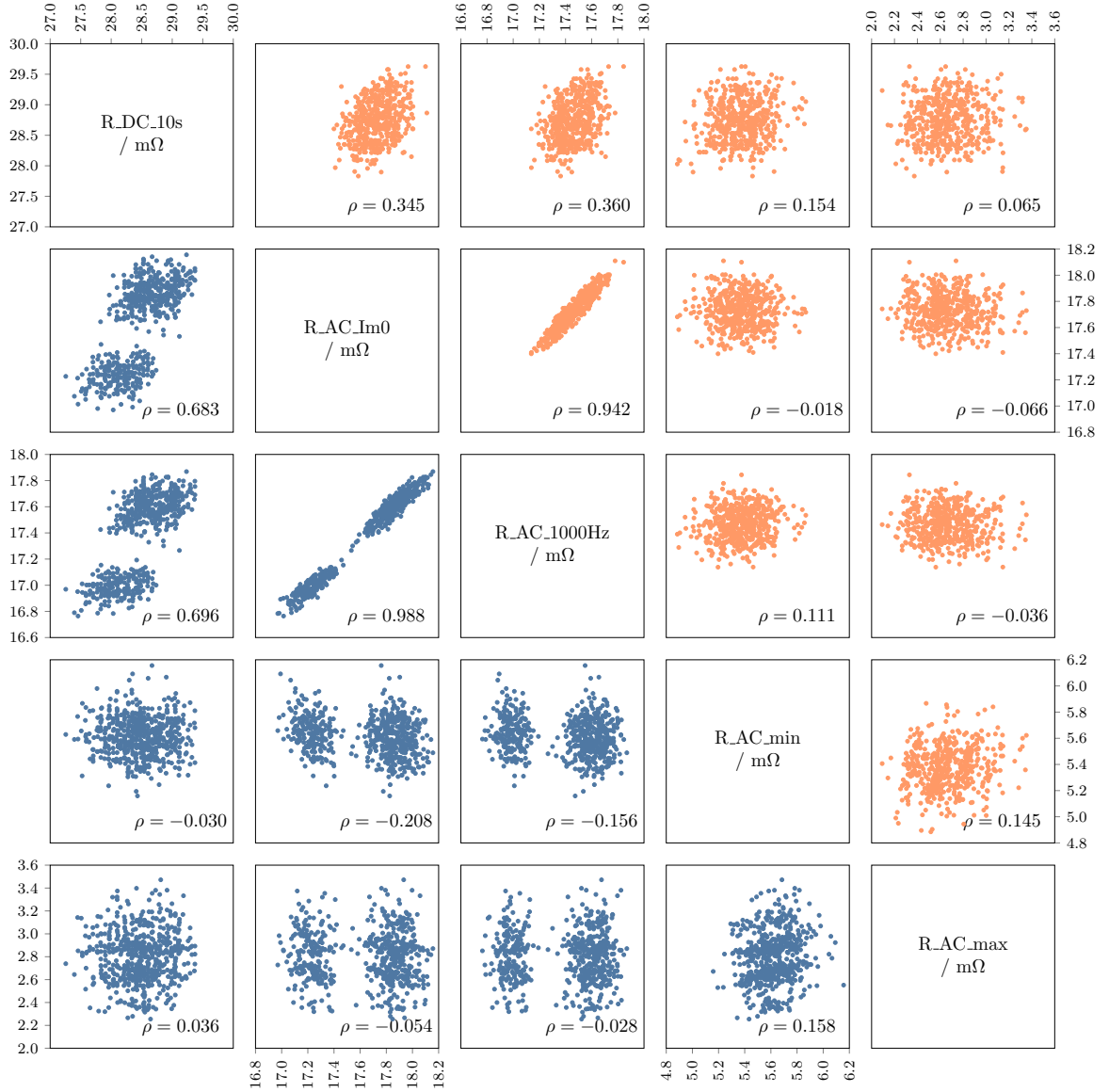


Figure 4.9: Correlations between the following cell parameters: R_DC_10s, R_AC_Im0, R_AC_1000Hz, R_AC_min and R_AC_max. The blue points represent batch B1, the orange points batch B2. The correlation coefficient values range from $\rho \in [-1, 1]$ and are given in the lower right corner of each correlation plot. Their corresponding correlation classes are defined in Section 3.3.2.

For batch B1 two separate scatter plots can be observed within those correlation graphs, which are dependent on one of the ohmic AC impedances R_AC_Im0 or R_AC_1000Hz. This data separation within the scatter plot implies a group building within batch B1. The remaining correlation graphs of B1 do not show this group building. The impedances R_DC_10s, R_AC_min and R_AC_max do not represent pure ohmic impedances of the cell but are associated with charge transfer and diffusion processes. The partially observed group building seems to relate to a change in the pure ohmic impedance during the production process of batch B1. Thus, batch B2 seems more suitable for further discussions of the correlation between parameters.

Regarding batch B1, R_DC_10s shows a moderate but nearly strong correlation with both, R_AC_Im0 ($\rho_{xy,B1} = 0.683$) and R_AC_1000Hz ($\rho_{xy,B1} = 0.696$). However, for B2 these correlations are only moderate and rather weak for both, R_AC_Im0 ($\rho_{xy,B2} = 0.345$) and R_AC_1000Hz ($\rho_{xy,B2} = 0.360$). This moderate correlation between the R_DC_10s and the ohmic AC impedances occurs due to the fact that the pure ohmic impedance of the cell contributes to the investigated DC impedance. However, the change within the correlation classes when comparing batch B1 and B2, implies that the moderate but nearly strong correlation observed for B1 results from the group building within that batch.

Within all other correlation graphs the correlation is weak ($|\rho_{xy}| < 0.3$). In detail, this implies that the parameters R_AC_min and R_AC_max are neither dependent on each other nor dependent on R_DC_10s, R_AC_Im0 or R_AC_1000Hz for neither batch B1 nor B2.

Therefore, only the R_DC_10s and R_AC_Im0 impedance will be used for the following investigation of correlation between impedances, discharge capacities, mass and temperature of the cells.

4.2.2.2 Correlation between mass, temperature, discharge capacities and specific impedances

Figure 4.10 shows the correlation between the impedances R_DC_10s and R_AC_Im0, the discharge capacities C_DCH_CC, C_DCH_CV and C_DCH_CCCV, the mass and the mean temperature during CU-measurement T_Mean.

The discharge capacities show differently strong correlations between each other: The correlation between C_DCH_CV and C_DCH_CCCV is weak. The correlation between C_DCH_CC and C_DCH_CV is moderate strong to strong and negative ($\rho_{xy,B1} = -0.809$, $\rho_{xy,B2} = -0.692$), whereas the correlation between C_DCH_CC and C_DCH_CCCV is moderate strong and positive ($\rho_{xy,B1} = 0.690$, $\rho_{xy,B2} = 0.762$). This finding indicates that when a cell has been charged more (compared to the other cells) during the CC-phase, it is charged less (compared to the other cells) during the CV-phase and vice versa.

The correlation between the DC impedance R_DC_10s and the single phase discharge capacities is moderate strong to strong and negative for C_DCH_CC ($\rho_{xy,B1} = -0.723$, $\rho_{xy,B2} = -0.626$) and positive for C_DCH_CV ($\rho_{xy,B1} = 0.637$, $\rho_{xy,B2} = 0.817$). This means, that a high CC discharge capacity correlates to a small DC impedance, whereas a high CV discharge capacity correlates to a high DC impedance. These results support the explanations met in Section 4.2.1: A higher cell impedance leads to higher overpotentials during the CC-phase which then take longer to be reduced during the CV-phase. For C_DCH_CCCV the influence of variation of the cell impedance is decreased by summing up C_DCH_CC and C_DCH_CV resulting in a weak to moderate weak and negative

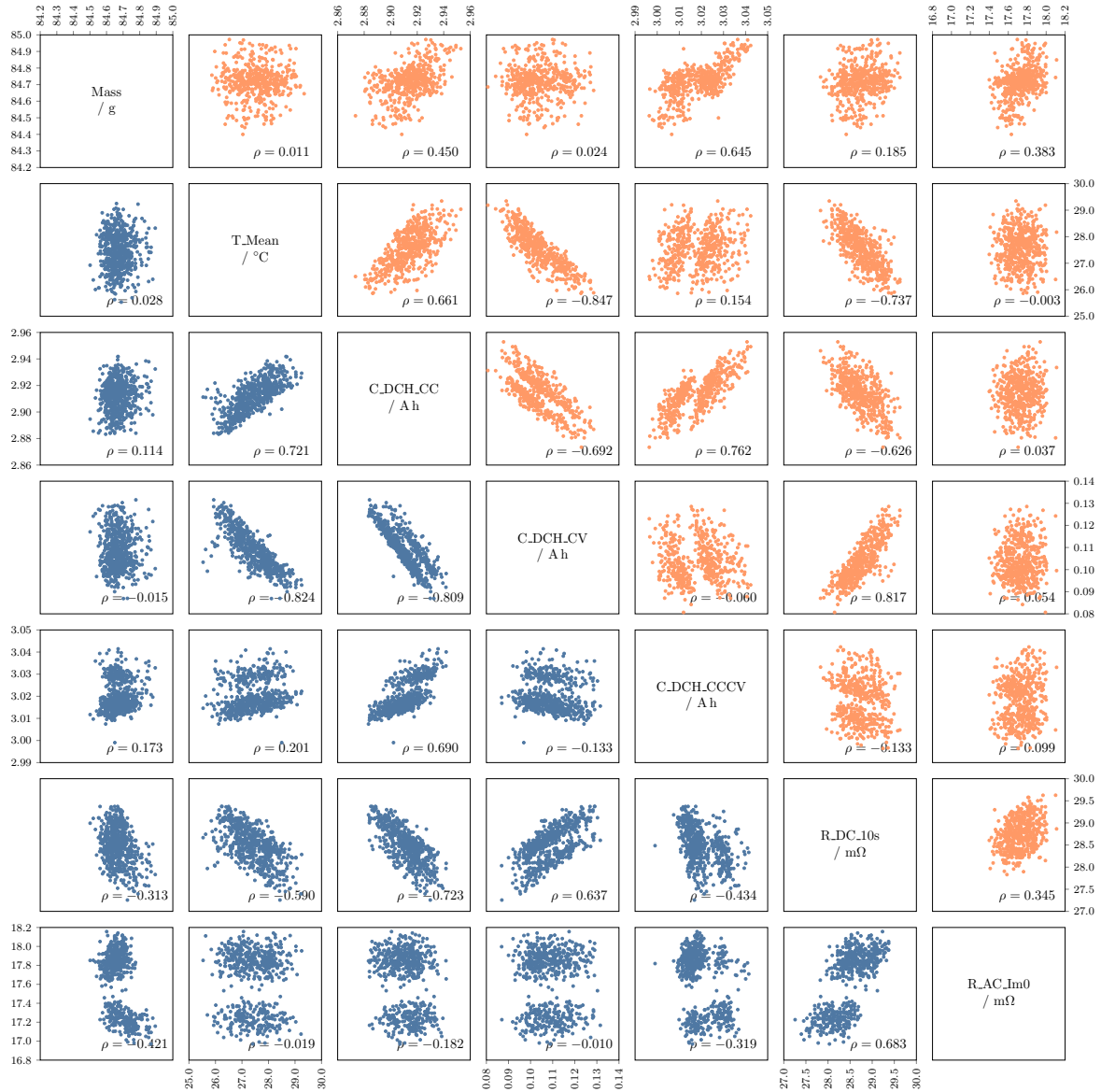


Figure 4.10: Correlations between the following cell parameters: Mass, T_Mean, C_DCH_CC, C_DCH_CV, C_DCH_CCCV, R_DC_10s and R_AC_Im0. The blue points represent batch B1, the orange points batch B2. The correlation coefficient values range from $\rho \in [-1, 1]$ and are given in the lower right corner of each correlation plot. Their corresponding correlation classes are defined in Section 3.3.2. Note that T_Mean is the mean temperature during the CU-measurement. A correlation of T_Mean with AC values is therefore not significant.

correlation between C_DCH_CCCV and R_DC_10s. Thus, the variation of R_DC_10s allows no conclusion about the variation of C_DCH_CCCV.

The correlation between the ohmic AC impedance R_AC_Im0 and the discharge capacities is weak. This is due to the fact that during the discharge of a cell mainly those overpotentials are relevant, which are due to processes occurring at low frequencies. In order to make statements about the variation of both, the cell impedance and the cell capacity, both parameters need to be investigated.

The temperature T_Mean shows the same correlation behaviour for both batches: Between T_Mean and C_DCH_CC a moderate strong to strong positive correlation ($\rho_{xy,B1} = 0.721$, $\rho_{xy,B2} = 0.661$) is observed. Between T_Mean and C_DCH_CV a strong negative correlation ($\rho_{xy,B1} = -0.824$, $\rho_{xy,B2} = -0.847$) can be seen. Between T_Mean and R_DC_10s a moderate strong to strong negative correlation ($\rho_{xy,B1} = -0.590$, $\rho_{xy,B2} = -0.737$) is observed. A high impedance value leads to a shorter CC-phase which again leads to a smaller mean temperature value during the whole CU-measurement. The strong temperature dependency observed for the single phase discharge capacities is compensated when combining both capacities to C_DCH_CCCV ($\rho_{xy,B1} = 0.201$, $\rho_{xy,B2} = 0.154$). Therefore, using this discharge capacity during cell characterisation is beneficial, as the temperature dependency resulting from the correlation with the cell impedance is reduced. The significance of any correlation between T_Mean and the ohmic AC impedance R_AC_Im0 is limited as T_Mean is the mean temperature determined from the CU-measurement and not from the EIS-measurement.

The mass does not show any correlation with the other investigated parameters, except for a moderate correlation with C_DCH_CCCV and only for B2 ($\rho_{xy,B2} = 0.645$). Such a correlation could be explained by a variation in cell internal parameters such as the volume fraction of active material. Unless corresponding information by the manufacturer can be accessed, this dependency between internal and external cell parameters can be investigated by physicochemical simulation.

Table 4.4 shows the obtained correlation coefficients for all 15 parameters. Analysing the dependency of the local maximum and minimum AC impedance on their corresponding frequency reveals that their respective correlation is very strong and negative: The correlation between R_AC_max and f_AC_max: $\rho_{xy,B1} = -0.943$, $\rho_{xy,B2} = -0.940$. The correlation between R_AC_min and f_AC_min: $\rho_{xy,B1} = -0.758$, $\rho_{xy,B2} = -0.767$. This finding confirms the assumption that it is crucial to carefully choose the frequencies and density of frequency points during an EIS-measurement in order to allow for accurate ECM fitting results.

4.3 Implications for developing and modelling battery modules

From the results, four major implications for the development and modelling of battery modules can be extracted. They are numbered according to the boxes which group the data in Table 4.4.

- A For modelling purposes, each of the DC impedances can be used, as R_DC_10s, R_DC_30s and R_DC_60s all show the same statistical behaviour. Their correlation is very strong. Therefore, two of the three DC impedances can be omitted during characterisation. However, the DC impedances fail to depict the group building which is observed for the ohmic AC impedances within a batch.
- B To make a statement about the variation of the cell impedance, it is therefore necessary to determine the ohmic cell impedance. As the ohmic AC impedances R_AC_Im0 and

Table 4.4: Experimentally determined parametric correlation coefficients between all 15 parameters: The lower triangular matrix gives the correlation coefficients of batch B1 in blue, the upper triangular matrix gives the correlation coefficients of batch B2 in orange. The definition of the given parameters is shown in Figure 4.2. The correlation coefficient values range from $\rho \in [-1, 1]$. Their corresponding correlation classes are defined in Section 3.3.2. The boxes A, B, C, and D group the data from which four major implications are extracted for the development and modelling of battery modules (compare Section 4.3).

Mass	0.011	0.450	0.024	0.645	0.185	0.180	0.182	0.383	0.400	-0.024	-0.014	0.007	-0.004	-0.004
0.028	T_Mean	0.661	-0.847	0.154	-0.737	-0.762	-0.772	-0.003	-0.017	-0.102	-0.031	-0.055	-0.102	0.017
0.114	C_DCH	CC	-0.692	0.762	-0.626	-0.643	-0.649	0.037	0.045	-0.143	-0.052	-0.047	-0.025	-0.021
-0.015	C_DCH	CV	-0.060	0.817	0.848	0.860	0.860	0.054	0.030	0.013	0.015	-0.088	-0.027	-0.019
0.173	0.201	0.690	-0.133	C_DCH	-0.133	-0.128	-0.126	0.099	0.089	-0.187	-0.059	-0.144	-0.058	-0.046
-0.313	-0.590	-0.723	0.637	-0.434	CCGV	0.992	0.990	0.345	0.360	0.154	0.065	0.051	-0.007	-0.063
-0.277	-0.641	-0.758	0.698	-0.421	DC	10s	60s	0.325	0.337	0.150	0.067	0.042	-0.013	-0.063
-0.254	-0.669	-0.779	0.730	-0.415	0.984	0.995	DC	0.314	0.324	0.146	0.068	0.034	-0.016	-0.062
-0.421	-0.019	-0.182	-0.010	-0.319	0.683	0.623	0.584	AC	Im0	-0.018	-0.066	-0.234	0.032	-0.084
-0.415	-0.034	-0.192	-0.009	-0.335	0.696	0.637	0.598	AC	Im0	0.111	-0.036	0.057	0.081	-0.096
0.033	-0.074	-0.114	0.048	-0.134	0.036	0.044	0.048	AC	Im0	max	min	0.145	0.143	-0.940
0.048	-0.102	-0.151	0.023	-0.227	-0.030	-0.012	-0.006	0.158	AC	max	min	0.466	0.067	-0.767
0.163	-0.099	-0.040	-0.008	-0.077	-0.123	-0.106	-0.098	0.445	Im0	max	min	f_AC	Im0	0.127
0.017	0.035	0.043	-0.047	0.016	-0.057	-0.058	-0.058	-0.943	0.046	0.058	f_AC	max	min	-0.003
0.012	0.002	0.004	0.031	0.044	0.022	0.017	0.018	0.043	-0.758	-0.108	-0.076	f_AC	min	-0.026

R_AC_1000Hz both show the same statistical behaviour, also a faster measurement technique using an impedance meter or battery tester, which determines the ohmic impedance at a constant frequency $f = 1000$ Hz, can be considered. In this case, an EIS-measurement is not necessarily required and the four AC impedances could be omitted during cell characterisation.

- C To make a statement about the variation of the cell capacity, C_DCH_CCCV should be determined, as this is the capacity for which the influence of the variation of both, the cell impedance and the temperature is decreased. As this capacity calculates from the two other capacities C_DCH_CC and C_DCH_CV, none of the determined capacities can be omitted during characterisation. Nevertheless, the measurement time does not increase. Note, that the variation of the cell impedance allows no conclusion about the variation of the cell capacity.
- D When aiming to use characteristic points within the Nyquist plot (i.e. the local maximum or minimum) determined from an EIS-measurement for ECM fitting purposes, the frequencies should be chosen carefully. R_AC_max and R_AC_min have been found to strongly depend on their respective frequencies f_AC_max and f_AC_min. Especially if the local maximum plateau within the Nyquist diagram is flat and the local minimum is smooth, the impedances should be determined at either fixed frequencies or the interpolated frequencies should be based on a high frequency density within that characteristic range. A pre-measurement is sensible in order to find the most promising fixed frequency or frequency density for each characteristic point and to thus achieve a good compromise between a prolonged measurement time and a high fitting accuracy.

Based on the analyses of the cell-to-cell variations and correlations of the investigated cell, two indices are at least necessary to characterise the parametric variation among cells: The most effective and time efficient parameter to depict the impedance variation is the R_AC_1000Hz impedance. To identify the variation of capacity the parameter C_DCH_CCCV should be determined.

4.4 Conclusion

The investigated cell shows small cell-to-cell parametric variations compared to other cells [9; 19]. For most parameters the respective variations are similar for both investigated batches.

The relative variation σ/μ of discharge capacity obtained during CC-phase is small (about 0.45%) and even smaller for C_DCH_CCCV (about 0.28%) with the influence of the variation of the cell impedance being reduced. In comparison, the relative variation of the ohmic AC impedance is still small but a little larger (about 0.72%, when considering batch B2 which shows no group building within the batch). This corresponds to variation ratios between cell capacity and ohmic impedance of 1:1.5 (CC) and 1:2.2 (CCCv) respectively. Due to the strong correlation between the two ohmic AC impedances R_AC_1000Hz and R_AC_Im0, it is justifiable to use the R_AC_1000Hz impedance during cell characterisation. The DC impedances all show the same statistical behaviour (relative variation about 1.3%). A high CC discharge capacity correlates to a small DC impedance, whereas a high CV discharge capacity correlates to a high DC impedance. The DC impedances do not show the group building which can be observed for the ohmic AC impedances of batch B1. Therefore, determining the ohmic cell impedance proves to be necessary during cell characterisation when aiming to determine the cell-to-cell-variation of the cell impedance.

For fitting purposes of ECMs, frequently used parameters are the ohmic AC impedance and the impedances of the local extrema within the Nyquist diagram R_{AC_max} and R_{AC_min} . The relative variation of the latter two parameters (about 8.1% and 2.8%) is found to be dependent on their respective frequency, which varies strongly (about 15.9% and 21.6%). A good compromise needs to be found between the number of low frequency points during an EIS-measurement resulting in a prolonged measurement time and the quality of fitting.

An important result from investigating the correlation between cell parameters, is that the cell impedance influences both, the discharge capacities and the mean temperature of the cell. A higher cell impedance leads to higher overpotentials during the discharge of the cell - therefore, the CC-phase is shorter. Reducing these overpotentials takes longer which increases the duration of the CV-phase. As the temperature mainly increases during the CC-phase, also the mean temperature during the CU-measurement is lower for cells with a higher impedance. For C_{DCH_CCCV} the influence of the variation of the cell impedance and therefore also of the temperature is reduced.

5

Influence of cell-to-cell variations on the inhomogeneity of battery modules

Regarding the findings of Chapter 4, the investigated cell reveals cell-to-cell variations for both, capacity and impedance. Even if the variations are small, they are still expected to affect the performance of a battery module in case no cell matching strategy is considered during battery module assembly but if the cells are chosen and assembled arbitrarily instead. The following chapter presents the simulative approach which examines the influence of cell-to-cell variations on the inhomogeneity of battery modules. First, the cell internal parameters which influence a cell's capacity and impedance are discussed. This discussion is crucial as within the chosen physicochemical modelling approach, cell-to-cell variations in capacity and impedance must be implemented by artificially modifying the parameterisation of the PCM using the internal cell parameters. Moreover, the developed multiscale multiphysics model is described. The resulting simulated inhomogeneous current distribution under cell-to-cell variations is presented for a generalised 2P module. Hereby the influence of the system terminal position, the impact on the Ah-throughput and the influence of the applied *C-Rate* is discussed. From the results, first implications for assembling battery modules are extracted regarding the connection of cells which show cell-to-cell variations.

This chapter is mainly based on the publication “Influence of cell-to-cell variations on the inhomogeneity of lithium-ion battery modules” by Rumpf et al. [39].

5.1 Influencing cell internal parameters on cell capacity and impedance

Inhomogeneity in battery modules can be influenced by cell-to-cell variations and by the module design. The module design includes the choice of assembled cell connectors and the thermal management of

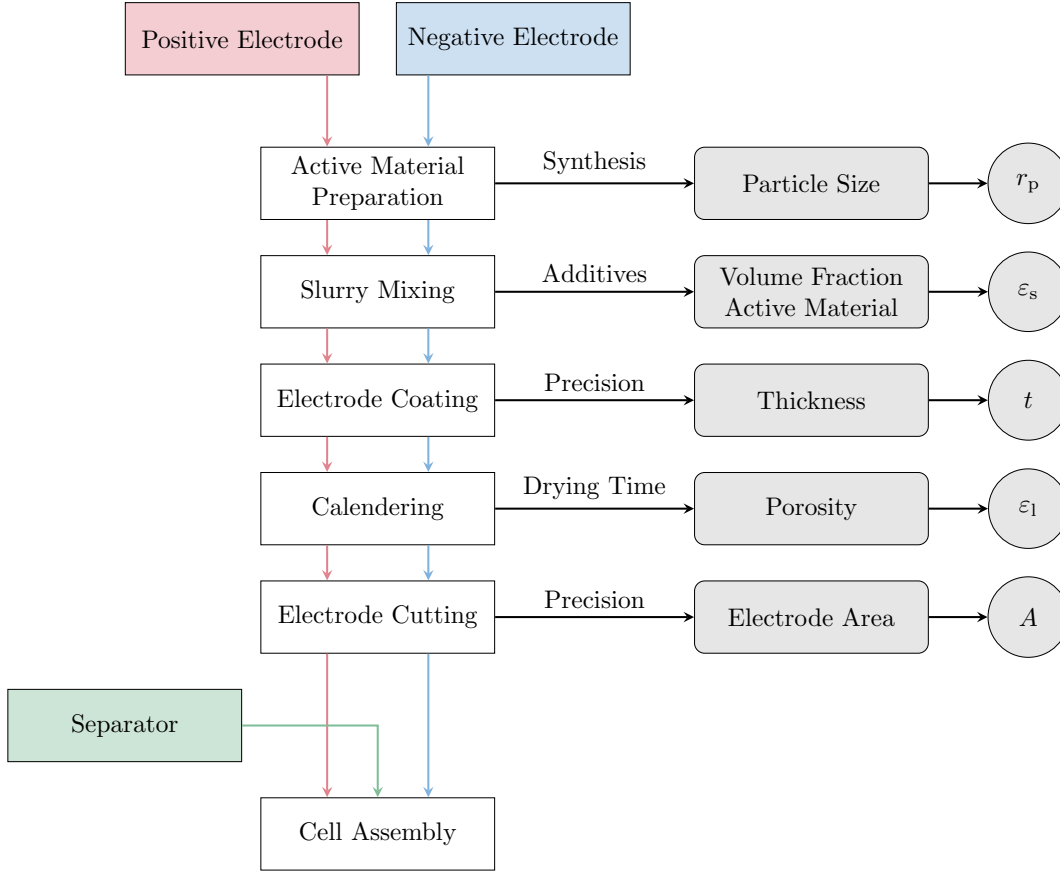


Figure 5.1: Manufacturing process chain for lithium-ion cells indicating the effect of variations during the manufacturing steps on internal cell parameters. Following the cell assembly, also the formation process can indirectly have an effect. The derived internal parameters are the particle size $r_{p,i}$ and volume fraction $\varepsilon_{s,i}$ of the active material as well as the thickness t_i , porosity $\varepsilon_{l,i}$ and area $A_{\text{electrode},i}$ of an electrode i ($i \in \{\text{neg}, \text{pos}\}$).

the system. Both, the cell connector resistances and evolving thermal gradients can influence the inhomogeneity in battery modules. Cell-to-cell variations in capacity and impedance are externally measurable but are contributed by multiple internal cell parameters [8]. For the presented investigation, the respective variations in capacity and impedance across the connected cells are to be adjusted within the single cell models. Therefore, the influence of these internal parameters on both, cell capacity and cell impedance, are discussed in the following.

During battery cell manufacturing, multiple processing steps are required, which can result in variations of cell internal parameters. Figure 5.1 provides an overview of the manufacturing process chain.

During the synthesis of the active material for the positive and negative electrode i ($i \in \{\text{neg}, \text{pos}\}$), different particles sizes $r_{p,i}$ can evolve. This active material is subsequently mixed to a slurry by using additives such as carbon black and binder. During this processing step the maximum active material weight percentage of the electrode is defined, which influences the active material volume fraction $\varepsilon_{s,i}$ of the electrode after the further processing steps. The slurry is then coated onto both sides of the respective current collector foil (copper for the negative electrode, aluminium for the positive electrode), which defines the initial electrode thickness. This initial thickness influences the final electrode thickness t_i after the further processing steps. As soon as the electrode roll has been calendered at a certain temperature and pressure over a certain drying time, the porosity of the

electrode $\varepsilon_{1,i}$ is set. By cutting the electrode roll into the desired length and width, the area of the electrode $A_{\text{electrode},i}$ is defined. The further processing of the cell depends on the cell format, which is to be produced. In case of Pouch cells, the electrodes are stacked or z-folded with separators in between the positive and negative electrode. In case of prismatic or cylindrical cells, the jelly roll is produced by winding the positive electrode, separator and negative electrode around a mandrel. The produced electrode stack or jelly roll is inserted into a Pouch foil or a can respectively, the internal tabs are welded to the external cell poles and the cell is filled with electrolyte. After the formation process and the final sealing of the cell, it is ready for use. A deviation in any of these processing steps can influence the cell internal parameters which might in turn affect the cell's final capacity and impedance. These possible influences on the cell capacity and impedance are discussed in the following.

5.1.1 Influences on cell capacity

A cell's capacity is influenced by the respective capacities of the positive and negative electrode, which are balanced according to cell design requirements [107]. Based on a volumetric perspective, the capacity of a porous electrode i ($i \in \{\text{neg}, \text{pos}\}$) calculates as follows [108]:

$$C_i = A_i \cdot t_i \cdot \varepsilon_{s,i} \cdot c_{s,\text{max},i} \cdot (x_{100} - x_0) \cdot F_{\text{const}} \quad (5.1)$$

A_i (m^2) is the area of the electrode, t_i (m) is the thickness of the electrode, $\varepsilon_{s,i}$ is the active material volume fraction within the electrode, $c_{s,\text{max},i}$ (mol m^{-3}) is the theoretical maximum concentration of lithium in the active material, $[x_0, x_{100}] \in [0, 1]$ is the range of stoichiometry during operation and F_{const} is the Faraday constant. When considering the limiting electrode, a change in one of these internal parameters, will change the capacity of the electrode and thus also of the lithium-ion cell.

Pre-studies have shown, that a variation of the influencing cell internal parameters has different effects.

The electrode area $A_{\text{electrode},i}$ could either vary due to the production process in case the cutting of electrodes was imprecise. Or it could decrease effectively over the cell's lifetime due to ageing effects such as loss of active material. Note, that an electrode overhang area as reported by Wilhelm et al. [109] is neglected in this investigation on cell level. Moreover, $A_{\text{electrode},\text{neg}} = A_{\text{electrode},\text{pos}} = A_{\text{electrode}}$ is considered the same for both electrodes and therefore varying this parameter in the model will not change the balancing of the two electrodes to each other. As the PCM is a p2D physicochemical model, the electrode stack is modelled in 1D and within the model $A_{\text{electrode}}$ is only used to scale the applied current density with respect to the rated capacity C_{rated} of the simulated cell and the chosen *C-Rate*:

$$j_{\text{rate}} = C\text{-Rate} \cdot j_{1C} = C\text{-Rate} \cdot \frac{C_{\text{rated}}}{A_{\text{electrode}} \cdot 1 \text{ h}} \quad (5.2)$$

Therefore, changing $A_{\text{electrode}}$ within the model will result in a different applied current density and thus in an adapted discharge duration and in a changed effective discharge capacity of the cell. However, it cannot be used to scale the cell's capacity in a physicochemical understanding as this influence is not implemented in the model.

A variation in the electrode thickness t_i could be explained by a variation during the production process while coating the current collector with the electrode slurry or while calendaring the electrode. Changing the electrode thickness t_i in the model implies an influence on the length of electric and ionic paths through the active material and electrolyte between separator and current collector. These

longer transport ways through the electrode result in different overpotentials and thus in different current densities.

A variation in the active material volume fraction $\varepsilon_{s,i}$ could be explained by a variation during the production process while calendaring the electrode. The denser the electrode is to be calendared, the higher will the active material volume fraction be compared to the fraction of electrode porosity ε_1 (which equals the volume fraction of the electrolyte). Within the model, $\varepsilon_{s,i}$ influences the active specific surface area $a_v = \frac{3\varepsilon_{s,i}}{r_{p,i}}$, where $r_{p,i}$ (m) is the mean particle radius within the electrode (note, that spherical particles are assumed in the model). a_v influences the local current source i_v , the polarisation η and thus finally the local current density j_{loc} within the electrode.

The theoretical maximum concentration of lithium in the active material of an electrode $c_{s,max,i}$ is a material parameter. It calculates from the volumetric theoretical capacity of an electrode and depends on the density of the active material $\varrho_{AM,i}$ (kg m^{-3}) and its molar mass M_i (g mol^{-1}).

$$c_{s,max,i} = \frac{c_{v,th,i}}{z \cdot F_{const}} = \frac{c_{g,th,i} \cdot \varrho_{AM,i}}{z \cdot F_{const}} = \frac{\varrho_{AM,i}}{M_i} \quad (5.3)$$

It can thus vary for different active material formulations. Within the model, $c_{s,max,i}$ affects the electrode kinetics during lithium intercalation by contributing to the exchange current density j_0 at the boundary between electrode particle and electrolyte. j_0 scales the local current density j_{loc} in the Butler-Volmer equation within the electrode.

The stoichiometric range $[x_0, x_{100}]$ defines the utilisation factor of the specific electrode. Within the model, the electrode stoichiometry at the lithiated state of the full cell x_{100} can be used to set the SOC of the electrode and thus of the full cell. It scales the initial lithium concentration $c_{s,0,i}$ within an electrode, which influences the exchange current density j_0 and the local current density j_{loc} within the electrode. Using the electrode stoichiometry as capacity variation parameter results not only in adapting the voltage range, within which the electrode can be cycled but also the absolute voltage level of the cell.

As the voltage level of the cell shall not be changed when implementing a cell capacity variation within the model, the internal parameter $\varepsilon_{s,neg}$ is used for capacity adaption in the model.

5.1.2 Influences on cell impedance

Different authors have investigated the influence of cell internal parameters on the cell's impedance at different time constants [110–118].

The impedance of a lithium-ion cell is contributed by both electrodes ($i \in \{\text{neg, pos}\}$) due to the electrode thickness t_i , the specific surface area of the electrode's porous material $a_{v,i}$, the solid phase electric and liquid phase ionic conductivity $\sigma_{s,i}$ and κ_l , and the diffusion coefficient of the salt in the liquid phase D_l [113–115]. The latter three parameters are to be corrected by the respective porous electrode's tortuosity τ_i . Additionally, also the internal contact resistances between current collectors and active materials [115] as well as the impedances of the current collectors as such [118] influence the cell impedance. Reimers et al. [118] have developed an equation to calculate this latter impedance R_{foil} , which depends on the respective tab arrangement and length $x_{electrode}$ of the electrode stack design as well as on the specific electric resistances of the current collectors $R_{coll,neg}$ and $R_{coll,pos}$ (compare Equation 5.23).

All of these different contributions to the cell impedance are active within different frequency ranges as their related electrochemical processes have different time constants. As has been shown in the experimental investigation in Chapter 4, the ohmic AC impedances have been able to depict a statistic group building within a batch of production fresh cells, whereas the DC impedances with time constants of 10 s to 60 s have not. Therefore, in the simulative investigation presented in this thesis, a variation in the cell impedance is to be adapted using an ohmic impedance within the model. Therefore, the internal foil resistance R_{foil} is used, which makes up about 40 % (compare Equation 5.23) of the rated cell impedance $R_{\text{cell}} = 18 \text{ m}\Omega$ (determined at $f = 1000 \text{ Hz}$).

5.1.3 Variation range for parameters

Within Chapter 4, the variations in capacity and impedance of two batches of cells (600 and 500 cells respectively) have been measured. Batch B1 showed a strong group building within the variation of the ohmic cell impedance which resulted in a coefficient of variation $\sigma/\mu|_{R_{\text{AC_Im0,B1}}} = 1.82 \%$. Here, σ is the standard deviation around the mean μ of the respective parametric variation. Therefore, the results for batch B2 had been more significant for further studies. For batch B2, the CC and CCCV discharge capacity as well as ohmic cell impedance showed a coefficient of variation $\sigma/\mu|_{C_{\text{DCH_CC,B2}}} = 0.48 \%$, $\sigma/\mu|_{C_{\text{DCH_CCCV,B2}}} = 0.33 \%$ and $\sigma/\mu|_{R_{\text{AC_Im0,B2}}} = 0.73 \%$ respectively. These variations are in the same range as those reported by Campestrini et al. [20] but are smaller than those reported by other groups [9; 18; 19]. Therefore and due to the possibility of group building even within a labelled batch of cells, the worst case variations within a battery module should be considered significantly higher than the measured standard deviations – even for high quality commercial cells. If a certain cell-to-cell variation is normally distributed, then 99.73 % of the respective parameters lie within $\mu \pm 3\sigma$ [63]. In case cells are chosen arbitrarily from a batch of delivered cells during battery module assembly, the cell-to-cell variations can be up to $\mu \pm 3\sigma$. Therefore, the following maximum variations around the rated capacity and impedance of the cell are to be used during the simulative investigation in this study. These variations are used to worsen one cell and improve the other cell within the module topology:

$$\begin{aligned} dC &= \pm 1.5 \% = \pm 0.045 \text{ Ah} \\ dR &= \pm 4 \% = \pm 0.72 \text{ m}\Omega \\ dT &= \pm 2.5 \text{ K} \end{aligned} \tag{5.4}$$

An absolute thermal gradient $|dT| = 5 \text{ K}$ is chosen for this study as this value has been reported as the maximum allowable thermal gradient within battery modules during operation [81; 119; 120] in order to avoid about 25 % accelerated ageing kinetics and up to 50 % variance in power capability [120].

Temperature cell-to-cell variations are investigated against the background that an inefficient thermal management or an external heat source next to one side of the battery module can lead to temperature gradients across a module [15; 16], which results in a current deviation between parallel connected cells or strings [17].

For the cell internal model parameters the attributed variations imply a change in the active material volume fraction by $d\varepsilon_{s,\text{neg}} = \pm 6.9 \times 10^{-3}$, a change in the internal foil resistance by $dR_{\text{foil}} = \pm 0.72 \text{ m}\Omega$ and a change in the initial reference temperature of the cells by $dT_{\text{ref}} = \pm 2.5 \text{ K}$ based on the respective values for the homogeneous system as stated in Table 5.4 and Table 5.5.

5.2 Model development

The developed model of connected cells is based on the multiscale multiphysics model for single cells [92; 121–124] and consists of multiple coupled submodels (compare Figure 5.2): Each cell is simulated by a p2D PCM after Doyle, Fuller and Newman [58–61] in order to account for the physicochemical behaviour of the cell (compare green box in Figure 5.2). On cell level, this PCM is coupled bidirectionally to a 0D THM of the cell (compare purple box in Figure 5.2), which in turn allows for implementing temperature dependent cell parameters within the PCM.

For the electrical coupling of multiple cells, a 0D ELM is used (compare blue box in Figure 5.2). Regarding the thermal model of connected cells (compare orange box in Figure 5.2), the thermal single cell model is enhanced by additionally considering the cell connectors. Furthermore, heat transfer mechanisms are implemented between cells, connectors and the surrounding air. The ELM is supplied with the total system current i_{app} which is provided by the Operation model part (compare yellow box in Figure 5.2). The presented model is built and solved in COMSOL Multiphysics 5.3a.

5.2.1 Physicochemical model

The physicochemical behaviour of each single cell is described by a p2D PCM as described in Chapter 3.4.

5.2.2 Thermal model

The thermal behaviour of each single cell is modelled using a 0D THM. During operation, heat is generated within the lithium-ion cell due to different reasons: activation, concentration and ohmic losses [90]. This heat can be calculated using the simplified Bernardi Equation [125]:

$$q_{\text{gen}} = i_{\text{cell}}(E_{\text{eq}} - \phi_{\text{cell}}) - i_{\text{cell}}\left(T_{\text{cell}} \frac{\partial E_{\text{eq}}}{\partial T_{\text{cell}}}\right) \quad (5.5)$$

i_{cell} (A) is the cell current, E_{eq} (V) is the open circuit potential of the cell, ϕ_{cell} (V) is the cell potential and T_{cell} (K) is the average cell temperature. The first term describes the heat due to the cell's overpotential occurring due to ohmic losses, charge-transfer overpotentials, and mass transfer limitations, i.e. irreversible polarisation heat. The second term describes the reversible part of the generated heat, i.e. entropic heat, which occurs due to a change in entropy. [125]

The heat which is generated by the cell is partly stored by the cell (q_{stored} in W) due to the cell's heat capacity and partly dissipated to the environment by three heat transfer processes: First, by conduction via the cell terminals (q_{cond} in W). Second, by natural or forced convection via the surrounding air (q_{conv} in W). Third, by radiation (q_{rad} in W).

$$q_{\text{stored}} = m_{\text{cell}} c_{\text{p,cell}} \frac{\partial T_{\text{cell}}}{\partial t} \quad (5.6)$$

$$q_{\text{cond}} = k_{\text{contact}} A_{\text{contact}} \frac{T_{\text{cell}} - T_{\text{contact}}}{x_{\text{contact}}} \quad (5.7)$$

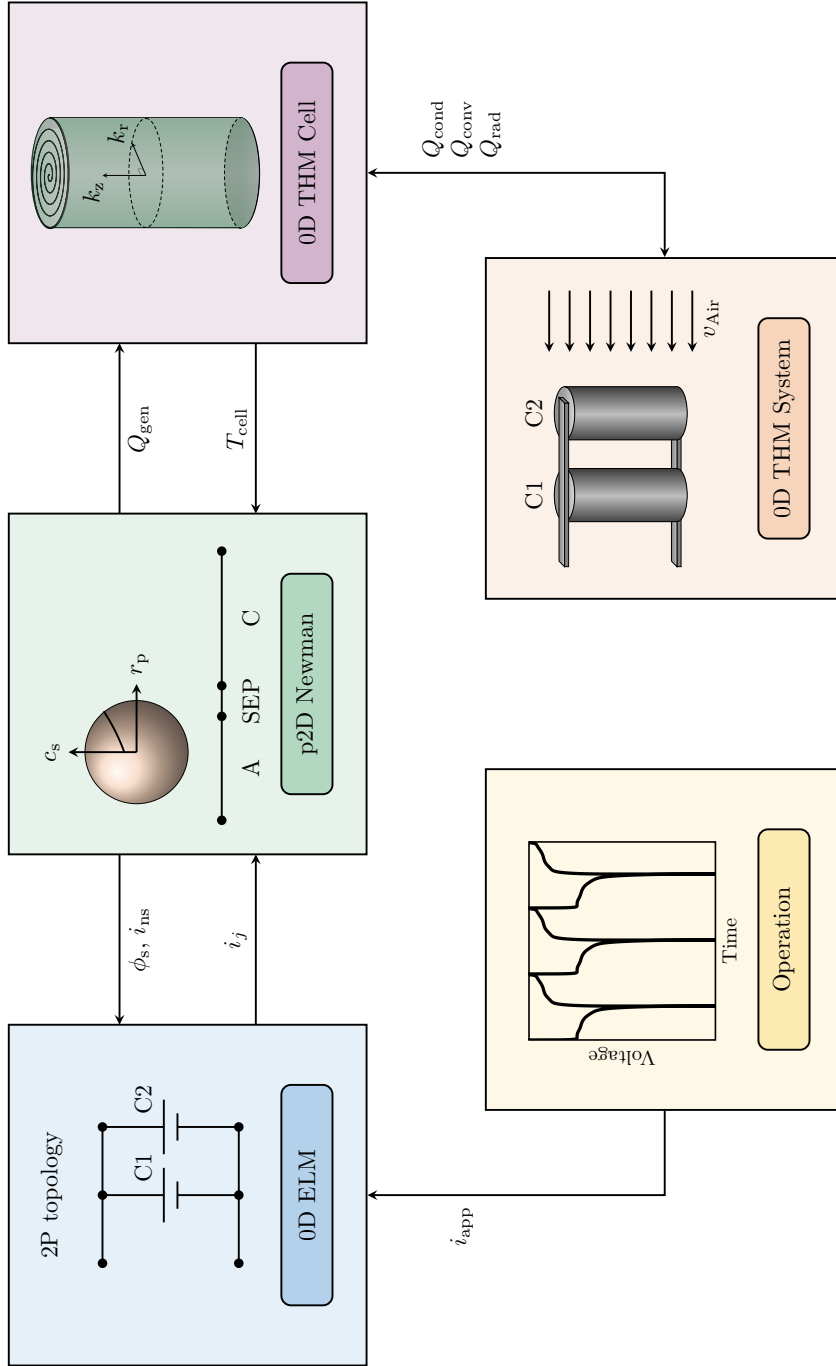


Figure 5.2: Scheme of the multidimensional coupled model of connected lithium-ion cells: Each cell is physicochemically modelled using a p2D Newman model (PCM: green box) and thermally modelled using a 0D lumped thermal model (THM Cell: purple box). The generated heat Q_{gen} is calculated in the PCM and coupled to the THM of the cell. In turn, the adapted cell temperature T_{cell} is coupled back to the PCM. The connection of multiple cells is electrically modelled in 0D (ELM: blue box) and thermally modelled in 0D (THM System: orange box) by considering cell connectors, surrounding air and heat fluxes Q_{cond} , Q_{conv} and Q_{rad} in between. Note, that a capital Q denotes that the heat fluxes have been averaged over the cell volume. The ELM is supplied with the total system current which is provided by the Operation model part (yellow box).

$$q_{\text{conv}} = h_{\text{conv}} A_{\text{cell}} (T_{\text{cell}} - T_{\text{amb}}) \quad (5.8)$$

$$q_{\text{rad}} = \varepsilon_{\text{rad}} \sigma_{\text{B}} A_{\text{cell}} (T_{\text{cell}}^4 - T_{\text{amb}}^4) \quad (5.9)$$

Here, m_{cell} (kg) is the mass and $c_{\text{p,cell}}$ ($\text{J kg}^{-1} \text{K}^{-1}$) is the specific heat capacity. T_{contact} (K) is the temperature of the contact area A_{contact} (m^2) at the cell poles, x_{contact} (m) is the thickness of the contact area and k_{contact} ($\text{W m}^{-1} \text{K}^{-1}$) is the thermal conductivity of the cell contacts. T_{amb} (K) is the temperature of the ambient air, A_{cell} (m^2) is the surface area of the cell which is exposed to the surrounding air (strictly speaking, the portion of the surface area which is covered by the cell contacts, must not be taken into account), h_{conv} ($\text{W m}^{-2} \text{K}^{-1}$) is the convective heat transfer coefficient, ε_{rad} is the emissivity of the cell and σ_{B} is the Stefan-Boltzmann constant.

Within a lithium-ion cell, heat conduction is the only heat transport mechanism [61]. Due to its layered and wound nature (compare Figure 3.1), a lithium-ion cell shows an anisotropic behaviour regarding its thermal conductivity. The thermal conductivity across a cell stack k_{r} (through the layers, in case of cylindrical cells in radial direction) is one to two magnitudes smaller than the thermal conductivity along the layers of the cell stack k_{z} (in case of cylindrical cells in axial direction) [94–96]. In case the mass ratios of the cell components are known, the thermal conductivities as well as the heat capacity of the cell can be calculated as described in Chapter 3.5.2.

The heat dissipation mechanisms (compare Equations 5.6 to 5.9) serve as boundary conditions for the energy system. In order to comply with the energy balance equation, the generated heat must equal the sum of stored and dissipated heat.

$$q_{\text{gen}} = q_{\text{stored}} + q_{\text{cond}} + q_{\text{conv}} + q_{\text{rad}} \quad (5.10)$$

$$\begin{aligned} i_{\text{cell}}(E_{\text{eq}} - \phi_{\text{cell}}) - i_{\text{cell}}(T_{\text{cell}}) \frac{\partial E_{\text{eq}}}{\partial T_{\text{cell}}} = & + m_{\text{cell}} c_{\text{p,cell}} \frac{\partial T_{\text{cell}}}{\partial t} \\ & + k_{\text{contact}} A_{\text{contact}} \frac{T_{\text{cell}} - T_{\text{contact}}}{x_{\text{contact}}} \\ & + h_{\text{conv}} A_{\text{cell}} (T_{\text{cell}} - T_{\text{amb}}) \\ & + \varepsilon_{\text{rad}} \sigma_{\text{B}} A_{\text{cell}} (T_{\text{cell}}^4 - T_{\text{amb}}^4) \end{aligned} \quad (5.11)$$

This equation is only valid if the cell can be considered having a homogeneous temperature distribution from centre to surface and thus if the implementation of a lumped thermal model is justifiable. Whether this simplification can be assumed, is to be determined by calculating the Biot number Bi . Bi relates the internal heat conduction resistance ($r_{\text{cell}}/k_{\text{r}}$) to the external heat transfer resistance ($1/h_{\text{conv}}$) [101], where r_{cell} is the radius and k_{r} is the radial thermal conductivity of the cylindrical cell.

$$\text{Bi} = \frac{h_{\text{conv}} r_{\text{cell}}}{k_{\text{r}}} \quad (5.12)$$

If $\text{Bi} < 0.1$, the cell's centre temperature T_{centre} and the cell's surface temperature T_{surf} differ by less than 2% of the temperature difference between the cell surface temperature and the ambient temperature ($T_{\text{surf}} - T_{\text{amb}}$) [99]. For the presented 26650 cell, the Biot number calculates to $\text{Bi} = 0.292$, so this is a marginal case. Assuming a lumped thermal model for the cell means neglecting the cell internal temperature gradients. However, for the presented study, this simplification can be accepted

due to three reasons: First, this assumption will decrease the required solving time of the model significantly compared to thermal cell models in higher dimensions. Second, under small loads as used in this study, the temperature gradient within a cylindrical cell is reasonably small [74]. Third and most important, the focus of this work is to investigate inhomogeneity within battery modules, not cells. While keeping in mind that the cell temperature will be higher in the respective cell's centre than depicted in the results, the discussed gradients across the battery module and the derived principle conclusions are still valid. Therefore, a lumped thermal model is implemented, Equation 5.11 is used for the THM of the single cell and the anisotropic thermal conductivity within the cell is neglected. The heat related terms can thus be averaged over the volume of the cylindrical cell, which is denoted by a respective capital Q within the THM.

The convective heat transfer coefficient h_{conv} depends on dimensionless parameters such as Nusselt, Reynolds and Prandtl number (Nu , Re , Pr) as well as on the geometry of the overflowed cell or bunch of cells respectively [99]. It thus defines the heat transfer to an overflowing fluid. For a single cylindrical 26650 cell $h_{\text{conv}} = 22.5 \text{ W m}^{-2} \text{ K}^{-1}$ has been calculated for $v_{\text{air}} = 1 \text{ m s}^{-1}$, $k_{\text{air}} = 0.0259 \text{ W m}^{-1} \text{ K}$, $\nu_{\text{air}} = 1.6 \times 10^{-5} \text{ m}^2 \text{ s}^{-1}$, $\text{Pr} = 0.72$ and $T = 25 \text{ }^\circ\text{C}$ (for the detailed calculation see Chapter 3.5.3.1). Note, that during this investigation, each cell within the battery module is attributed the same h_{conv} value. Regarding the forced convection around a bunch of cells, the fluid dynamic parameters and thus h_{conv} change compared to those for a single cell (compare Chapter 3.5.3.2). They are affected by the arrangement of the cylindrical cells (staggered or aligned) and by the distance between two adjacent cells [101]. Especially when the influence of cell arrangements on evolving thermal gradients during operation is examined, h_{conv} should be adapted for the assembled cells dependent on their respective position within the battery module [101].

In a real system, connected cells will interact electrically and thermally via the cell connectors. However, the aim is to investigate the pure influence of cell-to-cell variations on the module inhomogeneity and to compare the results to those when the connected cells are exposed to thermal gradients across the module. Thermal cell coupling by conduction would smear the effects of different influencing factors. This would make it harder to differentiate between and to compare the different effects. Therefore, the individual cells are considered to be at isothermal conditions throughout the conducted study. The cells are not able to interact thermally via the cell connectors but only electrically. Thermal conduction between two adjacent cells is therefore not taken into account during this study.

5.2.3 Electrical model

The 0D ELM of the battery module uses the Kirchhoff circuit laws for lumped electric circuit models: (1) The sum of the currents flowing into a node equals the sum of the currents flowing out of the node (conservation of charge). Here, n equals the number of currents around the considered node.

$$\sum_{k=1}^n i_k = 0 \quad (5.13)$$

(2) The directed sum of the electrical potential differences within any closed network is zero (mesh rule). Here, n equals the number of electric potential differences within the considered mesh.

$$\sum_{k=1}^n u_k = 0 \quad (5.14)$$

Not only the lithium-ion cells are considered in the electric model but also the electrical resistances of the cell connectors (R_p , R_n) and welding spots (R_{wsp} , R_{wsn}) for both, the positive and negative pole of the cell. By doing so, use cases with single defective welding spot joints and asymmetric cell connectors can be investigated. These elements need to be considered in the electric circuit model. Figure 5.3 depicts the different equivalent electric circuits for the respective investigated topologies.

The following assumptions are met in the model: The cell connectors are made of Hilumin (nickel plated steel) [126], the distance between two adjacent cells is $dx_{\text{cell}} = 5$ mm, the cell connectors are spot welded to the respective pole of the cell and four welding spots are used per cell pole. Table 5.5 summarises the geometric and electric data of the Hilumin cell connectors as well as the cross sectional area and corresponding electric resistance of the welding spots.

The equations of the electric model depend on the investigated module topology. Different equations apply for serial, parallel and combined cell connections and will be derived in the following.

Regardless of the topology, the current flowing into a cell i at its negative pole $i_{n,\text{cell},i}$ must equal the current flowing out of the cell at its positive pole $i_{p,\text{cell},i}$ (conservation of charge) and can therefore be termed $i_{\text{cell},i}$.

$$i_{n,\text{cell},i} = i_{p,\text{cell},i} = i_{\text{cell},i} \quad (5.15)$$

5.2.3.1 Serial connected cells

For x serial connected cells within a string j , the current flowing through the cells is equal and the cell potentials sum up. A string of two serial connected cells consists of the two cells, their welding spot joint resistances, their respective cell connectors and a cell connector R_{conn} in between the two cells (compare Figure 5.3 2S). $i_{n,j}$ denotes the current at the negative end of string j . $i_{p,j}$ denotes the current at the positive end of string j . Based on Kirchhoff's laws, the two currents are equal and can therefore be termed i_j .

$$i_{p,j} = i_{n,j} = i_j \quad (5.16)$$

As only one string of serial connected cells is considered in the 2S topology, i_j ($j = 1$) equals the overall applied system current i_{app} , which is provided by the Operation module part (compare yellow box in Figure 5.2) and which is applied at the system terminal (ST) of the ELM.

$$i_j = i_{\text{app}} \quad (5.17)$$

These equations can be generalised for x serial connected cells. For any number of x serial connected cells, the respective cell currents equal the string current.

5.2.3.2 Parallel connected cells

When considering the operation of a system of y parallel connected cells, the cell current equals the string current within the respective parallel connected string j . In the case of the system terminal (ST) being located left of string 1 (as illustrated in Figure 5.3 2P for $y = 2$), the following equations apply.

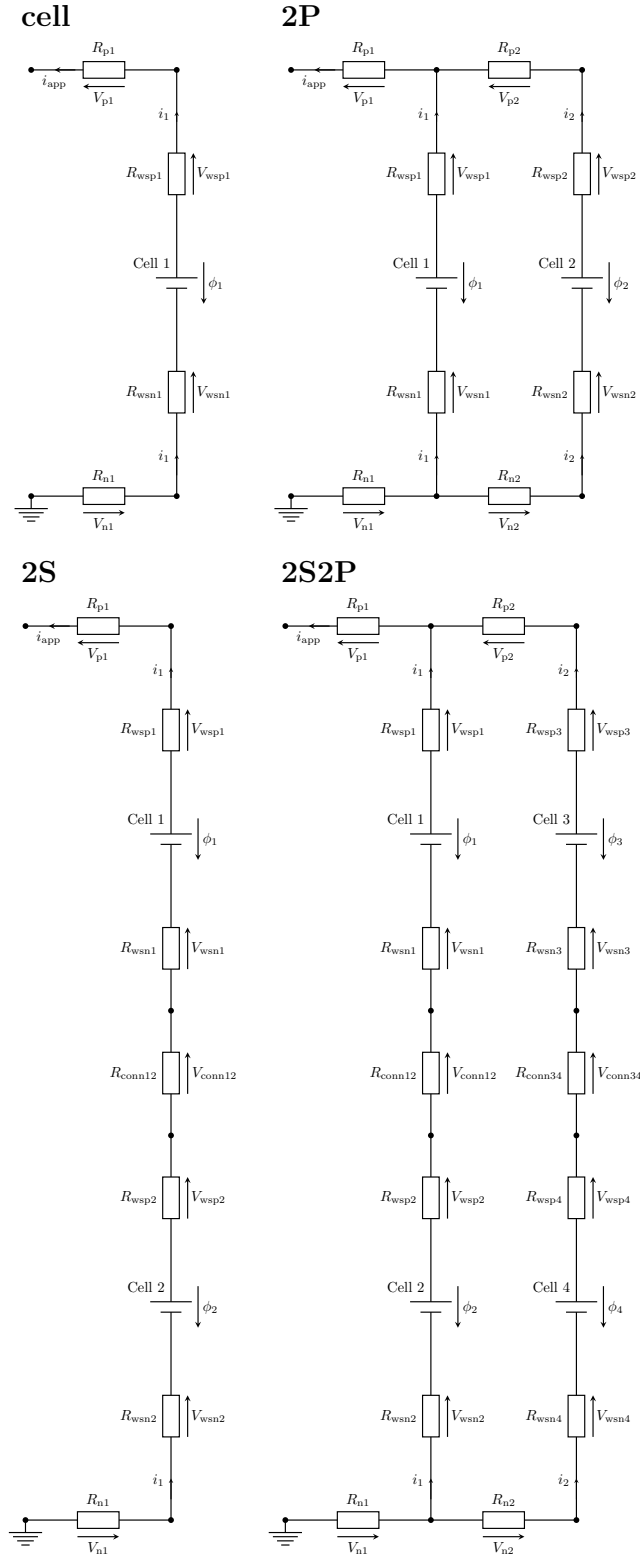


Figure 5.3: Equivalent electric circuits of different topologies considering both, battery cells and the resistances of cell connectors and welding spot joints. Note, that within a string of x serial connected cells, the cells are numbered from top to bottom and when connected in parallel, the strings are numbered from left to right. The positive and negative connector resistances $R_{p,j}$ and $R_{n,j}$ are numbered according to the closest adjacent string on the right hand side of the respective connector.

Based on the first circuit law of Kirchhoff, the current through the j th string i_j equals the difference of the applied current i_{app} at the ST of the ELM (which is provided by the Operation module part) and the sum of currents which flow through all other parallel connected strings. Using Equation 5.13, the following equation holds true for every parallel connected string j :

$$i_j = i_{\text{app}} - \sum_{\substack{k=1 \\ k \neq j}}^y i_k \quad (5.18)$$

Based on the second law of Kirchhoff, the enclosed network equation can be set up considering the mesh between string 1 and string 2, and solved for the current flowing through string 1.

$$i_1 = \frac{\phi_1 - \phi_2 + (R_{p2} + R_{n2} + R_{\text{wsp}2} + R_{\text{wsn}2}) \cdot i_2}{R_{\text{wsp}1} + R_{\text{wsn}1}} \quad (5.19)$$

This equation can be generalised for any number of y parallel connected strings. However, it must be distinguished, whether the system terminal (ST) of the battery module is located at the side of the parallel connected strings (compare Figure 5.4 ST_{side}), i.e. close to string $j = 1$ or $j = y$. Or, whether the ST is located somewhere in the middle of the parallel connected strings (compare Figure 5.4 ST_{mid}), i.e. in between two strings $j \in [2, y - 1]$. Furthermore, the equation adapts dependent on whether the respective string is located just at the ST or further away from it, and moreover whether it is located left or right of the ST. For each of these cases a general equation for the respective string current i_j is derived depending on the number of parallel connected strings y , resistances of cell connectors and welding spot joints. Figure 5.4(c) provides two flow charts (one for ST_{side} and one for ST_{mid}) on which equation to choose according to the respective strings' position relative to the ST. Table 5.1 and Table 5.2 state these general equations for a ST_{side} and ST_{mid} connection respectively (set $x = 1$ for a pure parallel connection of cells), which form the base for the coupling equations between ELM and PCM (compare Section 5.2.4). Note, that the equations for the string currents i_j within the Tables 5.1 and 5.2 are derived using the second law of Kirchhoff. For the remaining string currents on the right hand side of each of the equations in the table, the first law of Kirchhoff (compare Equation 5.18) must be used for their definition.

A ST_{side} connection results from a asymmetric current collector design. A ST_{mid} connection represents a fully symmetric current collector design if only two strings are connected in parallel and if the ST is situated in the middle of the two strings. As soon as more strings are connected, the ST_{mid} case represents a half symmetric current collector design. To make this case fully symmetric, the ST would have to be situated at a cross position, e.g. the lower ST at the lower left end and the upper ST at the upper right end of the parallel connected strings. As investigating the influence of a disadvantageous current collector design in combination with cell-to-cell variations is more relevant, the focus of this work is on an ST_{side} connection. In order to compare the results to a symmetric current collector design, the current distribution within a 2P module is analysed, wherefore the symmetric case can be covered by a ST_{mid} connection.

5.2.3.3 Combined connected cells

For combined connected cells, y strings of x serial connected cells are subsequently connected in parallel. Therefore, the equations for serial and parallel connected cells must be combined. Within each of the strings j , still, the current at the positive end of the string $i_{p,j}$ equals the current at the negative end of

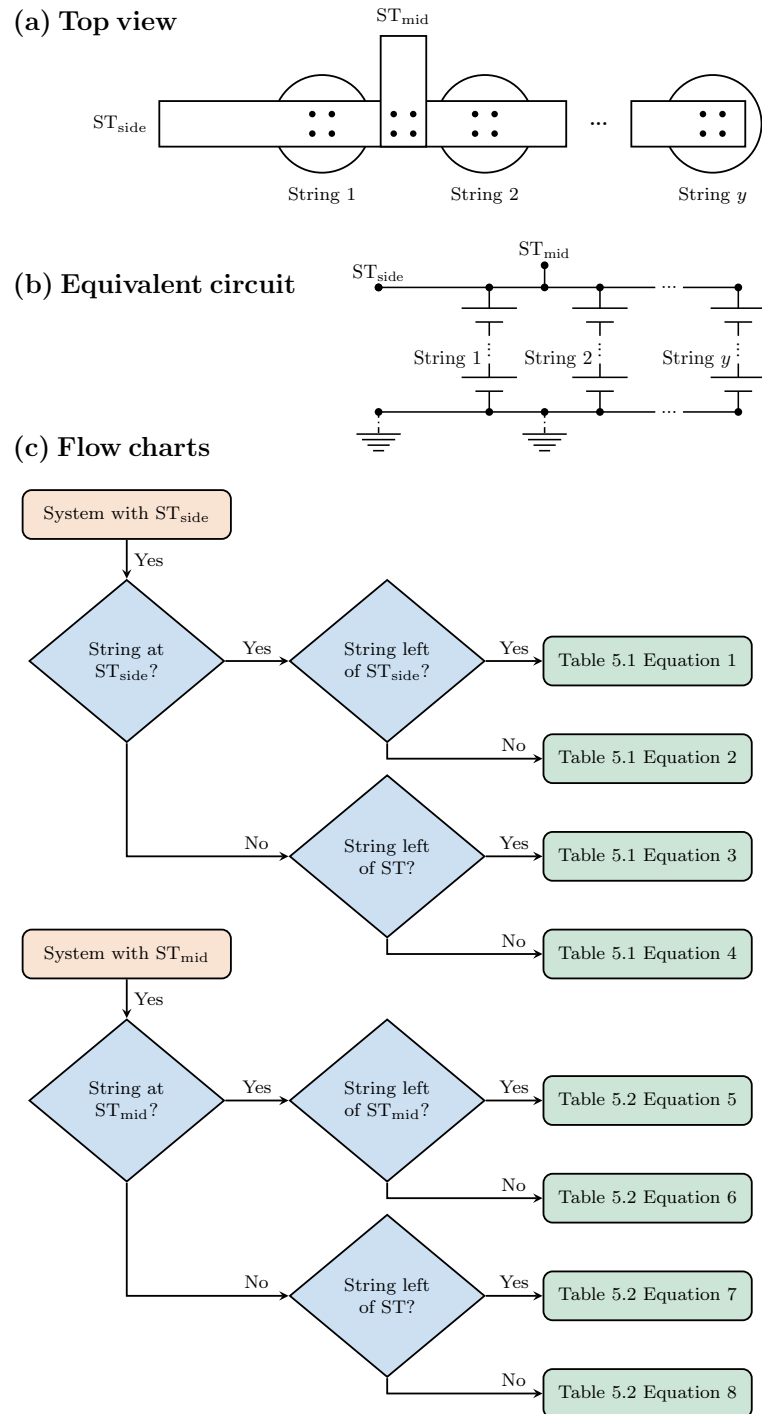


Figure 5.4: (a) Top view of parallel connected cells or strings. The cell connector is spot welded on the poles of the cells. The system terminal (ST) can either be located at the side (ST_{side}) or in the middle (ST_{mid}) of the parallel connection. (b) Equivalent circuit of parallel connected strings illustrating the different locations of the ST. (c) Flow charts for all $xSyP$ topologies about which equation in Table 5.1 (for ST_{side}) and in Table 5.2 (for ST_{mid}) to choose for determining the string current i_j for all cells within a string j according to the string position relative to the ST. Please note, that the respective flow chart needs to be run through once for each of the connected strings $j \in [1, y]$. For a pure parallel connection, set $x = 1$. For a pure serial connection, set $y = 1$.

Table 5.1: General ELM equations for the string currents i_j within $xSyP$ topologies contacted at ST_{side} , which are valid for $x \geq 1$, $y \geq 1$, except for 1S1P. Set $x = 1$ for a pure parallel connection. Set $y = 1$ for a pure serial connection. According to the decision flow charts (compare Figure 5.4(c)), the adequate equation for the desired string current i_j can be chosen dependent on the position of the string j relative to the system terminal (ST). The currents of the remaining strings on the respective right hand side of each of the equations in the table must be defined using the first law of Kirchhoff (compare Equation 5.18). Note, that within a string of x serial connected cells, the cells are numbered from top to bottom and when connected in parallel, the strings are numbered from left to right. The positive and negative connector resistances $R_{p,j}$ and $R_{n,j}$ are numbered according to the closest adjacent string on the right hand side of the respective connector. Note, that the equations numbers A to E refer to mathematical terms which are repeated within the equations 1 to 4.

#	Equation
1	$i_j = \left(\sum_{k=(j-1)x+1}^{jx} (\phi_k) - \sum_{\substack{k=(j-2)x+1 \\ y>1}}^{(j-1)x} (\phi_k) + A + (R_{p,j} + R_{n,j}) \cdot \sum_{k=1}^{j-1} (i_k) \right) \cdot C^{-1}$
2	$i_j = \left(\sum_{k=(j-1)x+1}^{jx} (\phi_k) - \sum_{\substack{k=jx+1 \\ y>1}}^{(j+1)x} (\phi_k) + B + (R_{p,(j+1)} + R_{n,(j+1)}) \cdot \sum_{k=j+1}^y (i_k) \right) \cdot C^{-1}$
3	$i_j = \left(\sum_{k=(j-1)x+1}^{jx} (\phi_k) - \sum_{k=jx+1}^{(j+1)x} (\phi_k) + B - (R_{p,(j+1)} + R_{n,(j+1)}) \cdot \sum_{k=1}^{j-1} (i_k) \right) \cdot D^{-1}$
4	$i_j = \left(\sum_{k=(j-1)x+1}^{jx} (\phi_k) - \sum_{k=(j-2)x+1}^{(j-1)x} (\phi_k) + A - (R_{p,j} + R_{n,j}) \cdot \sum_{k=j+1}^y (i_k) \right) \cdot E^{-1}$
A	$\sum_{\substack{k=(j-2)x+1 \\ y>1}}^{(j-1)x} (R_{wsp,k} + R_{wsn,k}) \cdot i_{(j-1)} + \sum_{\substack{k=(j-2)x+1 \\ x>1 \\ y>1}}^{(j-1)x-1} (R_{conn,(k)(k+1)}) \cdot i_{(j-1)}$
B	$\sum_{\substack{k=jx+1 \\ y>1}}^{(j+1)x} (R_{wsp,k} + R_{wsn,k}) \cdot i_{(j+1)} + \sum_{\substack{k=jx+1 \\ x>1 \\ y>1}}^{(j+1)x-1} (R_{conn,(k)(k+1)}) \cdot i_{(j+1)}$
C	$\sum_{k=(j-1)x+1}^{jx} (R_{wsp,k} + R_{wsn,k}) + \sum_{\substack{k=(j-1)x+1 \\ x>1}}^{jx-1} (R_{conn,(k)(k+1)})$
D	$(R_{p,(j+1)} + R_{n,(j+1)}) + C$
E	$(R_{p,j} + R_{n,j}) + C$

Table 5.2: General ELM equations for the string currents i_j within $xSyP$ topologies contacted at ST_{mid} , which are valid for $x \geq 1, y \geq 1$, except for 1S1P. Set $x = 1$ for a pure parallel connection. Set $y = 1$ for a pure serial connection. According to the decision flow charts (compare Figure 5.4(c)), the adequate equation for the desired string current i_j can be chosen dependent on the position of the string j relative to the system terminal (ST). The currents of the remaining strings on the respective right hand side of each of the equations in the table must be defined using the first law of Kirchhoff (compare Equation 5.18). Note, that within a string of x serial connected cells, the cells are numbered from top to bottom and when connected in parallel, the strings are numbered from left to right. The positive and negative connector resistances $R_{p,j}$ and $R_{n,j}$ are numbered according to the closest adjacent string on the right hand side of the respective connector. Note, that the equations numbers A to G refer to mathematical terms which are repeated within the equations 5 to 8.

Equation

$$5 \quad i_j = \left(\sum_{k=(j-1)x+1}^{jx} (\phi_k) - \sum_{k=jx+1}^{(j+1)x} (\phi_k) + B + \left(\frac{R_{p,(j+1)}}{2} + \frac{R_{n,(j+1)}}{2} \right) \cdot \left(\sum_{k=j+1}^y (i_k) - \sum_{k=1}^{j-1} (i_k) \right) \right) \cdot F^{-1}$$

$$6 \quad i_j = \left(\sum_{k=(j-1)x+1}^{jx} (\phi_k) - \sum_{k=(j-2)x+1}^{(j-1)x} (\phi_k) + A + \left(\frac{R_{p,j}}{2} + \frac{R_{n,j}}{2} \right) \cdot \left(\sum_{k=1}^{j-1} (i_k) - \sum_{k=j+1}^y (i_k) \right) \right) \cdot G^{-1}$$

$$7 \quad i_j = \left(\sum_{k=(j-1)x+1}^{jx} (\phi_k) - \sum_{k=jx+1}^{(j+1)x} (\phi_k) + B - (R_{p,(j+1)} + R_{n,(j+1)}) \cdot \sum_{k=1}^{j-1} (i_k) \right) \cdot D^{-1}$$

$$8 \quad i_j = \left(\sum_{k=(j-1)x+1}^{jx} (\phi_k) - \sum_{k=(j-2)x+1}^{(j-1)x} (\phi_k) + A - (R_{p,j} + R_{n,j}) \cdot \sum_{k=j+1}^y (i_k) \right) \cdot E^{-1}$$

$$A \quad \sum_{\substack{k=(j-2)x+1 \\ y>1}}^{(j-1)x} (R_{wsp,k} + R_{wsn,k}) \cdot i_{(j-1)} + \sum_{\substack{k=(j-2)x+1 \\ x>1 \\ y>1}}^{(j-1)x-1} (R_{\text{conn},(k)(k+1)}) \cdot i_{(j-1)}$$

$$B \quad \sum_{\substack{k=jx+1 \\ y>1}}^{(j+1)x} (R_{wsp,k} + R_{wsn,k}) \cdot i_{(j+1)} + \sum_{\substack{k=jx+1 \\ x>1 \\ y>1}}^{(j+1)x-1} (R_{\text{conn},(k)(k+1)}) \cdot i_{(j+1)}$$

$$C \quad \sum_{k=(j-1)x+1}^{jx} (R_{wsp,k} + R_{wsn,k}) + \sum_{\substack{k=(j-1)x+1 \\ x>1}}^{jx-1} (R_{\text{conn},(k)(k+1)})$$

$$D \quad (R_{p,(j+1)} + R_{n,(j+1)}) + C$$

$$E \quad (R_{p,j} + R_{n,j}) + C$$

$$F \quad \left(\frac{R_{p,(j+1)}}{2} + \frac{R_{n,(j+1)}}{2} \right) + C$$

$$G \quad \left(\frac{R_{p,j}}{2} + \frac{R_{n,j}}{2} \right) + C$$

the string $i_{n,j}$ and is therefore termed i_j (compare Equation 5.16). Furthermore, based on Kirchhoff's first law, Equation 5.18 holds true for every parallel connected string $j \in [1, y]$. Based on the second law of Kirchhoff, the enclosed network equation can be derived considering the mesh between two adjacent strings and generalised for any number of y parallel connected strings. As for the yP pure parallel topology, the position of the respective string relative to the ST must be considered for the $xSyP$ topology. The respective flow charts for ST_{side} and ST_{mid} are depicted in Figure 5.4(c) and the associated equations are given in Tables 5.1 and 5.2. Note, that interconnections between multiple parallel strings are only considered at the top and bottom and not in the middle of the strings.

5.2.4 Model coupling

The PCM and the THM of the single cell model are coupled bidirectionally. The generated heat q_{gen} is integrated over the three domains of the PCM (negative electrode, separator and positive electrode) and results in Q_{gen} . This value is coupled into the THM as a heat source. The temperature of the cell T_{cell} evolves during operation due to generated Q_{gen} , stored Q_{stored} and dissipated heat Q_{diss} (all averaged over the cell volume) according to the 0D energy balance equation in the THM. This adapted temperature is sequentially coupled back to the PCM. Different physicochemical parameters are implemented being temperature dependent. Thus, they adjust according to a temperature increase or decrease. The transport properties of the electrolyte D_1 , κ_1 and $\frac{\partial \ln f_{\pm}}{\partial \ln c_1}$ are described in dependency of lithium concentration c_1 and temperature T_{cell} according to Valøen et al. [70] (compare Chapter 3.4.4 Equations 3.20 to 3.22). The diffusivity and reaction rate in the electrodes are assumed to follow a temperature dependent Arrhenius behaviour according to Guo et al. [65; 71] (compare Chapter 3.4.4 Equations 3.23 and 3.24).

Regarding the coupling between PCM and ELM, two coupling relevant variables are calculated in each time step within the PCM of each cell. The cell potential difference of the solid phase between positive and negative cell pole ϕ_s and the electrode current density i_{ns} , which is normal to the 1D interval. The two respective variables of all connected cells $i \in [1, x \cdot y]$ are passed to the ELM.

The ELM requires the total battery system current i_{app} as input for calculating the respective string currents. This system current is provided by the Operation model part (compare yellow box in Figure 5.2). Any desired current profile can be chosen according to the study focus. The ELM calculates the string currents i_j for every j th string from the equations in Table 5.1 or Table 5.2 respectively. For each of the cells within a string j the cell currents equal the string current. These cell currents are used within the PCM for calculating the potential boundary condition at the negative cell pole $\phi_{si}|_{x_{\text{stack}}=0}$. x_{stack} denotes the x -coordinate of the PCM interval (compare Figure 3.1). $x_{\text{stack}} = 0$ denotes the interval boundary at the anode of the PCM cell stack, $x_{\text{stack}} = x_{\text{max}}$ denotes the interval boundary at the cathode of the PCM cell stack.

Within the model, the following equations are used for each i th of the x serial connected cells:

$$\phi_{si}|_{x_{\text{stack}}=0} = 0 \text{ V} \quad (5.20)$$

$$j_{\text{nsi}}|_{x_{\text{stack}}=x_{\text{max}}} = \frac{i_{\text{app}}}{A_{\text{electrode}}} \quad (5.21)$$

The respective potential differences of the serial connected cells ϕ_1 and ϕ_2 (for a 2S system), are added up to a string potential ϕ_j during each time step while subtracting the potential drops which occur at the respective cell connector (R_p , R_n) and welding spot (R_{wsp} , R_{wsn}) resistances within the string.

For a pure parallel connection of y cells, the equations for calculating the respective cell potential at the negative cell pole vary according to the position of the cell respective to the ST. This is also true for a combined connection of x serial and y parallel cells. In both cases, it has to be distinguished, in which of the parallel strings $j \in [1, y]$ the respective cell i is located and whether this string j is located left or right of ST_{side} or ST_{mid} . The equations for $\phi_{si}|_{x_{stack}=0}$ are given in Table 5.3, where o denotes the number of strings in between string j and the ST. Note, that the equations which are given for $xSyP$ systems can also be used for $1SyP$ systems. For the applied current density to the respective cell's PCM, the string currents i_j with $j \in [1, y]$ are used:

$$j_{nsi}|_{x_{stack}=x_{max}} = \frac{i_j}{A_{electrode}} \quad (5.22)$$

The electric coupling is established. The general PCM-ELM coupling equations are summarised in Table 5.3.

5.2.5 Validation and parametrisation

The cell used for parametrisation of the model and the following investigations is the cell introduced in Chapter 3.2. For further nominal data of the investigated cell, see Table 3.1. In order to parametrise the single cell model, one single cell has been subjected to two measurement routines in a thermal test bench at $T_{amb} = 25^\circ\text{C}$ and $v_{air} = 1\text{ m s}^{-1}$: (Part 1) Cooling tests: CC pulse profiles, followed by an OC period and (Part 2) C-Rate tests: CC discharge tests at different C-Rates. For a detailed description of the custom made thermal test bench, please refer to Rheinfeld et al. [121].

Within the thermal test bench, an air flow with a predefined velocity can be set. Using this velocity, the convective heat transfer coefficient, which occurs at the investigated cell can be calculated (compare Chapter 3.5.3.1). The heat capacity of a cell can be calculated using the masses and heat capacities of the individual cell components [93]. The component masses have been measured, the component heat capacities have been taken from Chen et al. [94] and Guo et al. [98]. The calculated heat capacity of the investigated cell is $1300\text{ J kg}^{-1}\text{ K}^{-1}$ (compare Chapter 3.5.2). This value can be used for a first simulation. The thermal parameter fitting has been performed as described by Zhang et al. [74]. Using the calculated heat transfer coefficient, the heat capacity of the cell can be adapted within the simulation until experimental and simulated data coincide. The final value used during the simulations in this study is $1400\text{ J kg}^{-1}\text{ K}^{-1}$. This heat capacity value needs to hold true for both, the cooling tests and the rating tests.

In the first part, the cell temperature has internally been increased by pulsing the cell using different CC pulse profiles until the cell reached a thermally steady state. The periodic pulse profiles have been designed using short current pulses in a way, that the mean *SOC* of the cell has not been changed during operation.

- 1Cch-2Cdch: CC charge $I_{ch,CC} = 1\text{ C} = 3\text{ A}$ for $t = 2\text{ s}$ followed by a CC discharge $I_{dch,CC} = 2\text{ C} = 6\text{ A}$ for $t = 1\text{ s}$ (period $\tau = 3\text{ s}$).

Table 5.3: General coupling equations between ELM and PCM for different topologies of x serial and y parallel connected cells. j denotes the number of that parallel connected string where the cell i is located. o denotes the number of strings in between string j and the ST. For a pure parallel connection, the equations for $xSyP$ can be used with $x = 1$.

Topology	$j_{nsi} _{x_{stack}=x_{max}}$	$\phi_{si} _{x_{stack}=0}$
xS	$\frac{i_{app}}{A_{electrode}}$	0 V
$xSyP$	$\frac{-i_j}{A_{electrode}}$	<p>if string j is right of ST_{mid}:</p> $-\frac{R_{n,(j-o)}}{2} \cdot \sum_{k=j-o}^j (i_k) - \sum_{k=j-o+1}^j \left(R_{n,k} \cdot \sum_{l=k}^j (i_l) \right) - A$ <p>if string j is left of ST_{mid}:</p> $-\frac{R_{n,(j+o)}}{2} \cdot \sum_{k=j}^{j+o-1} (i_k) - \sum_{k=j+1}^{j+o-1} \left(R_{n,k} \cdot \sum_{l=j}^k (i_l) \right) - A$ <p>if string j is right of ST_{side}:</p> $-\sum_{k=1}^j \left(R_{n,k} \cdot \sum_{l=k}^j (i_l) \right) - A$ <p>if string j is left of ST_{side}:</p> $-\sum_{k=j+1}^{j+o+1} \left(R_{n,k} \cdot \sum_{l=j}^{k-1} (i_l) \right) - A$
A		$i_j \cdot \left(R_{wsn,i} + \sum_{k=1}^{jx-i} (R_{wsp,(i+k)} + R_{conn,(i)(i+k)} + R_{wsn,(i+k)}) \right) - \sum_{k=1}^{jx-i} (\phi_{(i+k)})$

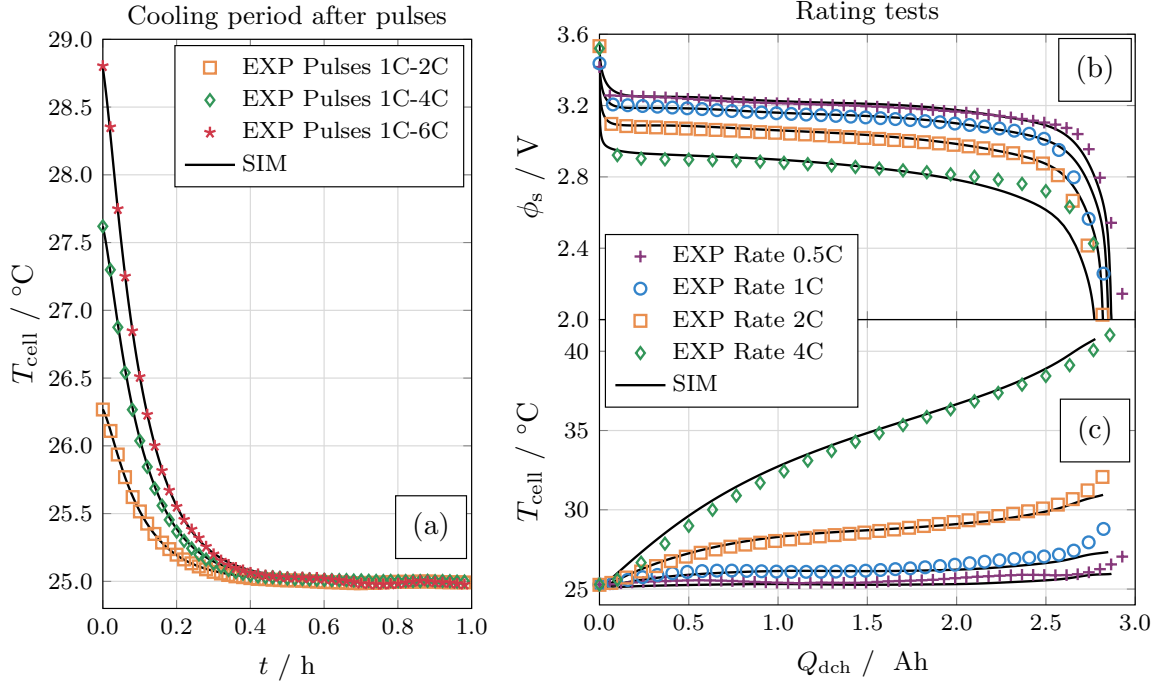


Figure 5.5: Validation of the single cell model at $T_{\text{amb}} = 25^\circ\text{C}$ and $v_{\text{air}} = 1 \text{ m s}^{-1}$ under (a) thermally steady conditions during an OC period for the cell temperature T_{cell} and under rating tests for (b) cell potential ϕ_s and (c) cell temperature T_{cell} . The resulting model parameters are given in Table 5.4 and Table 5.5.

- 1Cch-4Cdch: CC charge $I_{\text{ch,CC}} = 1 \text{ C} = 3 \text{ A}$ for $t = 4 \text{ s}$ followed by a CC discharge $I_{\text{dch,CC}} = 4 \text{ C} = 12 \text{ A}$ for $t = 1 \text{ s}$ (period $\tau = 5 \text{ s}$).
- 1Cch-6Cdch: CC charge $I_{\text{ch,CC}} = 1 \text{ C} = 3 \text{ A}$ for $t = 6 \text{ s}$ followed by a CC discharge $I_{\text{dch,CC}} = 6 \text{ C} = 18 \text{ A}$ for $t = 1 \text{ s}$ (period $\tau = 7 \text{ s}$).

After the thermally stationary state had been reached, the respective pulse profile was followed by an OC phase of $t = 1 \text{ h}$. During this OC phase the cell was cooled due to the forced air convection applied in the thermal test bench at the given air velocity v_{air} . The thermal parameter fitting has been performed during these cooling periods. The resulting comparison between the respective measured and simulated cooling phases for $v_{\text{air}} = 1 \text{ m s}^{-1}$ is depicted in Figure 5.5(a).

In the second part, the model has been parametrised regarding the cell behaviour under CC discharge at different C-Rates. The resulting comparison between measurement and simulation curves for both, cell potential and cell temperature, are shown in Figure 5.5(b) and (c) respectively. The resulting model parameters are summarised in Table 5.4 and Table 5.5. The implemented OCV curves, entropic coefficients as well as tortuosity relationships are given in Chapter 3.4.4.

Within the PCM, only the electrodes and separator but not the current collectors are modelled (compare Figure 3.1). During parametrisation, deviations might occur regarding the measured and simulated overpotentials. As already mentioned in Section 5.1.2, Reimers [118] has introduced a method to analytically account for the additional impedances of the current collectors which contribute to the overall impedance of a cell. He developed an equation to calculate this impedance R_{foil} dependent on the respective tab arrangement of the electrode stack design. The investigated cell has a three tab design. The negative current collector has two tabs at the outermost positions of the electrode stack.

Table 5.4: Physicochemical model parameters for the porous electrode and separator domain at $T_{\text{amb}} = 25^\circ\text{C}$ and $v_{\text{Air}} = 1\text{ m s}^{-1}$. Exponent glossary: e —estimated, m —measured. The analytical equations are given in Chapter 3.4.4.

Parameter	Negative Electrode (Li_xC_6)	Separator	Positive Electrode (Li_yFePO_4)
Geometry			
Electrode length $x_{\text{electrode}}$	140 cm ^m		140 cm ^m
Electrode height $y_{\text{electrode}}$	5.6 cm ^m		5.6 cm ^m
Electrode area (double coated) $A_{\text{electrode}}$	0.1568 m ^{2m}	0.1568 m ^{2m}	0.1568 m ^{2m}
Electrode thickness $t_{\text{electrode}}$	61 μm^m	18 μm^m	79 μm^m
Particle radius r_p	3.5 μm^m		0.05 μm^m
Electrode active material volume fraction ϵ_s	0.46 ^e	0.50 ^e	0.48 ^e
Electrode porosity ϵ_l	0.30 ^e		0.30 ^e
Active specific surface area a_v	$\frac{3\epsilon_s}{r_p}$		$\frac{3\epsilon_s}{r_p}$
Tortuosity τ	$(4.7 \cdot \epsilon_{l,\text{neg}}^{-0.1})^{-1}$ [69]	$(1.0 \cdot \epsilon_{l,\text{sep}}^{-2.5})^{-1}$ [69]	$(3.1 \cdot \epsilon_{l,\text{pos}}^{-0.6})^{-1}$ [69]
Thermodynamics			
Equilibrium voltage E_{eq}	$f(x)$ (Eqn. 3.8)[64]		$f(y)$ (Eqn. 3.9)[64]
Entropic coefficient $\frac{dE_{\text{eq}}}{dT}$	$f(x)$ (Eqn. 3.10)[65]		$f(y)$ (Eqn. 3.11)[66]
Maximum lithium concentration $c_{s,\text{max}}$	31.370 mol m ⁻³ [64]		22.806 mol m ⁻³ [64]
Initial state of charge $\frac{c_{s,0}}{c_{s,\text{max}}}$	0.78 ^e		0.02 ^e
Kinetics			
Reaction rate reference k_{ref}	$0.3 \times 10^{-11} \text{ m s}^{-1e}$		$0.3 \times 10^{-11} \text{ m s}^{-1e}$
Activation energy for reaction $E_{a,k}$	$3 \times 10^4 \text{ J mol}^{-1}$ [71]		$3 \times 10^4 \text{ J mol}^{-1}$ [71]
Anodic charge-transfer coefficient α_a	0.5[127]		0.5[127]
Cathodic charge-transfer coefficient α_c	0.5[127]		0.5[127]
Transport			
Solid diffusivity (reference) $D_{s,\text{ref}}$	$2 \times 10^{-14} \text{ m}^2 \text{ s}^{-1}$ [64]		$1.18 \times 10^{-18} \text{ m}^2 \text{ s}^{-1}$ [64]
Activation energy for diffusion E_a, D_s	$2 \times 10^4 \text{ J mol}^{-1}$ [71]		$4 \times 10^5 \text{ J mol}^{-1}$ [71]
Solid electric conductivity σ_s	100 S m ⁻¹ [128]		0.1 S m ⁻¹ [129]
Parameter			
Liquid Phase			
Electrolyte diffusivity D_l		$f(c_l, T)$ (Eqn. 3.20)[70]	
Electrolyte ionic conductivity κ_l		$f(c_l, T)$ (Eqn. 3.21)[70]	
Activity dependency $\frac{\partial \ln \gamma_{\pm}}{\partial \ln c_l}$		$f(c_l, T)$ (Eqn. 3.22)[70]	
Transport number t_+		0.38[70]	
Parameter			
Negative current collector (Cu)		Positive current collector (Al)	
Current collector length x_{coll}	140 cm		140 cm
Current collector width y_{coll}	5.6 cm		5.6 cm
Current collector thickness (single coated) t_{coll}	5.5 μm		7.5 μm
Current collector material resistivity ρ_{coll}	$1.72 \times 10^{-2} \Omega \text{ mm}^2 \text{ m}^{-1}$		$2.65 \times 10^{-2} \Omega \text{ mm}^2 \text{ m}^{-1}$
Current collector specific electrical resistance R_{coll}	$27.8 \text{ m}\Omega \text{ m}^{-1}$		$31.5 \text{ m}\Omega \text{ m}^{-1}$

Table 5.5: Geometric, electric and thermal model parameters for the cylindrical cell (multiple materials), cell connector (Hilumin - nickel plated steel) and welding spot joints (between cell pole and cell connector), when the distance between two adjacent cells is $dx_{\text{cell}} = 5 \text{ mm}$. The values are chosen for $T_{\text{amb}} = 25 \text{ }^\circ\text{C}$ and $v_{\text{Air}} = 1 \text{ m s}^{-1}$. Exponent glossary: f=fitted, e=estimated, m=measured, c=calculated.

Parameter	Value
Cell	
Radius r_{cell}	$26.2 \pm 0.2 \text{ mm}$
Height h_{cell}	$65.4 \pm 0.2 \text{ mm}$
Specific heat capacity $c_{\text{p,cell}}$	$1400 \text{ J kg}^{-1} \text{ K}^{-1\text{f}}$
Convective heat transfer coefficient h_{conv}	$22.5 \text{ W m}^{-2} \text{ K}^{-1\text{c}}$
Cell connector	
Length l_{conn}	$4.5 \text{ cm}^{\text{m}}$
Width w_{conn}	1 cm^{m}
Thickness t_{conn}	$0.5 \text{ mm}^{\text{m}}$
Electric conductivity σ_{conn}	$9.93 \times 10^6 \text{ S m}^{-1[126]}$
Electric resistance $R_{\text{conn}} = R_{\text{p}} = R_{\text{n}}$	$9 \times 10^{-4} \text{ } \Omega^{\text{c}}$
Density ρ_{conn}	$7.87 \text{ g cm}^{-3[126]}$
Specific heat capacity $c_{\text{p,conn}}$	$452 \text{ J kg}^{-1} \text{ K}^{-1\text{e}}$
Electric resistance spot-welded joint R_{ws}	$0.2 \text{ m}\Omega^{[130]}$
Thermal resistance spot-welded joint $R_{\text{th,ws}}$	$1 \times 10^{-5} \text{ m}^2 \text{ K W}^{-1[131]}$

The positive current collector has one tab in the middle of the electrode stack. Due to the three tab design the respective impedance calculates to

$$R_{\text{foil}} = \frac{1}{12} x_{\text{electrode}} (R_{\text{coll,neg}} + R_{\text{coll,pos}}) = 6.9 \text{ m}\Omega \quad (5.23)$$

Here, $x_{\text{electrode}} = 140 \text{ cm}$ is the length of the electrode stack. $R_{\text{coll,neg}}$ (Ω) and $R_{\text{coll,pos}}$ (Ω) are the specific electrical resistances of the respective current collectors. The foil resistance which is fitted during parametrisation of the single cell model is $R_{\text{foil}} = 8 \text{ m}\Omega$. The fitted value is a little higher than the calculated value due to the additional internal contact resistances within in the cell.

5.3 Inhomogeneous current distribution due to cell-to-cell variations

In a first step, the influence of cell-to-cell variations on the inhomogeneity of current distribution within a 2P module under different ST contact positions is investigated at 1C. A 1C discharge of the system corresponds to a system current of $i_{\text{app}} = -6 \text{ A}$. The intention is to discharge each of the cells by a cell current of $i_1 = i_2 = -3 \text{ A}$, which again corresponds to a 1C discharge on cell level. Furthermore, the resulting difference in Ah-throughput between the connected cells is discussed and the influence of the applied *C-Rate* on the inhomogeneous current distribution is investigated. Based on the results, implications for assembling battery modules are derived. During the following investigations it is assumed, that the two cells are connected in parallel instantaneously in the moment, the simulation starts. Thus, the initial condition is ($t = 0$; $DOD = 0$). This means, that the cells have not been able to balance over the parallel connection prior to the start of discharge.

5.3.1 Influence of the system terminal position

In order to examine the influence of cell-to-cell variations on the current distribution within a system of parallel connected cells, a 2P module is investigated, which is contacted differently. In case (a), the module is contacted at ST_{mid} , with symmetric cell connectors in between cell 1 and cell 2. In case (b) and (c), the module is contacted asymmetrically at ST_{side} , with cell 1 being located closer to the ST than cell 2. The modules are subjected to different parametric gradients.

Figure 5.6 shows the resulting current distribution during a 1C discharge over the respective system's DOD. The left hand side of the figure shows the schematic ECMs of the systems and relates the positions of the cells to the used line types according to the cell shading. The currents within the homogeneous system are displayed by grey lines. When inhomogeneities are induced, the solid shaded cell has a smaller capacity, a higher impedance or a lower initial temperature than the dashed shaded cell. The main part of the figure shows the current distribution due to a dC (purple lines), dR (green lines) and dT (orange lines) inhomogeneity respectively. The dots mark the maximum observed peak currents.

In all cases except for connected homogeneous cells under a ST_{mid} contacting (compare case (a)), the cells show an inhomogeneous current distribution. Each of the systems is discharged with a 1C system current, which should lead to a discharge current of 1C per cell. Due to the cell-to-cell inhomogeneity, the currents of the two cells are not equal but symmetric around the applied *C-Rate* per cell ($=1C$).

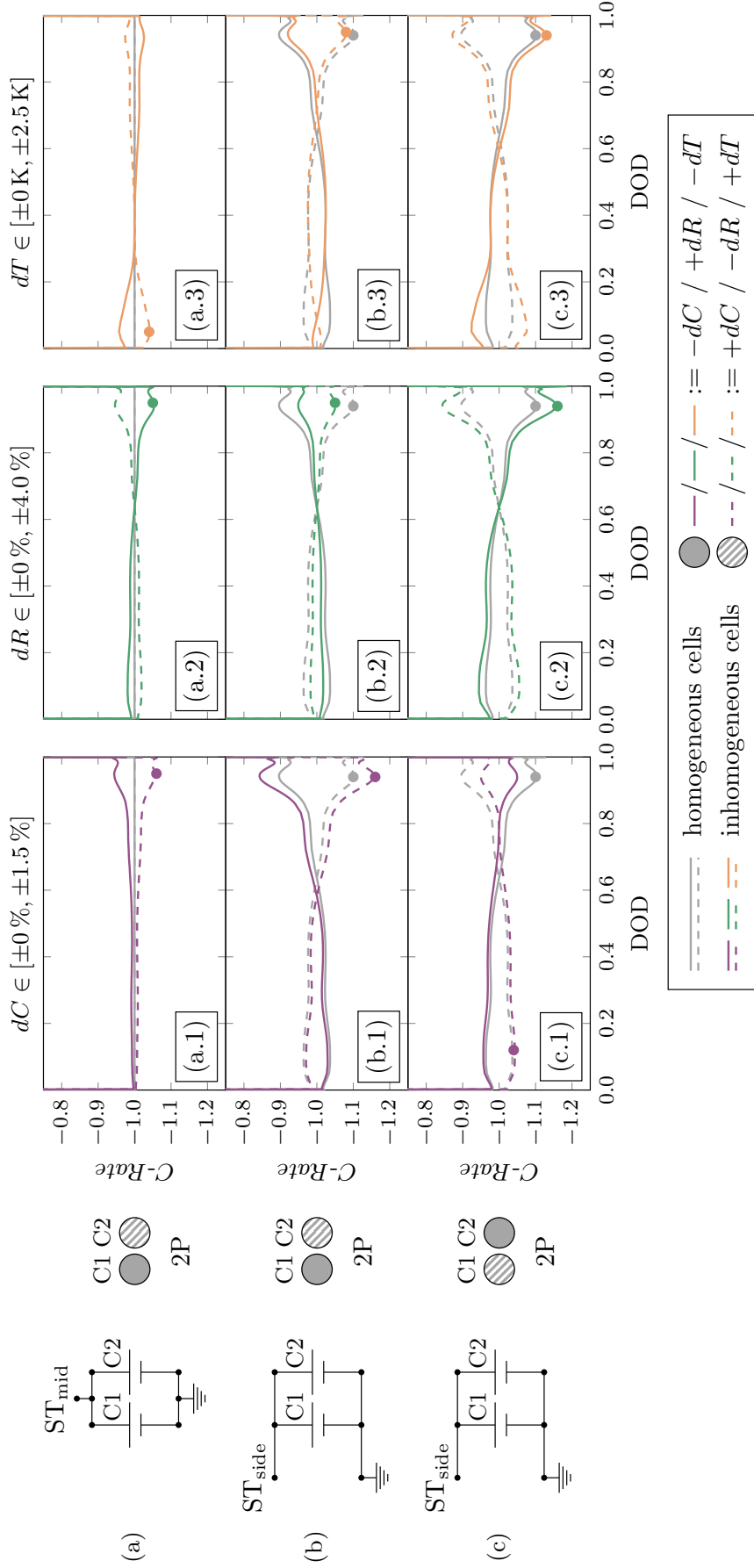


Figure 5.6: Current distribution during a 1C discharge scenario within the connected cells of a 2P module, which is contacted at ST_{mid} (case (a)) or ST_{side} (case (b) and case (c)) and which is subjected to differently induced inhomogeneity. The left hand side of the figure shows the schematic ECMs of the systems and relates the positions of the cells to the used line types according to the cell shading. The currents within the homogeneous system are displayed by solid lines. When inhomogeneities are induced, the solid shaded cell has a smaller capacity, a higher impedance or a lower initial temperature than the dashed shaded cell. The main part of the figure shows the current distribution due to a dC (purple lines), dR (green lines) and dT (orange lines) inhomogeneity respectively. The dots mark the maximum observed peak currents.

A $1C$ cell current is only reached for homogeneous cells which are contacted at ST_{mid} (compare (a.1)). When inhomogeneous cells are connected, in all cases except for (a.1), a turning point (TP) of the two currents can be observed during the discharge of the system. The cell which has delivered a higher current before the TP, delivers a smaller current afterwards and vice versa. The current distribution between the two connected cells depends on the ratio between their respective sum of contributions to the string's electric potential versus electric ground. These contributions are on the one hand the influence of the cell's OCV as well as the internal polarisation of the cell during operation. On the other hand also the external polarisation due to the cell interconnection resistances contributes to a string's electric potential. At the TP, the sums of these contributions to the electric potential of the two parallel connected strings are equal. Therefore, the currents through the two strings are equal at the TP. Towards the end of discharge (EOD) of the system, the two currents first diverge and then subsequently converge again. The divergence occurs when the limiting cell reaches its EOD. Then its internal polarisation increases, the cell cannot deliver the required current any more and the remaining cell must therefore deliver an even higher current. Finally, also this second cell cannot deliver this high current any more, the two currents converge again and the EOD of the system is reached.

The inhomogeneity observed in case (a) is enhanced when the cells are contacted asymmetrically (compare case (b) and (c)). In these cases, also the influence of the asymmetric current collector design is present. The coloured curves within cases (b) and (c) can therefore be considered the sum of the grey lines for that specific case and the coloured curves of case (a) to account for the respective additional cell-to-cell variation.

2P module contacted at ST_{mid} Under a dC cell-to-cell variation, one cell (cell 1 in (a.1) and (b.1)) is attributed a smaller amount of active material within the negative electrode $\varepsilon_{s,neg}$. This decreases the active specific surface area a_v , which influences the local current source i_v . A higher absolute internal polarisation $|\eta_1|$ results in a smaller absolute discharge current $|i_1|$. In order to be able to provide the required system current i_{app} , cell 2 is discharged with a higher absolute discharge current $|i_2| > |i_1|$. Within a module which is contacted at ST_{mid} (compare Figure 5.6 (a.1)), this results in cell 1 being discharged less than cell 2 throughout the whole discharge period.

A dR variation between the two cells with cell 1 being attributed a higher R_{foil} than cell 2 (compare Figure 5.6 (a.2)) results in a higher internal polarisation $|\eta_1|$ and therefore an initially smaller discharge current $|i_1|$ through cell 1. At the TP, the sums of the contributing parts to the electric potential of the strings are equal, after which cell 1 is discharged more than cell 2 until the EOD.

Under a dT variation (compare Figure 5.6 (a.3)), a smaller cell temperature T_{ref1} results in a worse lithium diffusivity within the electrode active materials and a both, a worse lithium diffusivity and a smaller ionic conductivity within the electrolyte [17], which therefore leads to a higher polarisation $|\eta_1|$ and thus to a smaller discharge current $|i_1|$. After the TP, the discharge current through cell 1 exceeds the one through cell 2.

2P module contacted at ST_{side} When the system is contacted at ST_{side} , even when homogeneous cells are connected, different currents through the parallel connected strings are observed (compare grey lines in Figure 5.6 cases (b) and (c)). This is due to the fact that although the cell connector resistances are constant in the simulation, the cells experience different voltage drops relative to the asymmetric ST. (R_{p1}, R_{n1}) are exposed to both cell currents $(i_1 + i_2)$ whereas (R_{p2}, R_{n2}) are only passed through by i_2 . Cell 2 is subjected to a higher external polarisation versus electric ground than

cell 1. These ohmic polarisations evoke a current distribution within the module which is independent of the induced cell-to-cell variations following the same principle as the current density distribution within single cells [92; 121–124]. The different string currents lead to a difference within the internal polarisations of the cells, cells' SOC's and OCV's. At the respective TP, this difference equals the difference within the external voltage drops which leads to the string currents being equal at this point. Note, that the grey lines for the homogeneous system are the same for case (b) and case (c). Depending on whether the 'bad' cell is situated closer to the ST (compare case (b)) or the 'good' cell is (compare case (c)), the inhomogeneity within the system increases or decreases according to the interaction between the effects of the cell-to-cell variation and the asymmetric ST.

A dC variation leads to a more homogeneous current distribution if the cell with the higher capacity is assembled closer to the ST (compare purple lines in Figure 5.6 (c.1)). In this case, also smaller peak currents are observed. The increased $\varepsilon_{s,neg,1}$ results in a smaller absolute polarisation $|\eta_1|$, which initially further increases the already larger absolute current through cell 1 due to the asymmetric connection $|i_1| > |i_2|$. This higher current increases the internal polarisation $|\eta_1|$, which works against the influence of the higher external resistances which are seen by cell 2. Therefore, the current deviation towards the EOD and the peak currents are reduced. Over the whole discharge period, the current distribution is more homogeneous.

In order to reach a more homogeneous current distribution under an induced dR variation, the cell with the higher impedance should be assembled closer to the ST (compare green lines in Figure 5.6 (b.2)). The difference within the internal polarisations works against the difference in the external potential drops. Therefore, in the beginning of the discharge, cell 2 is discharged less than cell 1 and the current deviation is smaller than for the homogeneous system. Towards the EOD of the system, cell 1 shows a smaller absolute internal polarisation, which results in a larger absolute discharge current $|i_1|$ compared to the homogeneous system. Therefore, the current deviation between the cells after the TP is still smaller than for the homogeneous system.

When the module is subjected to a thermal gradient dT , the current distribution is more homogeneous when the cell with the lower ambient temperature is assembled closer to the ST (compare orange lines in Figure 5.6 (b.3)). Due to the smaller cell temperature T_{ref1} , the internal polarisation $|\eta_1|$ is increased and works against the influence of the asymmetric ST contact. This not only results in a smaller current deviation between the cells but also in smaller peak currents within the system.

The observed maximum peak currents per cell within the different systems differ dependent on the ST position, the induced variations and the position of the 'good' and 'bad' cell relative to the ST (compare dot marks in Figure 5.6). For case (a) the absolute peak currents lie by 6% (dC), 5% (dR), and 4% (dT) above the intended C -Rate of $1C$. For a connection at ST_{side} (cases (b) and (c)), even for homogeneous connected cells, the peak currents exceed $1C$ by 10%. With the 'bad' cell being situated close to the ST (compare Figure 5.6 case (b)) the observed maximum peak currents per system change to 16% (dC), 5% (dR), and 8% (dT) above $1C$. With the 'good' cell being situated close to the ST (compare Figure 5.6 case (c)) the observed maximum peak currents per system change to 4% (dC), 16% (dR), and 13% (dT) above $1C$. Therefore, the peak currents within an asymmetrically contacted module can be lowered, if the cell with the higher capacity, higher impedance or lower ambient temperature is situated close to the ST.

5.3.2 Impact on the Ah-throughput

Figure 5.7 shows the resulting cumulated Ah-throughput Ah_{cell} through the parallel connected cells within a 2P module during a 1C discharge. The values correspond to the same investigation as shown in Figure 5.6 under the same induced dC , dR and dT variations. As the Ah differences between the two cells are not easy to identify in Figure 5.7, Figure 5.8 depicts the corresponding absolute difference in Ah between the two cells $|\Delta Ah_{\text{cell}}| = |Ah_{\text{cell1}} - Ah_{\text{cell2}}|$. Homogeneous cells are depicted by grey lines, inhomogeneous cells are depicted by coloured dotted (for case (b) in Figure 5.6) or dashed (for cases (a) and (c) in Figure 5.6) lines.

For an ST_{mid} connection, the Ah difference between the two connected cells increases under a dC variation towards the EOD. This is due to the fact that no TP of the cell currents is present in this case (compare Figure 5.6 (a.1)). Under a dR and dT variation, the Ah difference increases first and then decreases again. It is maximum at the respective TP (compare Figure 5.6 (a.2) and (a.3)).

As the more interesting results correspond to the ST_{side} -connection, the respective graphs are concentrated in Figure 5.9. Note, that within Figure 5.9, the lines corresponding to inhomogeneous cells in Figure 5.7 and 5.8 are depicted by dotted lines for case (b) and by dashed lines for case (c).

Figure 5.9 (a) to (c) show that the Ah which are put through the individual cells diverge during the discharge regime but converge again towards the EOD except for a dC variation under a case (b) assembly. Figure 5.9 (d) to (f) show the absolute difference in Ah-throughput between the two cells $|\Delta Ah_{\text{cell}}| = |Ah_{\text{cell1}} - Ah_{\text{cell2}}|$. For a dC variation under a case (b) assembly (compare dotted line in Figure 5.9 (d)), the Ah-difference increases towards the EOD. This is due to the fact that the absolute Ah-difference is depicted, wherefore a negative difference is displayed as a positive value. Thus, the Ah-difference at the EOD between the two cells is negative for a case (b) assembly and positive for a case (c) assembly under a dC variation. For a dR and dT variation, the Ah-difference vanishes towards the EOD. The maximum deviation in Ah between the connected cells emerges at the respective TP of the two cell currents (compare Figure 5.6 case (b) and case (c)). These maxima correspond to about 4% of the rated capacity of the cell $C_{\text{rated}} = 3 \text{ Ah}$, which is high compared to reported values by Erhard et al. [123] and Kosch et al. [124]. This is due to the fact that the cell investigated here is an LFP cell with a very flat OCV which does not allow for a OCV gradient driven balancing between the cells. The other investigated cell was a NMC cell which has a steeper OCV, which therefore allows for a balancing as soon as a SOC difference is present [123; 124]. The maximum deviation in Ah between the connected cells is smaller, if the cell with a lower capacity or higher impedance is assembled close to the ST. This is a different cell matching recommendation than when aiming to reduce peak currents within the system. So different optimization scenarios ask for different cell matching recommendations. Exposing the ST to the smaller ambient temperature on the other hand will reduce both, the Ah difference as well as the peak currents within the system.

Regarding the presented results, in case the discharge of the system was stopped right before the TP of the cell currents, the deviation between the individual Ah_{cell} is maximum. If this partial discharge was directly followed by a CC-charge (CH), the deviation between the individual Ah_{cell} will adapt further. Therefore, cycling a system of inhomogeneous parallel connected cells will not only lead to the individual cells experiencing different current rates but might also result in differently aged cells within the module over operation time.

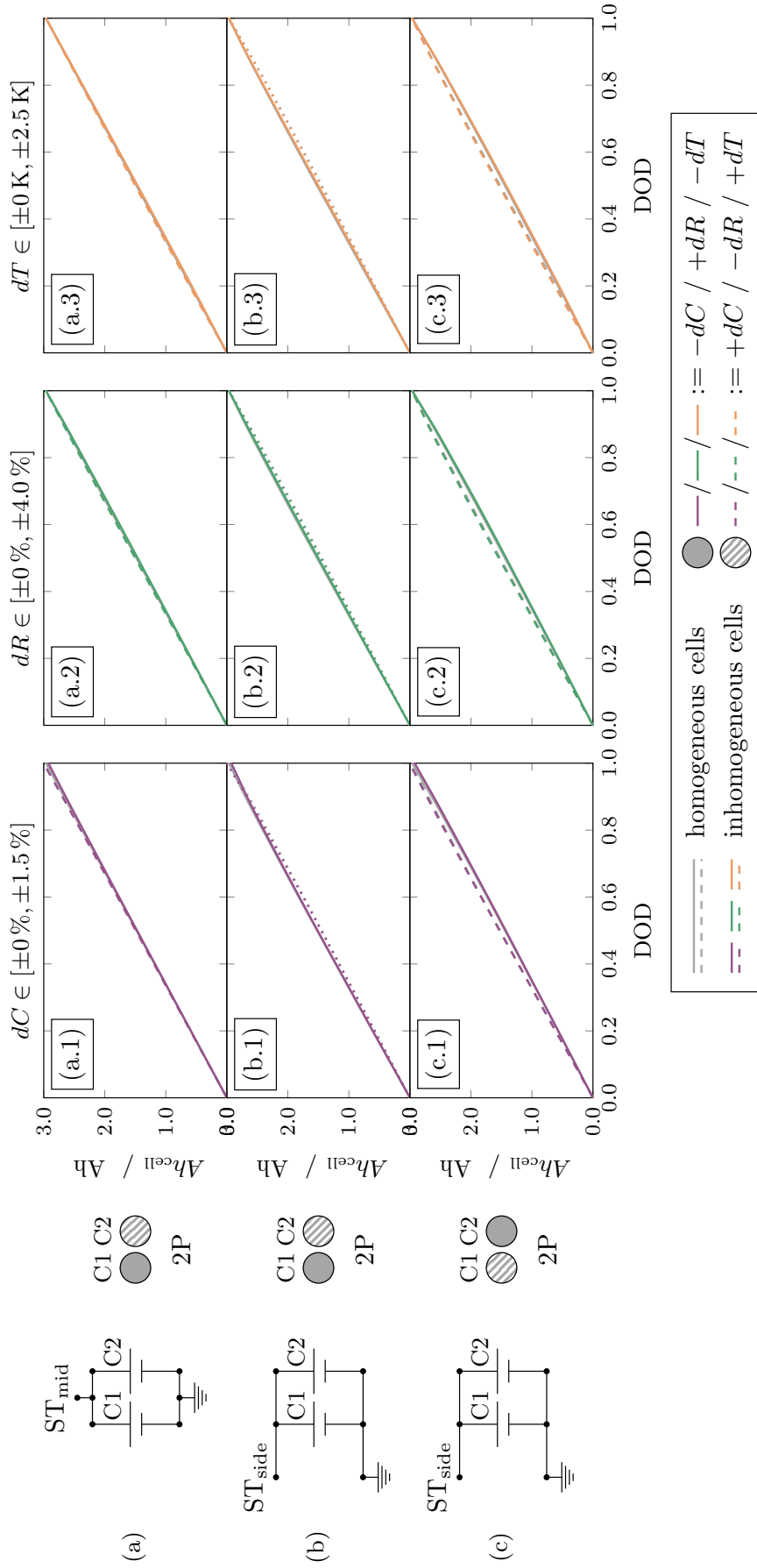


Figure 5.7: Cumulated Al-throughput Ah_{cell} through the parallel connected cells within a 2P module during a 1C discharge. Homogeneous cells are depicted by grey lines, inhomogeneous cells are depicted by coloured dotted (for case (b) in Figure 5.6) or dashed (for cases (a) and (c) in Figure 5.6) lines.

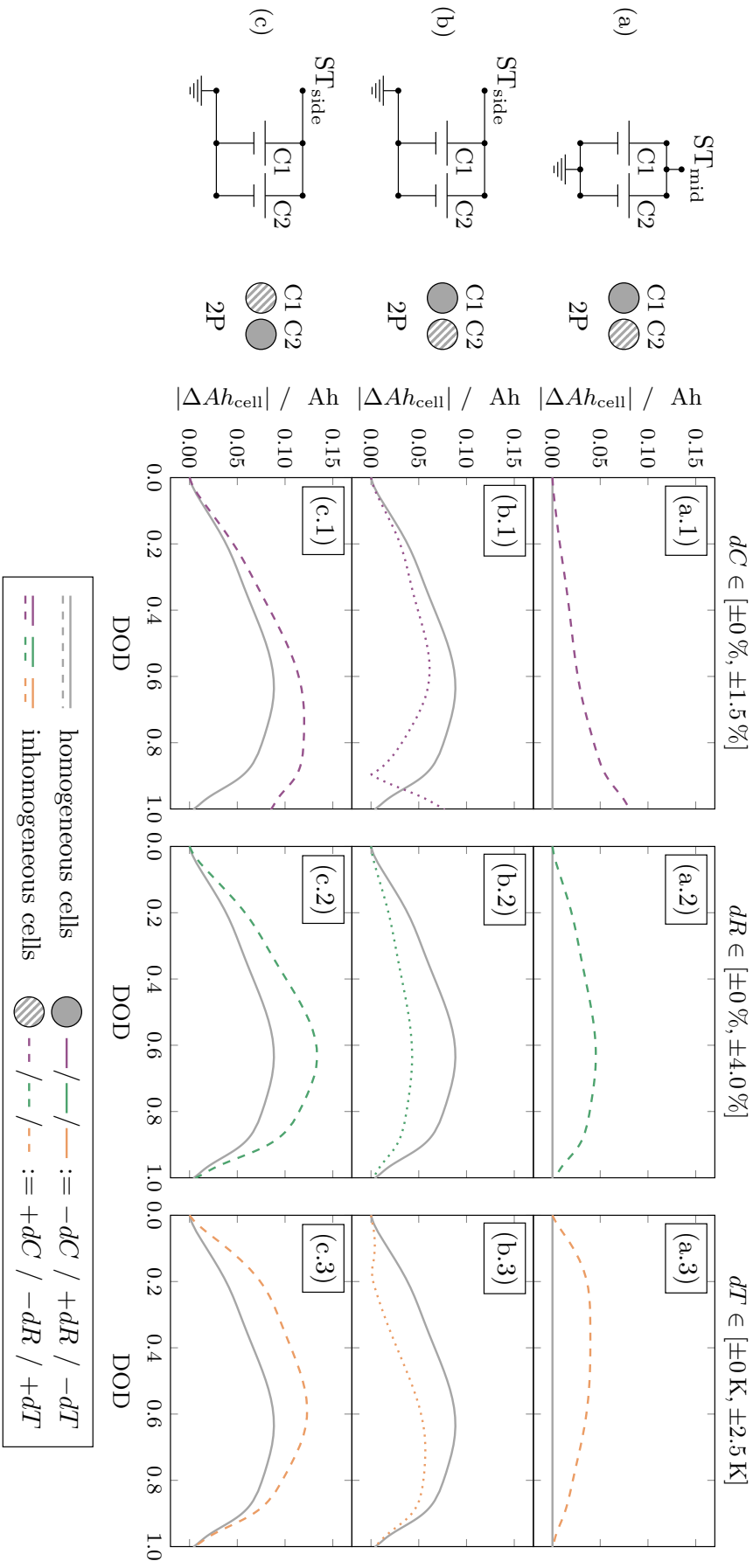


Figure 5.8: Absolute difference in Ah-throughput $|\Delta Ah_{\text{cell}}| = |Ah_{\text{cell}1} - Ah_{\text{cell}2}|$ between the parallel connected cells within a 2P module during a 1C discharge. Homogeneous cells are depicted by grey lines, inhomogeneous cells are depicted by coloured dotted (for case (b)) in Figure 5.6) or dashed (for cases (a) and (c) in Figure 5.6) lines.

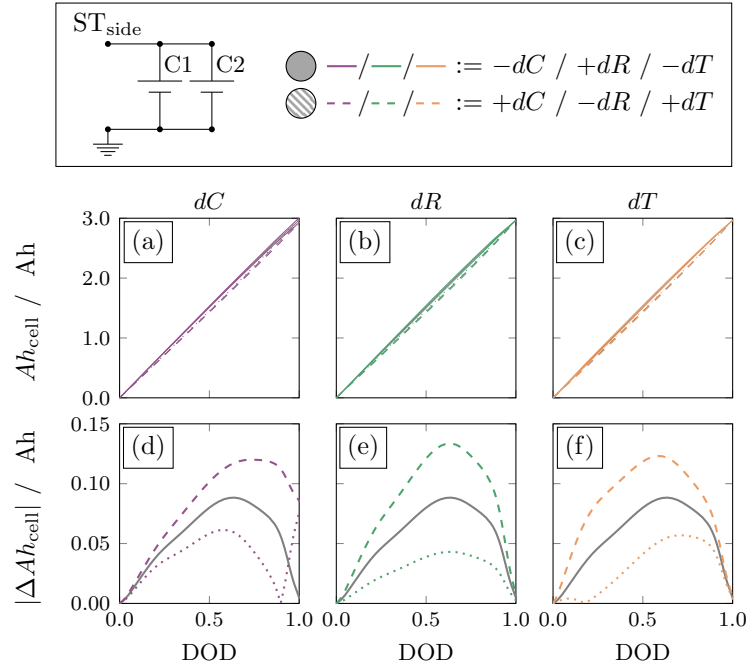


Figure 5.9: Graphs (a), (b) and (c) show the cumulated Ah-throughput Ah_{cell} through the parallel connected cells within a 2P module contacted at ST_{side} during a $1C$ discharge for a dC , dR and dT variation respectively. In graphs (d), (e) and (f) the absolute difference in Ah-throughput between the two cells $|\Delta Ah_{\text{cell}}| = |Ah_{\text{cell1}} - Ah_{\text{cell2}}|$ is given. Homogeneous cells are depicted by grey lines, inhomogeneous cells are depicted by coloured dotted (for case (b) in Figure 5.6) or dashed (for case (c) in Figure 5.6) lines.

5.3.3 Influence of the C-Rate

To examine the influence of the *C-Rate* on the resulting current distribution within a 2P module under cell-to-cell variations, the module is subjected to $0.25C$ and $4C$ in the following.

Figures 5.10 and 5.11 show the resulting current distribution during a $0.25C$ and $4C$ discharge over the respective system's DOD.

During a $0.25C$ discharge, the current distribution between the cells shows much more fluctuations compared to a $1C$ discharge. This is due to the fact, that the influence of the cells' OCVs is more pronounced at small *C-Rates*. The influence of induced cell-to-cell variations however, is comparable to that during a $1C$ discharge. Under an ST_{mid} connection, a dC variation does not result in a TP of the two current, whereas a dR and dT variation do. Under an ST_{side} connection, assembling the cell with a smaller capacity (compare Figure 5.10 (b.1)) or smaller impedance (compare Figure 5.10 (c.2)) near the ST results in increased peak currents within the system. Regarding a temperature gradient across the module, a difference to the simulation which uses a $1C$ current can be observed. Although a certain current distribution due to a dT variation has been present under a $1C$ discharge, this effect is reduced under a smaller *C-Rate*. Under an ST_{mid} connection, the currents of the two cells are nearly equal (compare Figure 5.10 (a.3)). Only at the beginning of the discharge a small deviation can be noted. The same is true for an ST_{side} connection. The current distribution which is visible in Figure 5.10 (b.3) and (c.3) is mainly due to the asymmetric current collector. Only until a $DOD \approx 0.15$ an additional current distribution compared to that of homogeneous connected cells can be observed.

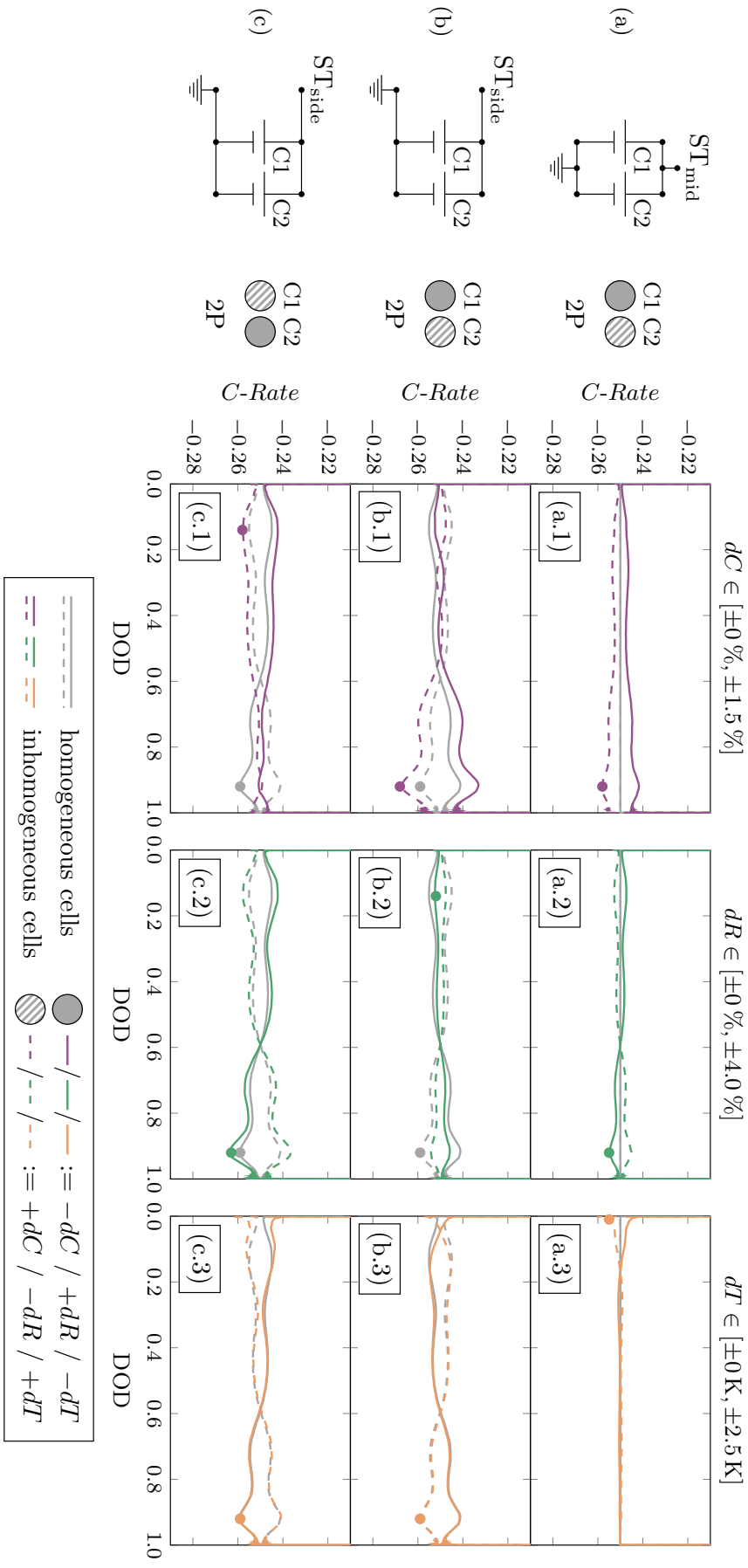


Figure 5.10: Current distribution during a $0.25C$ discharge scenario within the connected cells of a 2P module, which is contacted at ST_{mid} (case (a)) or ST_{side} (case (b) and case (c)) and which is subjected to differently induced inhomogeneity. The left hand side of the figure shows the schematic ECMs of the systems and relates the positions of the cells to the used line types according to the cell shading. The currents within the homogeneous system are displayed by grey lines. When inhomogeneities are induced, the solid shaded cell has a smaller capacity, a higher impedance or a lower initial temperature than the dashed shaded cell. The main part of the figure shows the current distribution due to a dC (purple lines), dR (green lines) and dT (orange lines) inhomogeneity respectively. The dots mark the maximum observed peak currents.

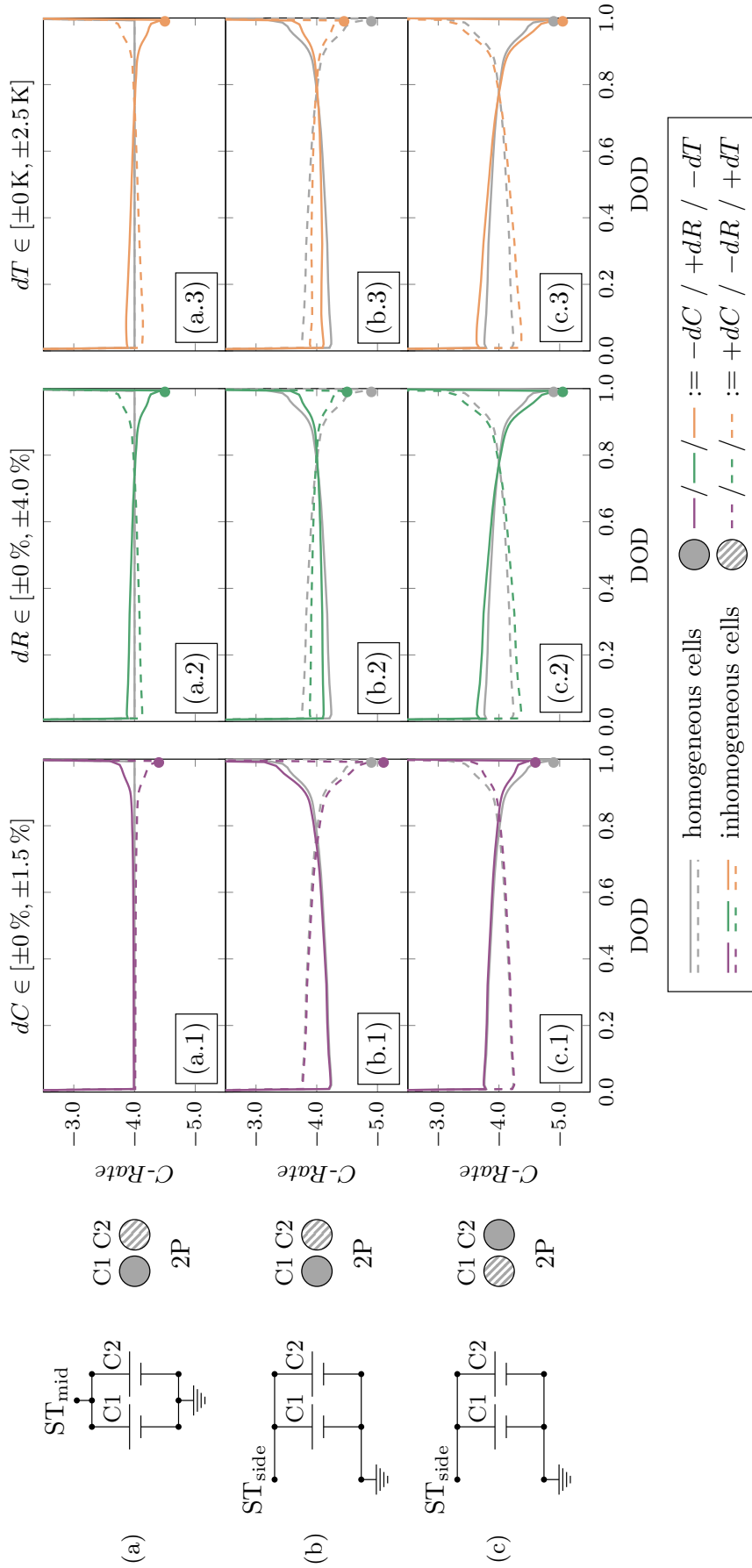


Figure 5.11: Current distribution during a 4C discharge scenario within the connected cells of a 2P module, which is contacted at ST_{mid} (case (a)) or ST_{side} (case (b) and case (c)) and which is subjected to differently induced inhomogeneity. The left hand side of the figure shows the schematic ECMs of the systems and relates the positions of the cells to the used line types according to the cell shading. The currents within the homogeneous system are displayed by grey lines. When inhomogeneities are induced, the solid shaded cell has a smaller capacity, a higher impedance or a lower initial temperature than the dashed shaded cell. The main part of the figure shows the current distribution due to a dC (purple lines), dR (green lines) and dT (orange lines) inhomogeneity respectively. The dots mark the maximum observed peak currents.

Table 5.6: Resulting maximum peak currents above the intended applied C -Rate per cell in % within a 2P module which is exposed to dC , dR and dT variations under different C -Rates. The rows (a), (b) and (c) refer to the respective cases in Figure 5.6 (1C), 5.10 (0.25C) and 5.11 (4C).

C -Rate	Case	dC	dR	dT
0.25C	(a)	3 %	2 %	2 %
	(b)	7 %	1 %	4 %
	(c)	3 %	5 %	4 %
1C	(a)	6 %	5 %	4 %
	(b)	16 %	5 %	8 %
	(c)	4 %	16 %	13 %
4C	(a)	10 %	13 %	13 %
	(b)	28 %	13 %	11 %
	(c)	15 %	26 %	26 %

This is due to the fact that at small C -Rates, the heat generation within the cells is much smaller than under a 1C current.

During a 4C discharge, the current distribution between the cells shows less fluctuations compared to a 1C discharge. For all induced variations and regardless of the chosen ST position, the maximum peak currents are observed at the very EOD. As under a 1C discharge, smaller peak currents are present if the cell with the higher capacity, higher impedance or lower ambient temperature is assembled close to the ST.

Table 5.6 compares the resulting maximum peak currents above the intended applied C -Rate per cell in % within the 2P module which is exposed to dC , dR and dT variations under the different simulated C -Rates. The rows (a), (b) and (c) refer to the respective cases in Figure 5.6 (1C), Figure 5.10 (0.25C) and Figure 5.11 (4C).

It becomes clear that the observed peak currents, which exceed the intended applied C -Rate, increase relatively with an increasing applied C -Rate. Whereas for a 0.25C discharge, the highest peak currents under an ST_{side} connection exceed the intended applied C -Rate by 7 % (dC) 5 % (dR) and 4 % (dT), the excess is as high as 16 % (dC) 16 % (dR) and 13 % (dT) for a 1C discharge and 28 % (dC) 26 % (dR) and 26 % (dT) for a 4C discharge. Therefore, cell-to-cell variations do – especially under an asymmetric current collector design – have a larger impact on the resulting peak currents within the system if higher C -Rates are applied.

5.4 Implications for assembling battery modules

From the results, three implications for assembling battery modules can be extracted regarding the connection of cells which show cell-to-cell variations.

- A A symmetric design of cell connectors results in a symmetric current distribution between two homogeneous parallel connected cells, whereas an asymmetric design results in asymmetric currents.
- B An asymmetric design of cell connectors can have a much larger impact on an inhomogeneous current distribution within a battery module than cell-to-cell parametric variations do. The extent of this impact depends on the resistances of the assembled cell connectors and on the assembled cell-to-cell variations.
- C If the applied *C-Rate* is higher, the maximum observed peak currents within the system increase relative to the applied *C-Rate*.

5.5 Conclusion

Comparing the observed current distribution under a symmetrically and an asymmetrically contacted module, it becomes clear that a symmetric design of cell connectors results in a symmetric current distribution between two homogeneous parallel connected cells, whereas an asymmetric design results in asymmetric currents due to the resistances of the cell connectors. Under the simulated dC , dR , and dT cell-to-cell variations and assembled cell connectors, an asymmetric design has a much larger impact on the current deviation than cell-to-cell variations do. Regarding the presented investigation, lower peak current have been observed within an asymmetrically contacted module if the cell with a higher cell internal polarisation is assembled close to the ST. This means, that the cell with a higher capacity or higher impedance should be assembled close to the ST. In case thermal gradients are to be expected across the module, the ST should be exposed to the lower ambient temperature. In order to minimize the Ah difference between the cells, the cell with a lower capacity or higher impedance shall be assembled close to the ST. Exposing the ST to the smaller ambient temperature will further decrease the Ah difference. Cell-to-cell variations have a larger impact on the resulting peak currents within the system if higher *C-Rates* are applied.

6

Cell matching strategy for peak current reduction

Chapter 5 has offered first results of assembling strategies within a battery module if cell-to-cell variations are known and either peak currents shall be reduced or the Ah difference between the cells shall be minimized. As depicted in Figure 5.6, peak currents which exceed the intended *C-Rate* per cell can occur within a system of parallel connected cells due to both, cell-to-cell variations and module design related reasons such as thermal gradients or an asymmetric cell connection design. The previous investigation has been based on a module which used Hilumin strips as cell connectors. The induced cell-to-cell variations have been varied individually to guarantee comparability between the evolving current distribution and the one resulting from a thermal gradient across the module.

In a real application, a thermal gradient across a module can be expected in most cases. Cells which are assembled in the middle of the battery module dissipate heat less easily than cells assembled at the edge of a module and will therefore show an increased temperature. Although a thermal management system can help to homogenise this temperature distribution, it can on the other hand also lead to a further thermal gradient if the module is cooled from one side, i.e. by air cooling. The cell connectors in a real application can be made of various materials, i.e. copper, aluminium, Hilumin or various alloys, and of different shapes, i.e. strips or thicker bars. Within an asymmetric current collector design, this will affect the module performance differently. From a battery module manufacturer's view, inhomogeneity can thus be reduced if either the assembled cells are matched, or if the thermal management or cell connectors are designed according to the optimization scenario.

By enhancing the investigations which have been carried out in Chapter 5, the possibility of cell matching for reducing peak currents during operation is examined in the following. On the one hand, assembling cells with varying capacity and impedance under an expected thermal gradient is analysed. Like this, the combination of an externally induced dT variation and a cell internal dC or dR variation can be compared. On the other hand, the influence of the cell connector resistance of different cell

Table 6.1: Resulting maximum peak currents above the intended applied C -Rate of $1C$ per cell in % within a 2P module which is exposed to different thermal gradients and under additional attributed dC and dR variations. The rows (a), (b), (c) and (d) refer to the respective cases in Figure 6.1.

Case	dX	$dT_{\text{ref},1} = 0 \text{ K}$	$dT_{\text{ref},1} = -2.5 \text{ K}$	$dT_{\text{ref},1} = +2.5 \text{ K}$
		$dT_{\text{ref},2} = 0 \text{ K}$	$dT_{\text{ref},2} = +2.5 \text{ K}$	$dT_{\text{ref},2} = -2.5 \text{ K}$
(a)	dC	5 %	5 %	8 %
	dR	5 %	8 %	3 %
(b)	dC	5 %	8 %	5 %
	dR	5 %	3 %	8 %
(c)	dC	13 %	13 %	18 %
	dR	4 %	3 %	8 %
(d)	dC	5 %	3 %	8 %
	dR	14 %	13 %	18 %

connectors on the resulting peak currents is analysed and their influence on the module performance is discussed. Based on the results, implications for assembling battery modules under a cell matching perspective for peak current reduction are derived.

This chapter is mainly based on the publication “Influence of cell-to-cell variations on the inhomogeneity of lithium-ion battery modules” by Rumpf et al. [39].

6.1 Assembling cells under an expected thermal gradient

In case a thermal gradient across the battery module is to be expected due to an external heat source at one end of the module or due to thermal management design, it will affect the degree of impact which cell-to-cell variations have on the inhomogeneous current distribution. Figure 6.1 shows the resulting current distribution for a 2P module which is exposed to a thermal gradient of $dT \in \{0, 5, -5\}\text{K}$. Additional to each of these thermal gradients, the connected cells are attributed dC (compare purple lines) and dR (compare green lines) variations respectively. The line types refer to the cells’ positions and shadings as depicted one the left of the respective case. The highest occurring peak currents per cell are additionally highlighted in the graphs by coloured dots.

The values of the highest occurring peak currents per system are given in Table 6.1 for each of the cases depicted in Figure 6.1 and for both, the additional dC and dR variation.

If no thermal gradient is present across a battery module which is contacted at ST_{mid} (compare Figure 6.1 (a.1) and (b.1)), both, the induced dC and dR variation result in a maximum peak current of 5% above the intended applied C -Rate per cell. As the cell connectors are symmetric, the inverted assembling of the cells has no effect. This is straight forward but is still mentioned for the sake of completeness. For a module contacted at ST_{side} however (compare Figure 6.1 (c.1) and (d.1)), the positioning of the cells has an effect on the resulting peak currents, as already discussed in Section 5.3.

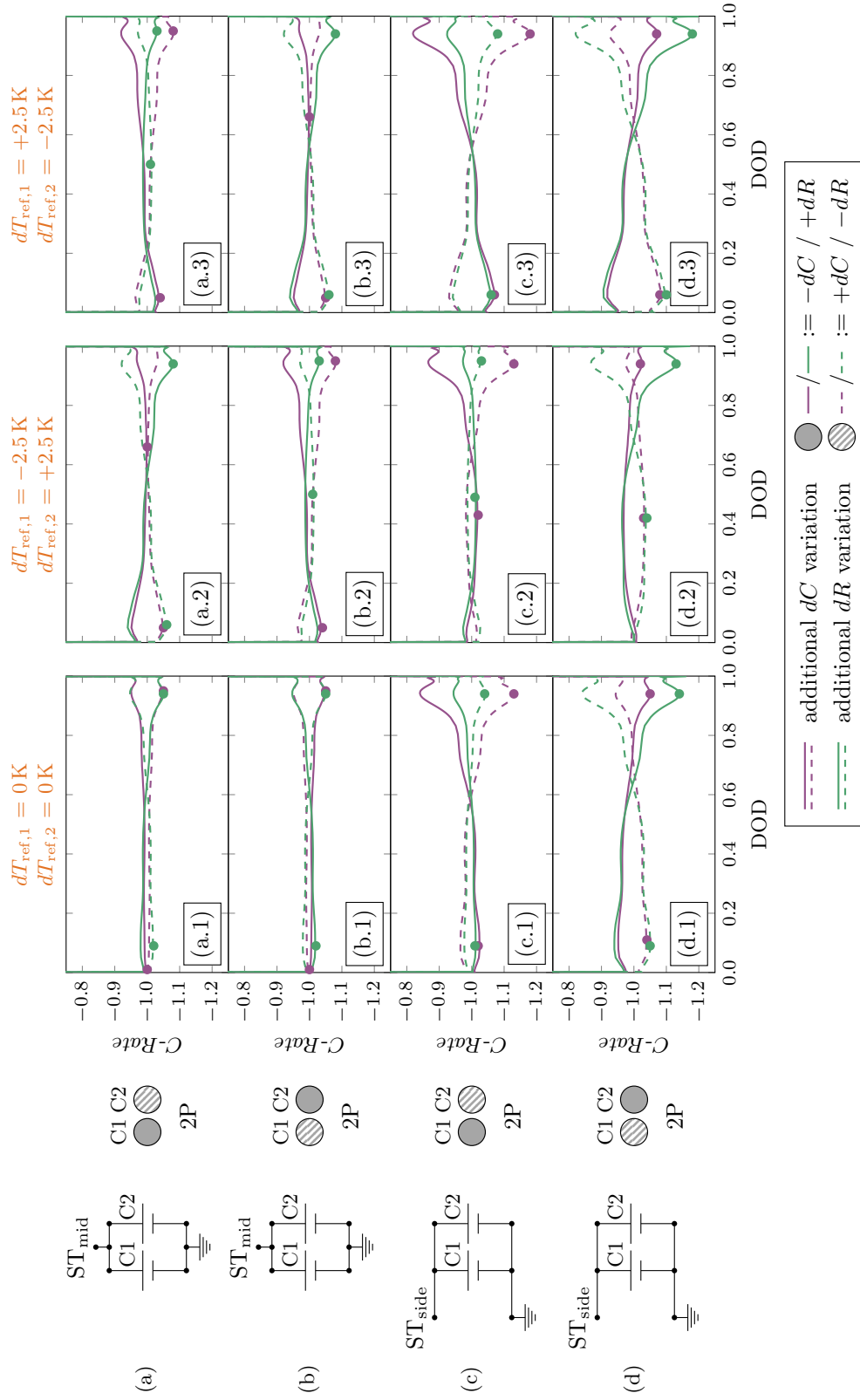


Figure 6.1: Current distribution under a 1C discharge scenario within the connected cells of a 2P module under different thermal gradients $dT \in \{0, 5, -5\}\text{K}$. Additional to the thermal gradients, the connected cells are attributed dC (compare purple lines) and dR (compare green lines) variations respectively. The line types of cell 1 and cell 2 are displayed according to the cells' positions and shadings as depicted on the left. The dots mark the highest occurring peak currents per cell per variation.

If cell 1 is exposed to the lower ambient temperature ($dT_{\text{ref},1}=-2.5\text{ K}$) and cell 2 is exposed to the higher ambient temperature ($dT_{\text{ref},2}=2.5\text{ K}$) (compare Figure 6.1 (a.2) and (b.2)) under ST_{mid} , the peak currents are reduced if the colder cell has the smaller capacity and smaller impedance. Under ST_{side} (compare Figure 6.1 (c.2) and (d.2)), the peak currents are reduced if the colder cell (in this case next to the ST) has the higher capacity and higher impedance.

If cell 1 is exposed to the higher ambient temperature ($dT_{\text{ref},1}=2.5\text{ K}$) and cell 2 is exposed to the lower ambient temperature ($dT_{\text{ref},2}=-2.5\text{ K}$) (compare Figure 6.1 (a.3) and (b.3)) under ST_{mid} , the peak currents are reduced if the colder cell has the smaller capacity and smaller impedance. Under ST_{side} (compare Figure 6.1 (c.3) and (d.3)), the peak currents are reduced if the colder cell (in this case further away from the ST) has the smaller capacity and smaller impedance.

Thus, if the maximum occurring peak currents during a full CC-DCH shall be reduced under ST_{mid} , the cell with the smaller capacity or impedance should be assembled towards the lower ambient temperature. Under ST_{side} , it has to be differentiated whether the ST is exposed to the lower or higher ambient temperature. If the ST is exposed to the lower ambient temperature, the cell with the higher capacity or higher impedance should be assembled close to the ST. If the ST is exposed to the higher ambient temperature, the cell with the smaller capacity or smaller impedance should be assembled close to the ST.

Note, that these results depend on the chosen ranges of investigated dC , dR and dT variations. For other ranges, the results might adapt. In the experimental investigation in Chapter 4 the capacity and impedance of fresh cells showed neither a positive nor a negative correlation. Nevertheless this also means that, within a batch of cells, there are cells which show both, a higher capacity and a higher impedance relative to the mean values of the batch. Thus, assembling such a cell well or bad will have an even larger impact on the inhomogeneous current distribution within a module than under the above presented variations.

6.2 Influence of cell connector resistances on resulting peak currents

Comparing the results of an ST_{mid} contact with those of an ST_{side} contact in Figure 6.1, it can be observed that the peak currents within the ST_{mid} topologies are smaller. This is due to the lacking additional influence of the cell connector resistances on the current distribution, which are present within an asymmetrically contacted module. The assembled cell connector resistances R_{conn} seem to have a similar if not larger impact on the current distribution within asymmetrically contacted modules than the induced variations or exposed thermal gradients. This influence will be further investigated in the following.

Cells can be connected by cell connectors of different material and thickness. These will lead to different cell connector resistances R_{conn} . In the following, the peak currents within an ST_{side} -connection are investigated depending on the ratio of R_{conn} to R_{cell} . $R_{\text{cell}} = 18\text{ m}\Omega$ is the nominal resistance of the investigated cell. The cell connectors which are to be compared are a copper bar, a copper strip, an aluminum strip, a Hilumin strip (which has been investigated so far) and a thinner Hilumin strip. They represent a step by step increased electric resistance. The data of the respective connectors are given in Table 6.2.

Table 6.2: Electrical resistance data for cell connectors of different material and thickness. The length and width of all connectors is $l_{\text{conn}} = 4.5$ cm and $w_{\text{conn}} = 1$ cm respectively as already given in Table 5.5. The previously presented results have been modelled based on the data for the Hilumin strip in 0.5 mm thickness. The last column of the table gives the ratio between the respective connector resistance and the nominal cell internal resistance ($R_{\text{cell}} = 18$ m Ω) in %.

Connector	σ_{conn} (S m $^{-1}$)	t_{conn} (mm)	R_{conn} (m Ω)	$\frac{R_{\text{conn}}}{R_{\text{cell}}}$ (%)
Copper bar	5.96×10^7	2	0.04	0.2
Copper strip	5.96×10^7	0.5	0.15	0.8
Aluminum strip	3.77×10^7	0.5	0.24	1.3
Hilumin strip	9.93×10^6	0.5	0.90	5
Hilumin strip thin	9.93×10^6	0.2	2.30	12.8

Figure 6.2 (a) presents the current distribution within a 2P module contacted at ST_{side} with homogeneous cells but different cell connectors under a $1C$ discharge regime. The different cell connectors are depicted by different shades of grey. The connector with the highest cell connector resistance (thin Hilumin strip) is illustrated by the darkest shade of grey. The connector with the lowest cell connector resistance (copper bar) is illustrated by the lightest shade of grey. The observed peak currents are highlighted within graph (a). The highest peak currents are observed for thin Hilumin strips, which show the highest electric resistance, whereas the smallest peak currents are observed for copper bars. The obtained peak currents are related to the applied C -Rate per cell and depicted in Figure 6.2 (b), (c) and (d) in grey. Graphs (b), (c) and (d) moreover show the resulting peak currents under a dC variation (purple curves), dR (green curves) and dT (orange curves) variation respectively. The line types refer to the cells' positions and shadings. The dark coloured curves depict the simulations with a negative dC , dR or dT . The light coloured curves depict the simulations with a positive dC , dR or dT . The legend of Figure 6.2 states, how the dC , dR and dT variation affects the respective capacity, impedance and temperature of the two connected cells.

Analysing the grey coloured curves for homogeneous cells, it becomes clear that the observed peak currents increase for both cells with increasing cell connector resistance R_{conn} . Moreover, the cell which is situated farther away from the ST experiences a higher peak current (note, that the dashed line is above the solid line for all R_{conn}). Using a 2 mm thick copper bar as cell connector minimizes the absolute current peaks to less than 1% above the intended applied C -Rate. For a 0.2 mm thin Hilumin strips however, the peak current will exceed the intended C -Rate by as much as 25%.

In contrast to homogeneous connected cells, the peak currents are not necessarily the smallest for low resistant cell connectors, as soon as cells under any type of cell-to-cell variation (dC , dR and dT) are connected. The light coloured curves show the smallest overall peak currents within the system for aluminium strips. For each of the dC , dR and dT variations an excess of 3% over $1C$. With even smaller R_{conn} (i.e. copper strips or bars) the maximum observed peak currents increase again. This is due to the fact that the cell connector resistances work against the difference in cell internal overpotentials due to variations if the cells are matched accordingly. Smaller R_{conn} are too small to

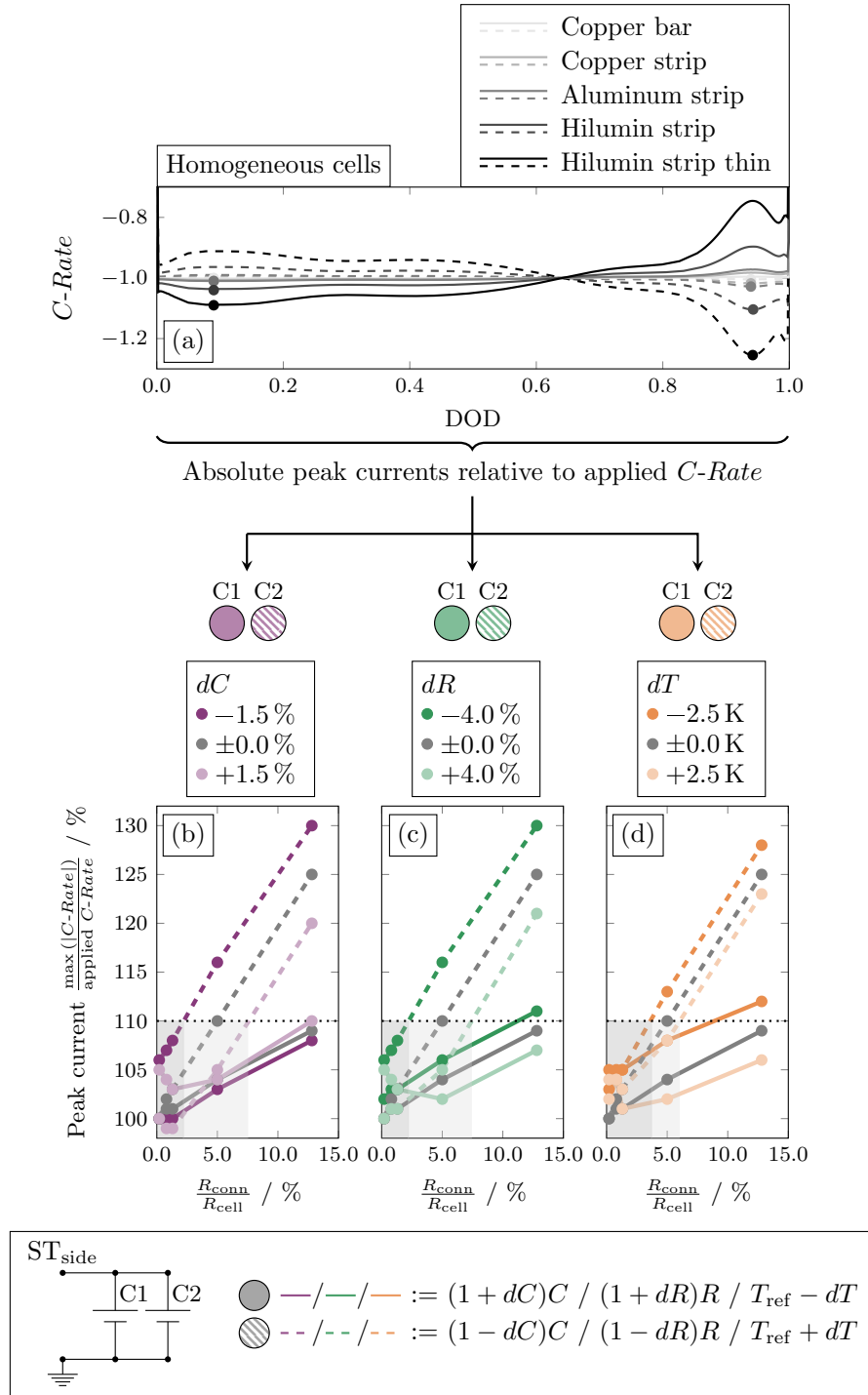


Figure 6.2: Influence of different cell connector resistances on the observed peak currents within a 2P module under a ST_{side} -connection and under a 1C CC-discharge. Graph (a) displays the current distribution for homogeneous connected cells. The lower graphs (b), (c) and (d) depict the observed peak currents per cell relative to the intended applied $C\text{-Rate}$ per cell in dependence of the different cell connector resistances. They refer to a dC (b), dR (c) and dT (d) variation respectively. As before, if cell 1 has a higher capacity, impedance or temperature, then cell 2 has a lower one and vice versa. The grey lines represent homogeneous cells. The current through cell 1 is depicted by solid lines, the one through cell 2 by dashed lines according to the cells' positions and shadings. The black dotted lines mark a threshold peak current of 10% above the intended applied $C\text{-Rate}$ per cell. This threshold value is not exceeded if the cell connectors are chosen from the grey shaded areas, as both together belonging lines lie within these areas. The legend of the depicted scenario is shown in the lower box.

level the existing variations and the peak currents are therefore larger. Using thin Hilumin strips as cell connectors under dC , dR and dT variations results in peak currents of 20 %, 21 % and 23 % above $1C$ for well matched cells and of 30 %, 30 % and 28 % above $1C$ for badly matched cells. Note, that these values depend on the simulated variation ranges. With the ranges used in this study, a dC variation of -1.5% results in the same maximum peak currents through cell 2 as a dR variation of -4% (compare dark coloured dashed lines in (b) and (c)).

For all types of cell-to-cell variation (dC , dR and dT) and independent of the chosen cell connectors, both light coloured curves lie beneath the highest dark coloured curve. The highest peak currents are observed for the respective highest dark coloured curve – if the cell with the low capacity, low impedance or high ambient temperature is assembled close to the ST. In other words, peak currents can be reduced, if the cell with the higher capacity or higher impedance is assembled close to the ST – and this is independent of the chosen cell connectors. Whether the cell close to the ST experiences the highest peak current or whether the other cell does, depends on the assembled cell connectors. In case thermal gradients are to be expected across the module, the ST should be exposed to the lower ambient temperature.

From a manufacturer's point of view the question arises, how the appropriate cell connector for a battery module shall be chosen in order to ensure that the peak currents will not exceed a certain threshold value

1. if the individual cells' capacity and impedance have not been determined prior to the module assembly and the cells might therefore be arbitrarily connected in a bad matching scenario.
2. if the individual cells' capacity and impedance have been determined prior to the module assembly and therefore a matching approach can be followed.

Figure 6.2 can be used to answer these questions by choosing the appropriate cell connectors dependent on the occurring cell-to-cell variations and tolerable threshold peak current. Arbitrarily, the tolerable peak current through any of the connected cells is assumed to be 10 % above the intended applied C -Rate per cell (compare black dotted lines in Figure 6.2). For a $1C$ discharge as depicted in Figure 6.2, each cell would be allowed to experience a peak current of $1.1C$.

Regarding question (1), in order to not exceed the chosen threshold value and to compensate a possible bad matching in capacity, impedance or thermal gradient across the module, the ratio of cell connector resistance to cell impedance $\frac{R_{\text{conn}}}{R_{\text{cell}}}$ should lie within the dark grey shaded areas in Figure 6.2 (b) to (d). In this case, the cell connector could be made of a copper bar, a copper strip or an aluminum strip. Of these cell connectors, the aluminum strip has the highest R_{conn} . Therefore, the aluminum strip is given in Table 6.3, which states the respective maximum suitable percentage values of $\frac{R_{\text{conn}}}{R_{\text{cell}}}$ and the corresponding cell connector material. Note, that also cell connector materials with lower R_{conn} than the given material are suitable.

Regarding question (2), if the cell-to-cell variations are known prior to the module assembly, and if the cells are matched accordingly, then the allowed range, from which the cell connector can be chosen, increases (compare additional light grey shaded areas in Figure 6.2 (b) to (d)). In this case, the cell connector could not only be made of a copper bar, copper strip or aluminum strip but could alternatively be made of a Hilumin strip.

Table 6.3: Maximum suitable cell connector resistance values relative to the cell impedance $\frac{R_{\text{conn}}}{R_{\text{cell}}}$ and corresponding cell connector material in order to not exceed a threshold peak current of 10% above the intended applied *C-Rate* per cell. Also cell connector materials with lower R_{conn} than the given material are suitable. The matching column refers to the line colours in Figure 6.2: homogenous cells = grey lines, bad matching (high peak currents) = dark coloured lines, good matching (low peak currents) = light coloured lines.

Matching	dC	dR	dT	Cell connector
bad	2.2%	2.2%	3.7%	Aluminum strip
homogeneous	5%	5%	5%	Hilumin strip
good	7.5%	7.4%	6%	Hilumin strip

6.3 Implications for assembling battery modules under a cell matching perspective

From the results, three further implications for assembling battery modules can be extracted regarding the connection of cells which show cell-to-cell variations – additional to those three implications already stated in Chapter 5.4.

- D Even if the connected cells were homogeneous in capacity and impedance and if the battery module was not subjected to an external thermal gradient, current peaks of 25% above the intended applied *C-Rate* per cell have been observed during a 1*C* CC discharge for thin Hilumin strips. When using copper bars as cell connectors however, the excess peak currents can be reduced to 1%.
- E If the arrangement of the cells within the module is chosen disadvantageously under a dC , dR or dT variation, these current peaks can increase to about 6% above 1*C* under the usage of copper bars and to even about 30% under the usage of thin Hilumin strips respectively.
- F Matching the cells during module assembly can minimize the peak currents within an asymmetrically contacted module. Independent of the chosen cell connectors, the peak currents are reduced if the cell with a higher cell internal polarisation is assembled close to the ST. This means, that the cell with a higher capacity or higher impedance should be assembled close to the ST. In case thermal gradients are to be expected across the module, the ST should be exposed to the lower ambient temperature.

6.4 Conclusion

By analysing the assembly of cells within an asymmetrically contacted module, it has been found that in order to reduce the occurring peak currents by cell matching, the cell with a higher capacity or higher impedance should be assembled close to the ST. In case thermal gradients are to be expected across the module, the ST should be exposed to the lower ambient temperature. During the study conducted in this chapter, it has furthermore been found that these conclusions are valid for any

chosen cell connectors. The withdrawn implications for matching of two parallel connected cells can be transferred to parallel connected battery modules and are therefore valuable regarding second life applications of battery modules.

Depending on the desired field of application of the battery module, the developed model can also be used to examine other optimization scenarios regarding cell matching. These will be discussed during the outlook presented at the end of this thesis.

7

Conclusion and outlook

This work presented an investigation regarding the causes and effects of inhomogeneity in lithium-ion battery modules using a physicochemical modelling approach. Therefore, on the one hand, an experimental determination and statistic analysis of the cell-to-cell variations of different cell parameters and of the correlation between these parameters has been performed. On the other hand, a holistic multidimensional multiphysics model for battery modules has been presented. This model uses a physicochemical model per connected cell and accounts for temperature dependent transport and kinetics parameters, conservation of charge and energy between the connected cells and heat exchange with the surroundings. Using the model, the influence of cell-to-cell variations on the inhomogeneity of a generalised 2P module is investigated and compared to the resulting impact by thermal gradients and an asymmetric current collector design. Furthermore, the model is used to investigate cell matching strategies for reducing peak currents in battery modules. From the results of both, the experimental and simulative investigation, implications regarding the development and modelling of battery modules as well as the assembly of battery modules have been derived.

This conclusion first summarizes the results of the parametric cell-to-cell variation and correlation study and of the analysis of inhomogeneity in battery modules. Afterwards, an outlook towards further research objectives is given.

7.1 Cell-to-cell variation and correlation

For the design and assembly of battery modules, cell capacity and impedance are crucial parameters which should be characterised regarding cell-to-cell parametric variations. Although cell characterisation prior to a battery module's assembly is time consuming, the use of similar cells is still advantageous and recommended. Similar cell capacities allow for a best possible utilisation of available capacity and similar cell impedances form the basis for evenly distributed currents within a module from the beginning of module operation. Therefore, cell matching during the assembly of battery modules is crucial

in order to minimize inhomogeneity in battery modules due to cell-to-cell variations [132]. The results of Chapter 4 allow a conclusion about which parameters are suitable for cell matching during the assembly of battery modules. Based on this, only the most crucial parameters need to be determined during cell characterisation measurements and thus measuring time and resources can be saved.

In Chapter 4, the experimental and statistic study of parametric cell-to-cell variation of 15 different cell parameters and the correlation between them has been based on 1100 commercial production fresh LiFePO₄-graphite cells being part of two batches (B1: cell 1-600, B2: cell 601-1100). This presented combination is unique in literature: only little publications have based their statistic analysis on more than 100 cells and often the parametric variation has only been determined for a limited number of parameters.

Overall, it has been found that the investigated cell showed small cell-to-cell parametric variations compared to values reported in literature studies [9; 19]. The two batches revealed no large differences for most parametric variations.

For fitting purposes during ECM modelling, often used cell parameters are either DC impedances determined from pulse tests or AC impedances determined from EIS measurements. The investigated DC impedances all showed a similar statistic behaviour with a relative variation σ/μ of about 1.3% and a strong correlation between them. The statistic analysis of the ohmic AC impedances of batch B1 revealed two separate cell groups, although the cells have been from one batch. As the statistic analysis of the DC impedances was not able to depict this group building, the ohmic AC impedances seem more appropriate in order to determine cell-to-cell variations regarding a cell's impedance. The correlation between the two investigated ohmic AC impedances was strong. Therefore, using a fast measurement technique like an impedance meter or battery tester which determines the ohmic impedance at a constant frequency $f = 1000$ Hz is justifiable.

As batch B2 did not show the mentioned group building within the AC impedances, this batch was found to be more suitable for further analyses. The relative variation of the ohmic AC impedance was 0.72%, whereas the one of the CC-discharge capacity was 0.45% and even smaller for the CCCV-discharge capacity (0.28%) as in this case the influence of the variation of the cell impedance had been reduced. The variation ratios between cell capacity and ohmic impedance are 1:1.5 (CC) and 1:2.2 (CCCV) respectively.

Often other characteristic impedances (i.e the local maximum or minimum within a Nyquist plot), which have been determined from an EIS measurement, are used for model fitting purposes. For these parameters the conducted study showed, that the related measurement frequencies should be chosen carefully as a strong correlation between frequency and impedance has been depicted. In this case pre-measurements should be performed in order to find the most promising fixed frequency for the characteristic point. Another option would be to choose the frequency density around the desired point sufficiently high – especially if the local maximum plateau within the Nyquist diagram is flat and the local minimum is smooth. Pre-measurements can help to achieve a compromise between a prolonged measurement time and a high fitting accuracy.

The cell impedance influences the discharge capacities and the mean temperature of the cell. A higher cell impedance leads to higher overpotentials during the discharge of the cell – therefore, the CC-phase is shorter. Reducing these overpotentials takes longer which increases the duration of the CV-phase. As the temperature mainly increases during the CC-phase, also the mean temperature during the CU-measurement is lower for cells with a higher impedance. For the CCCV-discharge capacity the influence

of the variation of the cell impedance and therefore also of the temperature is reduced. Therefore, in order to characterise a batch of cells regarding its capacity variation, the determination of the CCCV-discharge capacity is sensible. As this capacity does not correlate with any of the impedances, it can be concluded, that the variation of the cell capacity allows no conclusion about the variation of the cell impedance.

In conclusion, in order to characterise the parametric variation among cells, the most effective and time efficient parameter to depict the impedance variation is the R_{AC_1000Hz} impedance. To identify the variation of capacity the parameter C_{DCH_CCCV} should be determined.

The withdrawn implications in this chapter are useful for the development and modelling of battery modules. The experimentally determined parametric variation values and drawn conclusions are valuable for model fittings and battery pack analyses which had up to now been based on assumptions about cell-to-cell variations. As the investigated cells have been production fresh cells, the reported cell-to-cell variations and correlations refer to manufacturing tolerances and the operational behaviour of fresh cells and cannot be adopted for aged cells.

7.2 Inhomogeneity of battery modules and matching strategy

In Chapter 5, a coupled multiphysics multidimensional model for a $xSyP$ battery module which is able to distinguish between the influence of cell-to-cell variations, thermal gradients and cell connector design on the inhomogeneity of lithium-ion battery modules has been presented. Resistances for cell connectors and welding spot joints have been considered for each single connection in the model. Thus, a possible irregularity during the battery module design or assembly could be examined and compared to the impact of assembling unmatched cells (in capacity or impedance) while discussing the influence of thermal gradients across the module. The implemented cell-to-cell variations in capacity and impedance have been based on the results determined in Chapter 4. By using a PCM for each cell, the arising inhomogeneity could be discussed from an electrochemical point of view.

The model coupling equations have been provided in depicted flow charts for each of the connected cells and have been stated in detail which allows for a high reproducibility. The aim was to make general statements about the evolving current distribution between connected cells under operation. Therefore, the influence of different cell-to-cell variations on the inhomogeneity of lithium-ion battery modules has been demonstrated for a generalised 2P module under a CC-DCH operation regime at 1C. From the results, the following implications for assembling battery modules have been derived.

For homogeneous parallel connected cells, a symmetric design of cell connectors results in a symmetric current distribution whereas an asymmetric design results in asymmetric currents due to the resistances of the cell connectors. If cells under cell-to-cell variations are assembled in parallel, the current distribution between the strings depends on the ratio of the respective sum of the cell's OCV, the cell's internal polarisation and the external polarisation due to the cell connector design. An asymmetric design of cell connectors can have a much larger impact on an inhomogeneous current distribution within a battery module than cell-to-cell parametric variations do. The extent of this impact depends on the resistances of the assembled cell connectors and on the assembled cell-to-cell variations.

In order to reduce the occurring peak currents within an asymmetrically contacted module by cell matching, Chapter 6 has revealed, that the cell with a higher capacity or higher impedance should be assembled close to the ST. In case thermal gradients are to be expected across the module, the

ST should be exposed to the lower ambient temperature. These statements have been found to be valid for all different cell connectors, which have been investigated, i.e. copper bars, copper strips, aluminium strips and Hilumin strips in different thicknesses. The withdrawn implications for matching of two parallel connected cells can be transferred to parallel connected battery modules and are therefore valuable regarding second life applications, where differently aged battery modules with varying impedances and capacities are connected.

7.3 Outlook

The conducted experimental and statistic study regarding cell-to-cell variation and correlation can be used for multiple scopes of application.

As done in Chapter 5, the obtained results from Chapter 4 can be used as a data basis when modelling connected cells and battery modules. Due to the fact that the data basis has been published separately [133], also other researchers can use these cell-to-cell variation data for integration into their models of battery modules and systems. In absence of a profound data set, cell parameter variations have often been chosen randomly within a reasonable range in order to being able to investigate the influence of cell-to-cell variations on the performance of battery modules by simulation [44]. Using real measured variation data instead can help to enhance the prediction accuracy of the model [18].

The distinct quantitative statements about the parametric variation of different cell external parameters provide an experimentally determined range of parametric variation and cell non-uniformity. The published data set can furthermore be used during the design of SOC balancing systems and state of health (SOH) monitoring methods for battery modules.

For optimising a battery system towards mass, volume and material cost, considering cell-to-cell variations in a model might not be of large importance [134]. However, regarding the optimisation of a battery module's performance by improving module design and cooling strategies [15], considering cell-to-cell variations and thereby arising temperature gradients across the module (additionally to those arising from the module geometry), would be beneficial [135]. For such optimization analyses, the results of Chapter 4 can be useful.

As in this thesis the cell under investigation was a LFP-graphite cell, the findings must be limited to this specific chemistry. Cells by a different manufacturer, of a different format or different cell chemistry can result in different cell-to-cell variations. Nevertheless the reported data can serve as an indication for thoroughly statistically analysed variation ranges. Especially regarding the current distribution and balancing processes between parallel connected cells, the OCV of the cells plays an important role. Therefore, examining cells of a different cell chemistry which have a steeper OCV, e.g. NMC-graphite cells, is likely to result in a different current distribution.

Depending on the desired field of application of a battery module, the model which has been developed in this thesis can also be used to examine other optimization scenarios regarding cell matching. When considering SEI-growth as the main capacity fade and power fade mechanism during ageing [29], the cell capacity and impedance modify according to the respective Ah-throughput and ambient temperature. If cells are connected in parallel and do either show cell-to-cell variations or are contacted asymmetrically, the current distribution within the module will consequently lead to differently aged cells. Due to the changing capacity and impedance over ageing, the inhomogeneous current distribution will adapt further over time of operation. Therefore, optimizing the overall homogeneity of current

distribution between parallel connected cells is expected to decrease the inhomogeneous ageing of the cells. To investigate this issue further, the developed model should be coupled to an ageing model, e.g. a model accounting for SEI-growth as introduced by Kindermann et al. [29].

The model, which has been developed in this thesis can furthermore be used to examine the influence of partial-load cycles on the inhomogeneity of battery modules. There are different reasons, why battery module operators might limit the range of operation to a partial-load range. For example, in order to retain a certain amount of backup energy during EV operation or in order to protect the assembled cells from low anode potentials and thus from lithium-plating. In case the module discharge was stopped at a point where the Ah difference between parallel connected cells was large, and in case a charging cycle would directly follow, the Ah difference is likely to change further. This use case as well as the influence of dynamic load cycles on the inhomogeneity of battery modules seems worth to be investigated in the future.

The developed modelling framework can furthermore be used to investigate larger module topologies under different operation scenarios. Thereby, also the scalability of the resulting thesis statements can be evaluated regarding larger battery systems. It is moreover possible to evaluate the performance of hybrid energy storages by either simultaneously connecting high power and high energy cells or by connecting lithium-ion cells of different chemistries.

List of References

- [1] S. Miyatake, Y. Susuki, T. Hikihara, S. Itoh, and K. Tanaka. “Discharge characteristics of multicell lithium-ion battery with nonuniform cells”. In: *Journal of Power Sources* 241 (2013), pp. 736–743.
- [2] C. T. Love, M. B. Virji, R. E. Rocheleau, and K. E. Swider-Lyons. “State-of-health monitoring of 18650 4S packs with a single-point impedance diagnostic”. In: *Journal of Power Sources* 266 (2014), pp. 512–519.
- [3] M. Dubarry, N. Vuillaume, and B. Y. Liaw. “From single cell model to battery pack simulation for Li-ion batteries”. In: *Journal of Power Sources* 186.2 (2009), pp. 500–507.
- [4] G. J. Offer, V. Yufit, D. A. Howey, B. Wu, and N. P. Brandon. “Module design and fault diagnosis in electric vehicle batteries”. In: *Journal of Power Sources* 206 (2012), pp. 383–392.
- [5] L. Wang, Y. Cheng, and X. Zhao. “A LiFePO₄ battery pack capacity estimation approach considering in-parallel cell safety in electric vehicles”. In: *Applied Energy* 142 (2015), pp. 293–302.
- [6] M. J. Brand, M. H. Hofmann, M. Steinhardt, S. F. Schuster, and A. Jossen. “Current distribution within parallel-connected battery cells”. In: *Journal of Power Sources* 334 (2016), pp. 202–212.
- [7] T. Bruen and J. Marco. “Modelling and experimental evaluation of parallel connected lithium ion cells for an electric vehicle battery system”. In: *Journal of Power Sources* 310 (2016), pp. 91–101.
- [8] M. Dubarry, N. Vuillaume, and B. Y. Liaw. “Origins and accommodation of cell variations in Li-ion battery pack modeling”. In: *International Journal of Energy Research* 34.2 (2010), pp. 216–231.
- [9] S. Paul, C. Diegelmann, H. Kabza, and W. Tillmetz. “Analysis of ageing inhomogeneities in lithium-ion battery systems”. In: *Journal of Power Sources* 239 (2013), pp. 642–650.
- [10] R. Gogoana, M. Pinson, M. Bazant, and S. Sarma. “Internal resistance matching for parallel-connected lithium-ion cells and impacts on battery pack cycle life”. In: *Journal of Power Sources* 252 (2014), pp. 8–13.
- [11] F. An, J. Huang, C. Wang, Z. Li, J. Zhang, S. Wang, and P. Li. “Cell sorting for parallel lithium-ion battery systems: Evaluation based on an electric circuit model”. In: *Journal of Energy Storage* 6 (2016), pp. 195–203.
- [12] N. Ganesan, S. Basu, K. S. Hariharan, S. M. Kolake, T. Song, T. Yeo, D. K. Sohn, and S. Doo. “Physics based modeling of a series parallel battery pack for asymmetry analysis, predictive control and life extension”. In: *Journal of Power Sources* 322 (2016), pp. 57–67.

- [13] L. Wang, Y. Cheng, and X. Zhao. “Influence of connecting plate resistance upon LiFePO₄ battery performance”. In: *Applied Energy* 147 (2015), pp. 353–360.
- [14] B. Wu, V. Yufit, M. Marinescu, G. J. Offer, R. F. Martinez-Botas, and N. P. Brandon. “Coupled thermal-electrochemical modelling of uneven heat generation in lithium-ion battery packs”. In: *Journal of Power Sources* 243 (2013), pp. 544–554.
- [15] T. Wang, K. J. Tseng, J. Zhao, and Z. Wei. “Thermal investigation of lithium-ion battery module with different cell arrangement structures and forced air-cooling strategies”. In: *Applied Energy* 134 (2014), pp. 229–238.
- [16] K.-C. Chiu, C.-H. Lin, S.-F. Yeh, Y.-H. Lin, C.-S. Huang, and K.-C. Chen. “Cycle life analysis of series connected lithium-ion batteries with temperature difference”. In: *Journal of Power Sources* 263 (2014), pp. 75–84.
- [17] N. Yang, X. Zhang, B. Shang, and G. Li. “Unbalanced discharging and aging due to temperature differences among the cells in a lithium-ion battery pack with parallel combination”. In: *Journal of Power Sources* 306 (2016), pp. 733–741.
- [18] M. Dubarry, C. Truchot, M. Cugnet, B. Y. Liaw, K. Gering, S. Sazhin, D. Jamison, and C. Michelbacher. “Evaluation of commercial lithium-ion cells based on composite positive electrode for plug-in hybrid electric vehicle applications. Part I: Initial characterizations”. In: *Journal of Power Sources* 196.23 (2011), pp. 10328–10335.
- [19] S. F. Schuster, M. J. Brand, P. Berg, M. Gleissenberger, and A. Jossen. “Lithium-ion cell-to-cell variation during battery electric vehicle operation”. In: *Journal of Power Sources* 297 (2015), pp. 242–251.
- [20] C. Campestrini, P. Keil, S. F. Schuster, and A. Jossen. “Ageing of lithium-ion battery modules with dissipative balancing compared with single-cell ageing”. In: *Journal of Energy Storage* 6 (2016), pp. 142–152.
- [21] T. Baumhöfer, M. Brühl, S. Rothgang, and D. U. Sauer. “Production caused variation in capacity aging trend and correlation to initial cell performance”. In: *Journal of Power Sources* 247 (2014), pp. 332–338.
- [22] C. Pastor-Fernandez, T. Bruen, W. D. Widanage, M. A. Gama-Valdez, and J. Marco. “A Study of Cell-to-Cell Interactions and Degradation in Parallel Strings: Implications for the Battery Management System”. In: *Journal of Power Sources* 329 (2016), pp. 574–585.
- [23] S. Wang, L. Shang, Z. Li, H. Deng, and J. Li. “Online dynamic equalization adjustment of high-power lithium-ion battery packs based on the state of balance estimation”. In: *Applied Energy* 166 (2016), pp. 44–58.
- [24] L. H. Saw, Y. Ye, A. A. Tay, W. T. Chong, S. H. Kuan, and M. C. Yew. “Computational fluid dynamic and thermal analysis of Lithium-ion battery pack with air cooling”. In: *Applied Energy* 177 (2016), pp. 783–792.
- [25] T. Yang, N. Yang, X. Zhang, and G. Li. “Investigation of the thermal performance of axial-flow air cooling for the lithium-ion battery pack”. In: *International Journal of Thermal Sciences* 108 (2016), pp. 132–144.
- [26] P. Keil, S. F. Schuster, J. Wilhelm, J. Travi, A. Hauser, R. C. Karl, and A. Jossen. “Calendar Aging of Lithium-Ion Batteries - I. Impact of the Graphite Anode on Capacity Fade”. In: *Journal of The Electrochemical Society* 163.9 (2016), A1872–A1880.

-
- [27] P. Keil and A. Jossen. “Calendar Aging of NCA Lithium-Ion Batteries Investigated by Differential Voltage Analysis and Coulomb Tracking”. In: *Journal of The Electrochemical Society* 164.1 (2017), A6066–A6074.
- [28] P. Keil. “Aging of Lithium-Ion Batteries in Electric Vehicles”. Dissertation. Technical University of Munich, Department of Electrical and Computer Engineering, Institute for Electrical Energy Storage Technology, Munich, Germany, 2017.
- [29] F. M. Kindermann, J. Keil, A. Frank, and A. Jossen. “A SEI Modeling Approach Distinguishing between Capacity and Power Fade”. In: *Journal of The Electrochemical Society* 164.12 (2017), E287–E294.
- [30] P. Keil and A. Jossen. “Impact of Dynamic Driving Loads and Regenerative Braking on the Aging of Lithium-Ion Batteries in Electric Vehicles”. In: *Journal of The Electrochemical Society* 164.13 (2017), A3081–A3092.
- [31] T. Waldmann, B.-I. Hogg, and M. Wohlfahrt-Mehrens. “Li plating as unwanted side reaction in commercial Li-ion cells – A review”. In: *Journal of Power Sources* 384 (2018), pp. 107–124.
- [32] Y. Wang, C. Zhang, Z. Chen, J. Xie, and X. Zhang. “A novel active equalization method for lithium-ion batteries in electric vehicles”. In: *Applied Energy* 145 (2015), pp. 36–42.
- [33] L. Zhong, C. Zhang, Y. He, and Z. Chen. “A method for the estimation of the battery pack state of charge based on in-pack cells uniformity analysis”. In: *Applied Energy* 113 (2014), pp. 558–564.
- [34] J. Li, J. Klee Barillas, C. Guenther, and M. A. Danzer. “Multicell state estimation using variation based sequential Monte Carlo filter for automotive battery packs”. In: *Journal of Power Sources* 277 (2015), pp. 95–103.
- [35] F. Altaf, L. Johannesson, and B. Egardt. “Simultaneous Thermal and State-of-Charge Balancing of Batteries: A Review”. In: *Proceedings IEEE Vehicle Power and Propulsion Conference (VPPC, Coimbra, Portugal, 2014)* (2014).
- [36] J. V. Barreras, C. Pinto, R. de Castro, E. Schaltz, S. J. Andreasen, and R. E. Araujo. “Multi-Objective Control of Balancing Systems for Li-Ion Battery Packs: A Paradigm Shift?” In: *Proceedings IEEE Vehicle Power and Propulsion Conference (VPPC, Coimbra, Portugal, 2014)* (2014).
- [37] C. Pinto, J. V. Barreras, E. Schaltz, and R. E. Araujo. “Evaluation of Advanced Control for Li-ion Battery Balancing Systems using Convex Optimization”. In: *IEEE Transactions on Sustainable Energy* 7.4 (2016), pp. 1703–1717.
- [38] K. Rumpf, M. Naumann, and A. Jossen. “Experimental investigation of parametric cell-to-cell variation and correlation based on 1100 commercial lithium-ion cells”. In: *Journal of Energy Storage* 14P1 (2017), pp. 224–243.
- [39] K. Rumpf, A. Rheinfeld, M. Schindler, J. Keil, T. Schua, and A. Jossen. “Influence of Cell-to-Cell Variations on the Inhomogeneity of Lithium-Ion Battery Modules”. In: *Journal of The Electrochemical Society* 165.11 (2018), A2587–A2607.
- [40] M. Dubarry, C. Truchot, B. Y. Liaw, K. Gering, S. Sazhin, D. Jamison, and C. Michelbacher. “Evaluation of commercial lithium-ion cells based on composite positive electrode for plug-in hybrid electric vehicle applications. Part II: Degradation mechanism under 2C cycle aging”. In: *Journal of Power Sources* 196.23 (2011), pp. 10336–10343.

- [41] Y. Zheng, X. Han, L. Lu, J. Li, and M. Ouyang. “Lithium ion battery pack power fade fault identification based on Shannon entropy in electric vehicles”. In: *Journal of Power Sources* 223 (2013), pp. 136–146.
- [42] Y. Zheng, M. Ouyang, L. Lu, J. Li, X. Han, L. Xu, H. Ma, T. A. Dollmeyer, and V. Freyermuth. “Cell state-of-charge inconsistency estimation for LiFePO₄ battery pack in hybrid electric vehicles using mean-difference model”. In: *Applied Energy* 111 (2013), pp. 571–580.
- [43] F. An, L. Chen, J. Huang, J. Zhang, and P. Li. “Rate dependence of cell-to-cell variations of lithium-ion cells”. In: *Scientific Reports* 6 (2016), pp. 1–7.
- [44] B. Kenney, K. Darcovich, D. D. MacNeil, and I. J. Davidson. “Modelling the impact of variations in electrode manufacturing on lithium-ion battery modules”. In: *Journal of Power Sources* 213 (2012), pp. 391–401.
- [45] S. Santhanagopalan and R. E. White. “Quantifying Cell-to-Cell Variations in Lithium Ion Batteries”. In: *International Journal of Electrochemistry* 2012.12 (2012), pp. 1–10.
- [46] S. F. Schuster, M. J. Brand, C. Campestrini, M. Gleissenberger, and A. Jossen. “Correlation between capacity and impedance of lithium-ion cells during calendar and cycle life”. In: *Journal of Power Sources* 305 (2016), pp. 191–199.
- [47] H.-G. Schweiger, O. Obeidi, O. Komesker, A. Raschke, M. Schiemann, C. Zehner, M. Gehnen, M. Keller, and P. Birke. “Comparison of several methods for determining the internal resistance of lithium ion cells”. In: *Sensors* 10.6 (2010), pp. 5604–5625.
- [48] J. Kim and B. H. Cho. “Screening process-based modeling of the multi-cell battery string in series and parallel connections for high accuracy state-of-charge estimation”. In: *Energy* 57 (2013), pp. 581–599.
- [49] S. Kamalishahroudi, J. Huang, Z. Li, and J. Zhang. “Study of Temperature Difference and Current Distribution in Parallel-Connected Cells at Low Temperature”. In: *International Journal of Electrical, Robotics, Electronics and Communications Engineering* 8.10 (2014), pp. 1589–1592.
- [50] T. Grün, K. Stella, and O. Wollersheim. “Impacts on load distribution and ageing in Lithium-ion home storage systems”. In: *Energy Procedia* 135 (2017), pp. 236–248.
- [51] M. Fleckenstein, O. Bohlen, M. A. Roscher, and B. Bäker. “Current density and state of charge inhomogeneities in Li-ion battery cells with LiFePO₄ as cathode material due to temperature gradients”. In: *Journal of Power Sources* 196.10 (2011), pp. 4769–4778.
- [52] O. Capron, A. Samba, N. Omar, T. Coosemans, P. Van den Bosche, and J. Van Mierlo. “Lithium-Ion Batteries: Thermal Behaviour Investigation of Unbalanced Modules”. In: *Sustainability* 7 (2015), pp. 8374–8398.
- [53] M. Dubarry, A. Devie, and B. Y. Liaw. “Cell-balancing currents in parallel strings of a battery system”. In: *Journal of Power Sources* 321 (2016), pp. 36–46.
- [54] Y. Troxler, B. Wu, M. Marinescu, V. Yufit, Y. Patel, A. J. Marquis, N. P. Brandon, and G. J. Offer. “The effect of thermal gradients on the performance of lithium-ion batteries”. In: *Journal of Power Sources* 247 (2014), pp. 1018–1025.
- [55] W. Shi, X. Hu, C. Jin, J. Jiang, Y. Zhang, and T. Yip. “Effects of imbalanced currents on large-format LiFePO₄-graphite batteries systems connected in parallel”. In: *Journal of Power Sources* 2016.313 (2016), pp. 198–204.

-
- [56] H.-H. Huang, H.-Y. Chen, K.-C. Liao, H.-T. Young, H.-T. Lee, and J.-Y. Tien. “Thermal electrochemical coupled simulations for cell-to-cell imbalances in lithium-iron-phosphate based battery packs”. In: *Applied Thermal Engineering* 123 (2017), pp. 584–591.
- [57] M. P. Klein and J. W. Park. “Current Distribution Measurements in Parallel-Connected Lithium-Ion Cylindrical Cells under Non-Uniform Temperature Conditions”. In: *Journal of The Electrochemical Society* 164.9 (2017), A1893–A1906.
- [58] M. Doyle, T. F. Fuller, and J. Newman. “Modeling of Galvanostatic Charge and Discharge of the Lithium/Polymer/Insertion Cell”. In: *Journal of The Electrochemical Society* 140.6 (1993), pp. 1526–1533.
- [59] M. Doyle. “Design and Simulation of Lithium Rechargeable Batteries”. Dissertation. University of California, Department of Chemical Engineering, Berkeley, USA, 1995.
- [60] T. F. Fuller, M. Doyle, and J. Newman. “Simulation and Optimization of the Dual Lithium Ion Insertion Cell”. In: *Journal of The Electrochemical Society* 141.1 (1994), pp. 1–9.
- [61] J. Newman and K. Thomas-Alyea. *Electrochemical Systems*. Hoboken, New Jersey: John Wiley and Sons Inc., 2004.
- [62] S. Rothgang, T. Baumhöfer, H. van Hoek, T. Lange, R. W. De Doncker, and D. U. Sauer. “Modular battery design for reliable, flexible and multi-technology energy storage systems”. In: *Applied Energy* 137 (2015), pp. 931–937.
- [63] L. Fahrmeir, C. Heumann, R. Künstler, I. Pigeot, and G. Tutz. *Statistik*. 8th ed. Berlin Heidelberg: Springer, 2016.
- [64] M. Safari and C. Delacourt. “Modeling of a Commercial Graphite/LiFePO₄ Cell”. In: *Journal of The Electrochemical Society* 158.5 (2011), A562–A571.
- [65] M. Guo, G. Sikha, and R. E. White. “Single-Particle Model for a Lithium-Ion Cell: Thermal Behavior”. In: *Journal of The Electrochemical Society* 158.2 (2011), A122–A132.
- [66] J. Li, Y. Cheng, M. Jia, Y. Tang, Y. Lin, Z. Zhang, and Y. Liu. “An electrochemical-thermal model based on dynamic responses for lithium iron phosphate battery”. In: *Journal of Power Sources* 255 (2014), pp. 130–143.
- [67] J. L. Dodd. “Phase composition and dynamical studies of lithium iron phosphate”. Dissertation. California Institute of Technology, Engineering and Applied Science, Pasadena, California, 2007.
- [68] D. A. G. Bruggeman. “Berechnung verschiedener physikalischer Konstanten von heterogenen Substanzen”. In: *Annalen der Physik* 24.5 (1935), pp. 636–664.
- [69] J. Landesfeind, J. Hattendorff, A. Ehrl, W. A. Wall, and H. A. Gasteiger. “Tortuosity Determination of Battery Electrodes and Separators by Impedance Spectroscopy”. In: *Journal of Electrochemical Society* 163 (2016), A1373–A1387.
- [70] L. O. Valøen and J. N. Reimers. “Transport Properties of LiPF₆-Based Li-Ion Battery Electrolytes”. In: *Journal of The Electrochemical Society* 152.5 (2005), A882–A891.
- [71] M. Guo and R. White. “A distributed thermal model for a Li-ion electrode plate pair”. In: *Journal of Power Sources* 221 (2013), pp. 334–344.
- [72] C. Campestrini. “Practical feasibility of Kalman filters for the state estimation of lithium-ion batteries”. Dissertation. Technical University of Munich, Department of Electrical and Computer Engineering, Institute for Electrical Energy Storage Technology, Munich, Germany, 2017.

- [73] J. Wilhelm, S. Seidlmayer, S. Erhard, M. Hofmann, R. Gilles, and A. Jossen. “In Situ Neutron Diffraction Study of Lithiation Gradients in Graphite Anodes during Discharge and Relaxation”. In: *Journal of The Electrochemical Society* 165.9 (2018), A1846–A1856.
- [74] G. Zhang, L. Cao, S. Ge, C.-Y. Wang, C. E. Shaffer, and C. D. Rahn. “In Situ Measurement of Radial Temperature Distributions in Cylindrical Li-Ion Cells”. In: *Journal of The Electrochemical Society* 161.10 (2014), A1499–A1507.
- [75] M. Naumann. “Techno-economic evaluation of stationary battery energy storage systems with special consideration of aging”. Dissertation. Technical University of Munich, Department of Electrical and Computer Engineering, Institute for Electrical Energy Storage Technology, Munich, Germany, 2018.
- [76] V. V. Viswanathan, D. Choi, D. Wang, W. Xu, S. Towne, R. E. Williford, J.-G. Zhang, J. Liu, and Z. Yang. “Effect of entropy change of lithium intercalation in cathodes and anodes on Li-ion battery thermal management”. In: *Journal of Power Sources* 195.11 (2010), pp. 3720–3729.
- [77] B. Pattipati, B. Balasingam, G. V. Avvari, K. R. Pattipati, and Y. Bar-Shalom. “Open circuit voltage characterization of lithium-ion batteries”. In: *Journal of Power Sources* 269 (2014), pp. 317–333.
- [78] A. Jossen and W. Weydanz. *Moderne Akkumulatoren richtig einsetzen*. 1st ed. Untermeitingen: Inge Reichardt Verlag, 2006.
- [79] D. Aurbach. *Nonaqueous electrochemistry*. 8th ed. New York, Basel: Marcel Dekker Inc., 1999.
- [80] A. Ehrl, J. Landesfeind, W. A. Wall, and H. A. Gasteiger. “Determination of Transport Parameters in Liquid Binary Electrolytes: Part II. Transference Number”. In: *Journal of The Electrochemical Society* 164162.12 (2017), A2716–A2731.
- [81] R. Korthauer. *Handbuch Lithium-Ionen-Batterien*. Berlin Heidelberg: Springer, 2013.
- [82] Q. Wang, B. Jiang, B. Li, and Y. Yan. “A critical review of thermal management models and solutions of lithium-ion batteries for the development of pure electric vehicles”. In: *Renewable and Sustainable Energy Reviews* 64 (2016), pp. 106–128.
- [83] M. C. Smart, B. V. Ratnakumar, L. Whitcanacka, K. Chin, M. Rodriguez, and S. Surampudia. “Performance characteristics of lithium ion cells at low temperatures”. In: *Proceedings Seventeenth Annual Battery Conference on Applications and Advances (Long Beach, USA, 2002)* (2002), pp. 41–46.
- [84] B. V. Ratnakumar and M. C. Smart. “Lithium Plating Behavior in Lithium-ion Cells”. In: *ECS Transactions* 25.36 (2010), pp. 241–252.
- [85] M. C. Smart and B. V. Ratnakumar. “Effects of Electrolyte Composition on Lithium Plating in Lithium-Ion Cells”. In: *Journal of The Electrochemical Society* 158.4 (2011), A379–A389.
- [86] V. Zinth, C. von Lüdgers, M. Hofmann, J. Hattendorff, I. Buchberger, S. Erhard, J. Rebelo-Kornmeier, A. Jossen, and R. Gilles. “Lithium plating in lithium-ion batteries at sub-ambient temperatures investigated by in situ neutron diffraction”. In: *Journal of Power Sources* 271 (2014), pp. 152–159.
- [87] L. Gireaud, S. Grugeon S.and Laruelle, B. Yrieix, and J.-M. Tarascon. “Lithium metal stripping/plating mechanisms studies: A metallurgical approach”. In: *Electrochemistry Communications* 8.10 (2006), pp. 1639–1649.

-
- [88] J. Steiger, D. Kramer, and R. Mönig. “Mechanisms of dendritic growth investigated by in situ light microscopy during electrodeposition and dissolution of lithium”. In: *Journal of Power Sources* 261 (2014), pp. 112–119.
- [89] A. Senyshyn, M. Mühlbauer, O. Dolotko, and H. Ehrenberg. “Low-temperature performance of Li-ion batteries: The behavior of lithiated graphite”. In: *Journal of Power Sources* 282 (2015), pp. 235–240.
- [90] T. Bandhauer, S. Garimella, and T. F. Fuller. “Electrochemical-Thermal Modeling to Evaluate Battery Thermal Management Strategies: I. Side Cooling”. In: *Journal of The Electrochemical Society* 162.1 (2015), A125–A136.
- [91] P. J. Osswald, S. V. Erhard, J. Wilhelm, H. E. Hoster, and A. Jossen. “Simulation and Measurement of Local Potentials of Modified Commercial Cylindrical Cells, I: Cell Preparation and Measurements”. In: *Journal of The Electrochemical Society* 162.10 (2015), A2099–A2105.
- [92] S. V. Erhard, P. J. Osswald, J. Wilhelm, A. J. Rheinfeld, S. Kosch, and A. Jossen. “Simulation and Measurement of Local Potentials of Modified Commercial Cylindrical Cells, II: Multi-Dimensional Modeling and Validation”. In: *Journal of The Electrochemical Society* 162.14 (2015), A2707–A2719.
- [93] H. Maleki, S. Al Hallaj, J. R. Selman, R. B. Dinwiddie, and H. Wang. “Thermal Properties of Lithium-Ion Battery and Components”. In: *Journal of The Electrochemical Society* 146.3 (1999), pp. 947–954.
- [94] S. C. Chen, C. C. Wan, and Y. Y. Wang. “Thermal analysis of lithium-ion batteries”. In: *Journal of Power Sources* 140.1 (2005), pp. 111–124.
- [95] T. Bandhauer, S. Garimella, and T. F. Fuller. “A Critical Review of Thermal Issues in Lithium-Ion Batteries”. In: *Journal of The Electrochemical Society* 158.3 (2011), R1–R25.
- [96] S. Drake, D. Wetz, J. Ostanek, S. Miller, J. Heinzl, and A. Jain. “Measurement of anisotropic thermophysical properties of cylindrical Li-ion cells”. In: *Journal of Power Sources* 252 (2014), pp. 298–304.
- [97] G. F. Hewitt, T. R. Bott, and G. L. Shires. *Process heat transfer*. Begell House, Boca Raton: CRC Press, 1994.
- [98] G. Guo, B. Long, B. Cheng, S. Zhou, P. Xu, and B. Cao. “Three-dimensional thermal finite element modeling of lithium-ion battery in thermal abuse application”. In: *Journal of Power Sources* 195.8 (2010), pp. 2393–2398.
- [99] W. Polifke and J. Kopitz. *Wärmeübertragung - Grundlagen, analytische und numerische Methoden*. 2nd ed. München: Pearson Studium, 2009.
- [100] V. Gnielinski. “Berechnung mittlerer Wärme- und Stoffübergangskoeffizienten an laminar und turbulent überströmten Einzelkörpern mit Hilfe einer einheitlichen Gleichung”. In: *Forschung im Ingenieurwesen* 41.5 (1975), pp. 145–153.
- [101] VDI e.V. *VDI-Wärmeatlas*. 11th ed. Berlin Heidelberg: Springer, 2013.
- [102] J. P. Schmidt. “Verfahren zur Charakterisierung und Modellierung von Lithium-Ionen Zellen”. Dissertation. Karlsruher Institut für Technologie, Fakultät für Elektrotechnik und Informationstechnik, Institut für Werkstoffe der Elektrotechnik, Karlsruhe, Germany, 2013.

- [103] O. S. Bohlen. “Impedance-based battery monitoring”. Dissertation. RWTH Aachen University, Faculty of Electrical Engineering and Information Technology, Institute for Power Electronics and Electrical Drives, Aachen, Germany, 2008.
- [104] F. M. Kindermann, A. Noel, S. V. Erhard, and A. Jossen. “Long-term equalization effects in Li-ion batteries due to local state of charge inhomogeneities and their impact on impedance measurements”. In: *Electrochimica Acta* 185 (2015), pp. 107–116.
- [105] DIN (German Institute for Standards). *Fundamentals of metrology - Part 3: Evaluation of measurements of a single measurand, measurement uncertainty (DIN 1319-3:1996-05)*. Standard. Berlin, D: German Institute for Standards, May 1996.
- [106] DIN (German Institute for Standards). *Statistics - Vocabulary and symbols - Part 1: General statistical terms and terms used in probability (ISO 3534-1:2006); Text in German and English*. Standard. Berlin, D: German Institute for Standards, Oct. 2009.
- [107] J. Kasnatscheew, T. Placke, B. Streipert, S. Rothermel, R. Wagner, P. Meister, I. C. Laskovic, and M. Winter. “A Tutorial into Practical Capacity and Mass Balancing of Lithium Ion Batteries”. In: *Journal of The Electrochemical Society* 164.12 (2017), A2479–A2486.
- [108] D. J. Docimo and H. K. Fathy. “Multivariable State Feedback Control as a Foundation for Lithium-Ion Battery Pack Charge and Capacity Balancing”. In: *Journal of The Electrochemical Society* 164.2 (2017), A61–A70.
- [109] J. Wilhelm, S. Seidlmayer, P. Keil, J. Schuster, A. Kriele, R. Gilles, and A. Jossen. “Cycling capacity recovery effect: A coulombic efficiency and postmortem study”. In: *Journal of Power Sources* 365 (2017), pp. 327–338.
- [110] M. Doyle, J. P. Meyers, and J. Newman. “Computer Simulations of the Impedance Response of Lithium Rechargeable Batteries”. In: *Journal of The Electrochemical Society* 147.1 (2000), pp. 99–110.
- [111] J. P. Meyers, M. Doyle, R. M. Darling, and J. Newman. “The Impedance Response of a Porous Electrode Composed of Intercalation Particles”. In: *Journal of The Electrochemical Society* 147.8 (2000), pp. 2930–2940.
- [112] J. Huang, H. Ge, Z. Li, and J. Zhang. “An Agglomerate Model for the Impedance of Secondary Particle in Lithium-Ion Battery Electrode”. In: *Journal of The Electrochemical Society* 161.8 (2014), E3202–E3215.
- [113] G. Sikha and R. E. White. “Analytical Expression for the Impedance Response of an Insertion Electrode Cell”. In: *Journal of The Electrochemical Society* 154.1 (2007), A43–A54.
- [114] G. Sikha and R. E. White. “Analytical Expression for the Impedance Response for a Lithium-Ion Cell”. In: *Journal of The Electrochemical Society* 155.12 (2008), A893–A902.
- [115] A. Nyman, T. G. Zavalis, R. Elger, M. Behm, and G. Lindbergh. “Analysis of the Polarization in a Li-Ion Battery Cell by Numerical Simulations”. In: *Journal of The Electrochemical Society* 157.11 (2010), A1236–A1246.
- [116] R. Chandrasekaran. “Quantification of contributions to the cell overpotential during galvanostatic discharge of a lithium-ion cell”. In: *Journal of Power Sources* 262 (2014), pp. 501–513.
- [117] J. Huang, Z. Li, J. Zhang, S. Song, Z. Lou, and N. Wu. “An Analytical Three-Scale Impedance Model for Porous Electrode with Agglomerates in Lithium-Ion Batteries”. In: *Journal of The Electrochemical Society* 162.4 (2015), A585–A595.

-
- [118] J. N. Reimers. “Accurate and Efficient Treatment of Foil Currents in a Spiral Wound Li-Ion Cell”. In: *Journal of The Electrochemical Society* 161.1 (2014), A118–A127.
- [119] A. A. Pesaran. “Battery thermal models for hybrid vehicle simulations”. In: *Journal of Power Sources* 110 (2002), pp. 377–382.
- [120] C. Kuper, M. Hoh, G. Houchin-Miller, and J. Fuhr. “Thermal Management of Hybrid Vehicle Battery Systems”. In: *Proceedings International Battery, Hybrid and Fuel Cell Electric Vehicle Symposium (EVS24, Stavanger, Norway, 2009)* (2009), pp. 1–10.
- [121] A. Rheinfeld, S. Kosch, S. V. Erhard, P. J. Osswald, B. Rieger, and A. Jossen. “Electro-Thermal Modeling of Large Format Lithium-Ion Pouch Cells: A Cell Temperature Dependent Linear Polarization Expression”. In: *Journal of The Electrochemical Society* 163.14 (2016), A3046–A3062.
- [122] S. V. Erhard. “Mehrdimensionale elektrochemisch-thermische Modellierung von Lithium-Ionen-Batterien”. Dissertation. Technical University of Munich, Department of Electrical and Computer Engineering, Institute for Electrical Energy Storage Technology, Munich, Germany, 2017.
- [123] S. V. Erhard et al. “Simulation and Measurement of the Current Density Distribution in Lithium-Ion Batteries by a Multi-Tab Cell Approach”. In: *Journal of The Electrochemical Society* 164.1 (2017), A6324–A6333.
- [124] S. Kosch, A. Rheinfeld, S. V. Erhard, and A. Jossen. “An extended polarization model to study the influence of current collector geometry of large-format lithium-ion pouch cells”. In: *Journal of Power Sources* 342 (2017), pp. 666–676.
- [125] H. Bernardi, E. Pawlikowski, and J. Newman. “A General Energy Balance for Battery Systems”. In: *Journal of The Electrochemical Society* 132.1 (1985), pp. 5–12.
- [126] TATA Steel. *HILUMIN Batterie-Verbinderband*. 15.01.2017. URL: <https://www.tatasteeleurope.com/en/products-and-services/flat/electro-plated/hilumin/hilumin> (visited on 01/15/2017).
- [127] M. Doyle and J. Newman. “Comparison of Modeling Predictions with Experimental Data from Plastic Lithium Ion Cells”. In: *Journal of The Electrochemical Society* 143.6 (1996), pp. 1890–1903.
- [128] M. Doyle and Y. Fuentes. “Computer Simulations of a Lithium-Ion Polymer Battery and Implications for Higher Capacity Next-Generation Battery Designs”. In: *Journal of The Electrochemical Society* 150.6 (2003), A706–A713.
- [129] S.-Y. Chung, J. T. Bloking, and Y.-M. Chiang. “Electronically conductive phospho-olivines as lithium storage electrodes”. In: *Nature Materials* 1 (2002), A123–A128.
- [130] M. J. Brand, P. A. Schmidt, M. F. Zäh, and A. Jossen. “Welding techniques for battery cells and resulting electrical contact resistances”. In: *Journal of Energy Storage* 1 (2015), pp. 7–14.
- [131] R. P. Tye. *Thermal Conductivity*. 2nd ed. London and New York: Academic Press, 1969.
- [132] L. H. Saw, Y. Ye, and A. A. Tay. “Electro-thermal analysis and integration issues of lithium ion battery for electric vehicles”. In: *Applied Energy* 131 (2014), pp. 97–107.
- [133] K. Rumpf, M. Naumann, and A. Jossen. *Statistic analysis of experimentally determined cell parameters based on 1100 production fresh commercial lithium-ion cells*. <https://mediatum.ub.tum.de/1368108>. 2017.

- [134] N. Xue, W. Du, T. A. Greszler, W. Shyy, and J. R. Martins. “Design of a lithium-ion battery pack for PHEV using a hybrid optimization method”. In: *Applied Energy* 115 (2014), pp. 591–602.
- [135] B. Coleman, J. Ostanek, and J. Heinzl. “Reducing cell-to-cell spacing for large-format lithium ion battery modules with aluminum or PCM heat sinks under failure conditions”. In: *Applied Energy* 180 (2016), pp. 14–26.

List of Figures

1.1	Influencing factors on inhomogeneity in lithium-ion battery modules.	2
1.2	Structure of the thesis.	5
3.1	Schematic of a jelly roll and the different layers.	20
3.3	Tortuosity of the LiC ₆ and LiFePO ₄ electrodes as a function of porosity ε_1 compared to the Bruggeman relation.	24
3.4	Transport parameters of the electrolyte as a function of lithium concentration c_1 and cell temperature T_{cell} : (a) Diffusion coefficient D_1 , (b) Ionic conductivity κ_1 and (c) Activity dependency $\frac{\partial \ln f_{\pm}}{\partial \ln c_1}$	25
3.5	Diffusivity (a) and reaction rate (b) of the LiC ₆ and LiFePO ₄ electrodes as a function of cell temperature T_{cell} . Note, that the diffusivity of the LiFePO ₄ electrode in (a) does also show an exponential behaviour but has reference diffusion coefficient $D_{s,\text{ref}}$ which is four magnitudes smaller than for the LiC ₆ electrode. Note, that in (b) the reaction rates curves of both electrodes are the same as they are implemented using the same reference reaction rates and activation energies.	26
3.6	Definition of values for calculating h_{conv} for a bunch of four cells in aligned and staggered arrangement.	31
4.1	Flow chart of the measurement and storage sequence illustrating the temperature condition and time duration of each step.	37
4.2	Definition of parameters from the last part of the CU-measurement and Nyquist diagram of the EIS-measurement.	40
4.3	Variations of the discharge capacity during only CC-phase, only CV-phase and combined CCCV-phase.	43
4.4	Variations of the DC impedances after 10s R_DC_10s, 30s R_DC_30s and 60s R_DC_60s.	45
4.5	Variations of the ohmic AC impedances R_AC_Im0 and R_AC_1000Hz.	46
4.6	Variations of the local maximum AC impedance R_AC_max, and the local minimum AC impedance R_AC_min.	48
4.7	Variations of the interpolated AC frequencies f_AC_Im0, f_AC_max and f_AC_min.	50
4.8	Variations of the mass and mean temperature during the CU-measurement T_Mean.	51
4.9	Correlations between R_DC_10s, R_AC_Im0, R_AC_1000Hz, R_AC_min and R_AC_max.	55
4.10	Correlations between Mass, T_Mean, C_DCH_CC, C_DCH_CV, C_DCH_CCCV, R_DC_10s and R_AC_Im0.	57

5.1	Manufacturing process chain for lithium-ion cells.	64
5.2	Scheme of the coupled model of connected lithium-ion cells.	69
5.3	Equivalent electric circuits of different topologies considering both, battery cells and the resistances of cell connectors and welding spot joints.	73
5.4	(a) Top view of parallel connected cells or strings. (b) Equivalent circuit of parallel connected strings illustrating the different locations of the ST. (c) Flow charts for calculating the string currents within all $xSyP$ topologies.	75
5.5	Validation of the single cell model at $T_{\text{amb}} = 25\text{ }^{\circ}\text{C}$ and $v_{\text{air}} = 1\text{ m s}^{-1}$	81
5.6	Current distribution during a $1C$ discharge scenario within the connected cells of a 2P module, which is contacted at ST_{mid} or ST_{side} under differently induced inhomogeneity.	85
5.7	Cumulated Ah-throughput Ah_{cell}	89
5.8	Absolute difference in Ah-throughput $ \Delta Ah_{\text{cell}} $	90
5.9	Cumulated Ah-throughput Ah_{cell} and absolute difference in Ah-throughput $ \Delta Ah_{\text{cell}} $ for a 2P module contacted at ST_{side}	91
5.10	Current distribution during a $0.25C$ discharge scenario within the connected cells of a 2P module, which is contacted at ST_{mid} or ST_{side} under differently induced inhomogeneity.	92
5.11	Current distribution during a $4C$ discharge scenario within the connected cells of a 2P module, which is contacted at ST_{mid} or ST_{side} under differently induced inhomogeneity.	93
6.1	Current distribution under a $1C$ discharge scenario within the connected cells of a 2P module under different thermal gradients and additional dC and dR variations.	99
6.2	Influence of different cell connector resistances on the observed peak currents within a 2P module under a ST_{side} -connection and under a $1C$ CC-discharge.	102

List of Tables

2.1	Overview over the literature review regarding the statistic analysis of battery cells. . . .	8
2.2	Overview over the literature review regarding causes and effects of inhomogeneity. . . .	13
3.1	Nominal data of the investigated cell Sony US26650FTC1.	18
3.2	Governing equations within the p2D Newman-model.	21
3.3	Thermal properties of the cell components and the calculated cell properties.	29
3.4	Dimensionless thermal parameters for a single cylindrical cell and different battery module topologies.	33
4.1	Precision of the measurement equipment.	36
4.2	Experimentally determined parametric variations of the two investigated batches of cells. 53	
4.3	Overview of experimental investigations on cell-to-cell variations of capacity and impedance of production fresh cells reported in literature.	54
4.4	Experimentally determined parametric correlation coefficients between all 15 investigated parameters.	59
5.1	General ELM equations for the string currents i_j within $xSyP$ topologies contacted at ST_{side}	76
5.2	General ELM equations for the string currents i_j within $xSyP$ topologies contacted at ST_{mid}	77
5.3	General coupling equations between ELM and PCM for different $xSyP$ topologies. . . .	80
5.4	Physicochemical model parameters for the porous electrode and separator domain of the investigated cell SONYUS26650FTC1.	82
5.5	Geometric, electric and thermal model parameters for different components.	83
5.6	Resulting maximum peak currents within a 2P module under different $C-Rates$	94
6.1	Resulting maximum peak currents within a 2P module under different variations.	98
6.2	Electrical resistance data for cell connectors of different material and thickness.	101
6.3	Maximum suitable cell connector resistance values to not exceed a threshold peak current.104	